Modelling of Alternative Divertor Power Exhaust

Cyd Zachary Luis Cowley

Doctor of Philosophy

University of York
School of Physics, Engineering and Technology

October 2023

Abstract

Controlled fusion on Earth is one of the most powerful technological dreams devised by humanity. The prospect of an artificial star on our planet could offer reliable, clean, and widely accessible energy for all, using the most common element in the universe as fuel. Despite all its prospects, an economic fusion power plant has not yet been developed, due to the enormity and complexity of the challenges in the way of such a feat. In tokamaks, where a high temperature plasma is confined using strong magnetic fields, one of the most pressing issues is that of plasma exhaust. As these fusion devices become more powerful and better confined, the peak heat and particle loads on surrounding surfaces is enough to erode and damage even the strongest materials.

The focus of this thesis is the study of alternative divertors, one proposed solution to the tokamak exhaust challenge. By modelling edge plasmas under different conditions and geometries, this work furthers the understanding of how these different geometric features can influence divertor performance. The process of detachment, characterised by significant power and pressure loss in an edge plasma, is a key focal point for this modelling work.

By developing and extending reduced models, and comparing them to hundreds of 2D simulations of alternative divertors, good agreement is found for the predicted impacts of divertor features on detachment. These models are also compared with experiment, where certain broad predictions and ideas from reduced modelling seem present in experimental data. The agreement is not perfect, and when it comes to the movement of so-called detachment fronts, the location of these fronts is much more stable in 2D simulations and experiment than the reduced modelling. Notwithstanding, this work provides first of a kind verification of a reduced physics framework to understand the control of divertor detachment.

Declaration of Authorship

I, Cyd Zachary Luis Cowley, declare that this thesis titled, "Modelling of Alternative Divertor Power Exhaust" and the work presented in it are my own. I confirm that:

- This work was done wholly or mainly while in candidature for a research degree at this University.
- Where any part of this thesis has previously been submitted for a degree or any other qualification at this University or any other institution, this has been clearly stated.
- Where I have consulted the published work of others, this is always clearly attributed.
- Where I have quoted from the work of others, the source is always given. With the exception of such quotations, this thesis is entirely my own work.
- I have acknowledged all main sources of help.
- Where the thesis is based on work done by myself jointly with others, I have made clear exactly what was done by others and what I have contributed myself.

Signed: 

Date: 28/24/2024

"There is a single light of science, and to brighten it anywhere is to brighten it everywhere."

Isaac Assimov

Acknowledgements

First I would like to thank the people who have made the duration of this PhD project worthwhile and the most enjoyable experience. This includes my friends, colleagues, and mentors associated with the Fusion CDT, who shared coffee, karaoke, and yoga with me in the YPI. My friends at CCFE, with whom I exchanged the most fascinating conversations over the most mundane Costa Coffee. And everyone at MIT, especially Adam; thank you for making me feel so welcome, and for making a Boston winter an incredibly warm experience.

I would also like to thank the friends outside of the PhD that continue to inspire me, and remind me what I'm doing this for (especially the Flans).

This thesis would have been a failure without the excellent guidance of my supervisors. David, who patiently answered my countless stupid questions. And Bruce, who taught me how to ask smart ones. Thank you.

This thesis is dedicated to my family. Without your love and support, I couldn't have done any of this.

Contents

List of Figures

List of Abbreviations

IR	**I**nfra**R**ed
IPCC	**I**nternational **P**anel on **C**limate **C**hange
NBI	**N**eutral **B**eam **I**njector
ECRH	**E**lectron **C**yclotron **R**esonance **H**eating
ICRH	**I**on **C**yclotron **R**esonance **H**eating
JET	**J**oint **E**uropean **T**orus
ASDEX-U	**A**xially **S**ymmetric **D**ivertor **E**xperiment-**U**pgrade
JT-60	**J**apan **T**orus-**60**
DIII-D	**D**oublet **III-D**
TCV	**T**okamak à **C**onfiguration **V**ariable
MAST-U	**M**ega **A**mpere **S**pherical **T**okamak-**U**pgrade
NSTX-U	The **N**ational **S**pherical **T**orus **E**xperiment-**U**pgrade
STEP	**S**pherical **T**okamak for **E**nergy **P**roduction
SOL	**S**crape **O**ff **L**ayer
PFR	**P**rivate **F**lux **R**egion
SXD	**S**uper-**X** **D**ivertor
ECD	Elongated **C**onventional **D**ivertor
SOLPS-ITER	**S**crape **O**ff **L**ayer **P**lasma **S**imulator - **ITER**
DLS	**D**etachment **L**ocation **S**ensitivity
MARFE	**M**ultifaceted **A**symmetric **R**adiation **F**rom the **E**dge
MWI	**M**ulti **W**avelength **I**maging
EFIT	Equilibrium **FIT**ting
DMS	**D**ivertor **M**onitoring **S**pectroscopy
LOS	**L**ine **O**f **S**ight

Physical Constants

Electron mass	$m = 9.109\,383\,7 \times 10^{-31}\,\mathrm{kg}$
Elementary charge	$e = 1.602\,176\,63 \times 10^{-19}\,\mathrm{C}$
Vacuum permittivity	$\epsilon_0 = 8.854\,187\,81 \times 10^{8}\,\mathrm{F\,m^{-1}}$
Boltzmann constant	$k_B = 1.380\,649 \times 10^{-23}\,\mathrm{JK^{-1}}$

List of Symbols

n	electron density	m^{-3}
T	electron temperature	eV
n_i	ion density	m^{-3}
T_i	ion temperature	eV
n_0	neutral density	m^{-3}
T_0	neutral temperature	eV
ω_p	plasma frequency	Hz
λ_D	Debye length	m
Λ	plasma parameter	
$\nu_{1,2}$	collision frequency of particle 1 on medium 2	Hz
q_1	charge of particle 1	C
q_2	charge of bulk medium 2	C
m_1	mass of particle 1	kg
n_2	density of bulk medium 2	m^{-3}
m_r	reduced mass of species 1 and 2	kg
v_1	speed of particle 1	ms^{-1}
P_{fusion}	fusion power density	$\mathrm{W\ m}^{-3}$
E_{fusion}	fusion reaction energy	J
$\langle \sigma \mathrm{v} \rangle$	fusion fuel reactivity	$\mathrm{m}^3\mathrm{s}^{-1}$
P_{loss}	power loss rate	$\mathrm{W\ m}^{-3}$
τ_E	energy confinement time	s
$\mathbf{B}$	magnetic field	T
$\mathbf{E}$	electric field	Vm^{-1}
B_{tor}	toroidal magnetic field strength	T
B_{pol}	poloidal magnetic field strength	T
B	total magnetic field strength	T
a	minor radius	m
R	major radius	m
P_{SOL}	Power entering the scrape-off layer	W
$q_{\|\|}$	parallel heat flux density	Wm^{-2}
λ_T	SOL temperature fall-off width	m
λ_n	SOL density fall-off width	m
λ_q	SOL heat flux fall-off width	m
$L_{\|\|}$	parallel divertor connection length	m
R_{recyc}	recycling fraction	
Γ_{recyc}	recycled particle flux	$\mathrm{s}^{-1}\mathrm{m}^{-2}$
$\Gamma_{i,t}$	incident ion flux	$\mathrm{s}^{-1}\mathrm{m}^{-2}$
v_i	ion flow velocity	$\mathrm{m}^{-1}\mathrm{s}^{-1}$
c_{st}	ion sound speed at the target	$\mathrm{m}^{-1}\mathrm{s}^{-1}$
γ	sheath transmission coefficient	
t	time	s
$\mathbf{v}_s$	velocity of species s	ms^{-1}

m_s	mass of species s	kg
$\mathbf{F}_{s,col}$	force applied to species s due to collisions with other species	N
S_s	external sources and sinks of species s	s^{-1}
n_s	density of species s	m^{-3}
p_s	thermal pressure of species s	Nm^{-2}
Π_s	viscosity tensor of species s	Nm^{-2}
Z_s	effective atomic number of species s	
$\mathbf{q}_s$	total heat flux of species s	Wm^{-2}
W_s	power density transfer to species s	Wm^{-3}
κ_s	heat conductivity of species s	
κ_0	spitzer conductivity divided by temperature to the 5/2	$Wm^{-2}eV^{-7/2}$
F_R	divertor total flux expansion	
f_{mom}	divertor momentum loss fraction	
f_{power}	divertor power loss fraction	
W_α	volumetric radiation from impurity species α	W m^{-3}
f_α	the fixed fraction of impurity species α	
L_α	the electron cooling function of impurity species α	W m^3
τ_α	divertor residence time of impurity species α	s
s	distance measured parallel along a magnetic field line	m
s_{pol}	distance in the poloidal plane along a magnetic field line	m
$s_{f,\|\|}$	parallel detachment front location	m
C	lumped detachment control parameter	$W^{-5/7}m^{-11/7}$
$L_{\|\|,f}$	parallel length from front location to the x-point	m
$\langle B \rangle_{\text{above } f}$	line-averaged divertor magnetic field strength	T
$s_{f,pol}$	poloidal detachment front location	m
F_{Tu}	extended dls model under-relaxation factor	
Θ	poloidal magnetic pitch	
F_Θ	poloidal flux expansion	
W_{other}	additional sources and sinks for electron conducted heat flux	Wm^{-3}
ψ	normalised magnetic flux	
$\langle n \rangle$	line averaged midplane density	m^{-3}

Executive Summary

This thesis concerns plasma physics for nuclear fusion, making contributions to the realm of alternative divertor physics through modelling and model comparison to experiment. The motivation for this work is explored in Chapter 1, including the need for nuclear fusion stemming from the adverse risks of energy insecurity and climate change. The fundamental science of nuclear fusion is laid out, and the concept of a tokamak is introduced. However, there are numerous physics and engineering challenges preventing an economic energy-producing tokamak power plant. Chief among these issues is the exhaust challenge, which describes how plasma facing components cannot withstand the unmitigated heat and particle loads emerging from high-power, well-confined reactor tokamaks.

Most current-generation tokamaks implement a divertor configuration to divert the scrape-off layer plasma escaping from the core towards target plates. For next-generation reactor-like devices, one potential solution to alleviate strong plasma and power loads is through detachment, where most of the plasma power and momentum is dissipated before the plasma reaches the divertor targets. One prospective method of optimising the process of detachment is by operating with an alternative divertor. Such divertors implement novel magnetic or geometric characteristics, such as expansion of magnetic flux or implementation of multiple x-points. These characteristics are thought to benefit plasma exhaust, though there is still much to understand concerning their physics principles and how these emerge into operational benefits and disadvantages.

One powerful way of developing intuition and understanding of alternative divertor features is through computational and theoretical modelling. As such, this thesis primarily leverages modelling tools to contribute to the understanding of alternative divertors and their features. Much of this modelling focuses on detachment evolution in different geometries, an area which is still relatively nascent.

In Chapter 2, the theoretical groundwork for modelling alternative divertors in the steady-state is laid out. Among the many modelling tools for divertors are fluid codes, which solve the Braginskii fluid equations for a scrape-off layer plasma. One such code is SOLPS-ITER [1]–[3], which couples a fluid code with a Kinetic Monte-Carlo code for modelling the transport of neutrals, which can have a range of collisionalities in the divertor. In addition to computationally expensive simulation tools, simple reduced modelling is also introduced. In particular, the two-point model is a powerful tool to study the relationship between upstream plasma parameters at the midplane, and the critical plasma conditions at the divertor targets.

A more novel modelling tool introduced in Chapter 2 is the Detachment Location Sensitivity (DLS) model. The DLS model is a simple tool to study how detachment is accessed, and how sensitive the location of detachment fronts are with respect to changes in key plasma parameters. The model, originally developed in [4], is modified for this work, and the predictions made by the model are considered. The model predicts that divertors which have long connection lengths, high total flux

expansions, and high divertor averaged magnetic fields will have easier access to detachment, benefiting plasma exhaust. Concerning the movement of detachment fronts, the DLS model predicts that certain features will lead to reduced detachment location sensitivity - corresponding to a detachment solution which is very stable and insensitive to variations in the plasma. According to the model, regions of low poloidal field, or high total magnetic field gradient, could lead to this reduced detachment location sensitivity. The DLS model even predicts the presence of negative location sensitivity regions in inner leg divertors, where the divertor plasma could bifurcate into attached or detached solutions for the same plasma parameters.

As part of this thesis, the DLS model has been extended to produce fully self-consistent heat flux and temperature profiles for arbitrary impurity radiators. This extended DLS model outputs detachment access and location sensitivity predictions which consider the effects of having a wide radiation region that could extend up to the midplane. This model may allow for more accurate predictions of detachment for reactor-like tokamaks, where impurities such as neon can radiate along the entire SOL.

In Chapter 3, the efficacy of the DLS model is explored by comparing predictions of the model to SOLPS-ITER simulations. The simulations used are of isolated divertor legs in simplified geometry, extending from the x-point to the target. The upstream heat flux, upstream electron density, and divertor impurity fraction are set and varied. The reason these simplified geometries are used is because one or two features may be varied in isolation. As such, they can be a powerful way of interrogating individual divertor features methodically.

Concerning detachment access, the isolated leg SOLPS-ITER simulations are shown to broadly agree with theoretical predictions. Specifically, divertors with high connection length and total flux expansion achieve easier access to detachment, with a stronger dependence on geometric features than predicted by the DLS model. The isolated leg SOLPS-ITER simulations also agree with the DLS model in terms of detachment location sensitivity. In regions of divertors with strong parallel magnetic field gradients, low poloidal pitch, or in regions closer to the x-point, the poloidal movement of detachment fronts is less sensitive to changes in detachment control parameters. In general, the SOLPS-ITER simulations display lower detachment location sensitivity than DLS model predictions. One prediction of the DLS model verified for the first time by SOLPS-ITER simulations is the presence of negative sensitivity regions caused by geometry, where a divertor may bifurcate into deeply detached or attached solutions for the same upstream conditions.

Work in Chapter 3 marks the first time the movement of detachment fronts in simulations have been compared to reduced modelling. The favourable comparison provides a framework to understand how detachment may evolve in different geometries, enabling designers of future tokamaks to optimise a divertor configuration for detachment control.

In Chapter 4, simulations of the MAST-U Super-X geometry are used to study the impact of divertor baffling on performance and detachment access. Density scan simulations are performed for an extremely open divertor, and an extremely tightly baffled divertor, at three different input powers. Simulations show the tightly baffled divertor detaches at a lower density than the open divertor, consistent with previous

studies [5]. However, this difference is notably lessened at higher powers.

In addition to detachment access, the geometries with different baffling show different behaviour when it comes to particle and heat transport. Specifically, neutrals are trapped much more in the divertor chamber in the tight geometry; as a result, the tight geometry shows much higher compression of neutrals in the divertor chamber. Moreover, in the tightly baffled geometry radiation occurs in small, localised regions in the divertor, whereas radiation occurs along the entire SOL in the open geometry. Because of this, the open divertor simulations tend to have lower heat fluxes entering the divertor, and lower upstream temperatures.

The study contained in 4 is a simple one, yet is an important attempt to build a fundamental understanding for a complex divertor design feature. If physicists better understand the impacts of divertor baffling, then this understanding can feed into the design choices of the material surrounding a divertor plasma.

In Chapter 5, results from alternative divertor experiments in the MAST-U tokamak are studied. Data from the Multi-Wavelength Imaging and Divertor Monitoring Spectroscopy diagnostics are used to identify and track the location of the leading edge of detachment fronts. Detachment front movement for these experiments are compared against parameters controlling detachment, and in particular measurements for the upstream electron density. To this end, the midplane interferometry and Thomson scattering systems are leveraged.

In the second experimental campaign of MAST-U, the movement of detachment fronts in an elongated conventional divertor density scan are compared against that of a Super-X divertor. It is found that the sensitivity of the location of detachment fronts in parallel space in the Super-X is significantly lower than that of the elongated conventional. Conversely, when tracking the fronts in poloidal space, there is little difference between the two configurations. This is in general agreement with the DLS model, which also predicts a significant reduction in front sensitivity in parallel but not poloidal space. This work marks the first time experimental data of detachment front movement has been directly compared to reduced modelling. Such work could be beneficial for enhancing detachment control algorithms, or designing alternative divertors around detachment control.

In Chapter 6, the studies and conclusions presented in this thesis are reviewed. Highlighted output from this work are two first author publications, and one co-author publication. Two of these documents are formed from work present in Chapters 2 and 3, and are [6], [7]:

> *Optimizing detachment control using the magnetic configuration of divertors*, by C. Cowley, B. Lipschultz, D. Moulton and B. Dudson. Nuclear Fusion. DOI: 10.1088/1741-4326/ac7a4c

and:

> *Predictive SOLPS-ITER simulations to study the role of divertor magnetic geometry in detachment control in the MAST-U Super-X configuration*, by O. Myatra, B. Lipschultz, D. Moulton, K. Verhaegh, B. Dudson, S. Orchard, A. Fil and C. Cowley. Nuclear Fusion. DOI: 10.1088/1741-4326/acea33

As for the second first-author publication, this was built upon a collaborative project at the *The Massachusetts Institute of Technology*, and focuses on development

work for the SOLPS-ITER code. This work is tangentially related to this thesis, as the code improvements were to allow for additional alternative divertor geometries to be simulated. However, it does not exactly fit with the themes of the rest of the chapters here, which mainly focus on isolating alternative divertor features and studying detachment access and evolution. Thus, the work for this paper is omitted from this thesis, but readers are invited to visit the original publication [8]:

> *Novel SOLPS-ITER simulations of X-point target and snowflake divertors*, by C. Cowley, A Q Kuang, D Moulton, et al. Plasma Physics and Controlled Fusion. DOI: 10.1088/1361-6587/acb4ba

Finally, the scope of future work is outlined in Chapter 6. This includes performing more complex simulations, to study the impacts of drifts or impurity transport, for example. One of the most interesting realms of future work is on developing further experimental studies for understanding detachment front movement and control. After all, the work presented in Chapter 5 is a starting attempt to understand the underlying principles of experimental detachment front movement. This work can be vastly improved through more statistically significant datasets, looking at a wider range of conditions, and using more diagnostics and techniques. In general, there are many possible avenues for extension and improvement in this work, as the daunting task of understanding divertor plasmas is far from complete; and the broader field of plasma physics and controlled fusion is as complex and captivating as ever.

Chapter 1

Introduction

1.1 The Need for Fusion

1.1.1 The Role of Energy in Society

The pursuit of scientific knowledge – though admirable in itself – is made more virtuous by its potential to progress life on Earth. When used for the right reasons, scientific advances have saved and improved countless lives, through new medicines, complex materials, and safer homes and methods of transportation. Perhaps the most important way in which science has fundamentally changed the quality of human life is through the development of efficient external sources of energy.

The role of external energy in human advancement has been present for 200,000 years, since prehistoric civilisations first harnessed fire for cooking and warmth [9]. As societies began to develop, animals such as horses and oxen were used for labour and transport, allowing for more agricultural output than humans could achieve using only their own biology [9]. Since then, advances such as the water wheel have progressively alleviated humans from excessive manual labour, allowing for more focus on advancement rather than survival.

Perhaps the most stark case of energy catalysing development is that of the industrial revolution. In less than one century, the advent of steam engines and turbines caused the efficiency of production in the US and Europe to soar [10]. As a result, GDP per capita growth, which remained fairly stagnant at 0.2 % for most of early human history, rose to highs of 1.3 % during the industrial revolution [10]. This growth in GDP was coupled with a monumental rate of progress of technological development, and a fundamental shift in human workload. In 1900, the percentage of the global workforce in the agriculture sector was more than 70% [11]. By 2019, this proportion dropped to 27%, and the service industry now comprises half the global labour force [12].

Today, a strong correlation between development indicators and energy consumption can be seen [13]. In fact, data from the International Atomic Energy Agency and the United Nations Development Programme show that countries with energy consumption rate per capita above 1.4 kW have a human development index 60% higher on average than countries with less than 1.4 kW energy consumption rate [14]. Moreover, countries which have an energy consumption rate per capita of 5

kW have a 10 times lower infant mortality rate on average, and roughly 4 more average schooling years than countries with a consumption rate per capita of 1 kW [15].

Of course, these relationships between energy and development are limited, as excessive and inefficient energy use does not contribute to economic or social development [16]. These relationships are also correlations, and do not necessarily provide insight into the underlying reasons for the improved development indicators with higher energy use. However, by examining current global statistics, and the history of energy and development, one clear conclusion emerges: development is strongly linked to a minimum energy usage. Thus it seems a minimum energy consumption is necessary for high development indicators, and a society which can focus on science, education, and healthcare with an alleviation of burden from manual labour. Though access to external energy sources seems a necessity for development, our current energy consumption has not come without adverse consequences and risks.

1.1.2 Climate Change

Prevailing among the consequences of human energy consumption is anthropogenic climate change, which refers to the increase in global average surface temperatures brought about by human activity. The most significant of these activities is the overconsumption of fossil fuels since the industrial revolution, which has led to a strong and rapidly growing increase in concentrations of carbon dioxide, methane, ozone, and nitrous oxides in the atmosphere. Figure 1.1 for example, shows carbon dioxide concentrations have almost doubled since before the industrial revolution, reaching 400 ppm, the highest recorded value in more than eight thousand centuries of records [17]. This has serious impacts on the climate because the aforementioned gasses are highly absorbing in the infrared (IR), which means a smaller proportion of the blackbody radiation from the surface of the Earth can escape the atmosphere, warming the planet. This effect of trapping radiation is known as the greenhouse effect, and the gasses that cause it are often referred to as greenhouse gasses [18].

Through increasing the concentration of greenhouse gasses in the atmosphere, fossil fuel-based energy sources already have a measurable effect on the global average surface temperature. This initial temperature change has also catalysed feedback mechanisms. Mechanisms such as the melting of ice caps, lowering the albedo of the Earth and exacerbating the temperature change further. Data from NASA indicates the global mean surface temperature has already risen 1.1 °C above its value in 1880 [19]. What's more, if countries follow historic emission trends, on a pathway the International Panel on Climate Change (IPCC) labels 'SSP2-4.5' shown in Figure 1.2 [20], this is predicted to lead to a warming of roughly 2.8 °C by the end of the century, as shown in Figure 1.3.

Modelling predicts stark consequences for the climate, biodiversity, and human welfare under 2 °C of warming, which worsen severely with a warming of 4 °C.

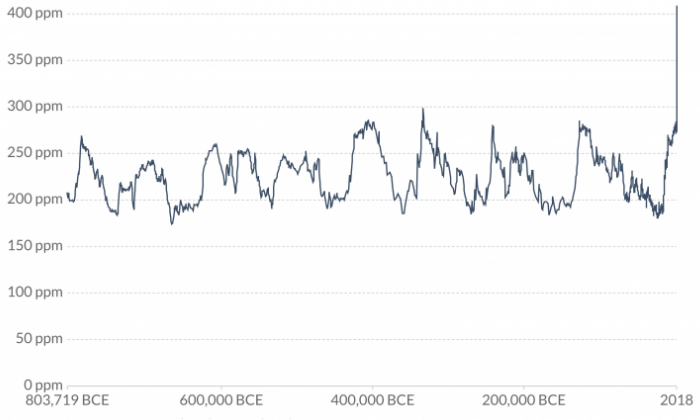

FIGURE 1.1: Historic annual carbon dioxide atmospheric concentrations [17].

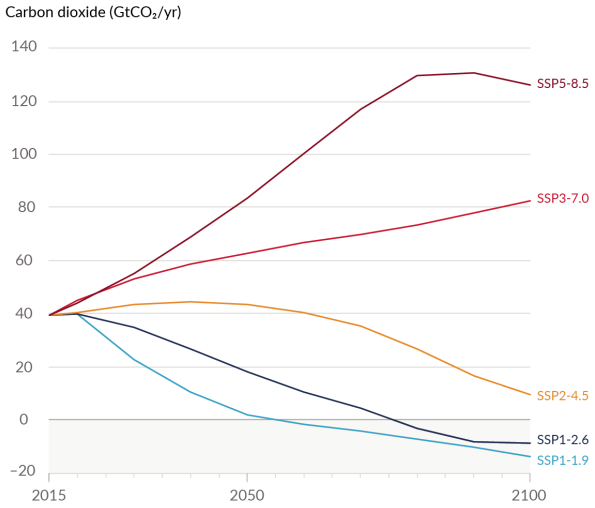

FIGURE 1.2: Annual carbon dioxide emissions for five IPCC emission pathways [20].

In terms of climate, antarctic sea ice extent is currently decreasing by an alarming rate of 12% per year [21]. Current warming trajectories could cause melting severe enough to make arctic summer waters ice free by 2050 [22], and will reduce global glacier mass by 18% [23]. As a consequence, sea levels are expected to rise by roughly 0.75m by 2100, to flood an area containing between US $ 7.9 and US $ 12.7 trillion in global assets [23], and displacing millions. Under the same SSP2-4.5 pathway, this sea level rise is predicted to double to 1.5m by 2300 [24].

In terms of agriculture and vegetation, the significant effects of climate change can already be seen, as 59% of global vegetation is showing a reduction in growth since the 1990s [25]. This is predicted to worsen over the coming years, and by 2050 the proportion of agricultural area that will become unsuitable is 10%; a number which may rise to 30% by 2100 under SSP5-8.5 [23]. Moreover, With 2 °C warming, land area burned by wildfire is expected to increase by 35 %. In terms of species biodiversity, 10 % of species assessed by the IPCC face a very high risk of extinction

at 2 °C of warming, which rises to 12% at 3 °C warming.

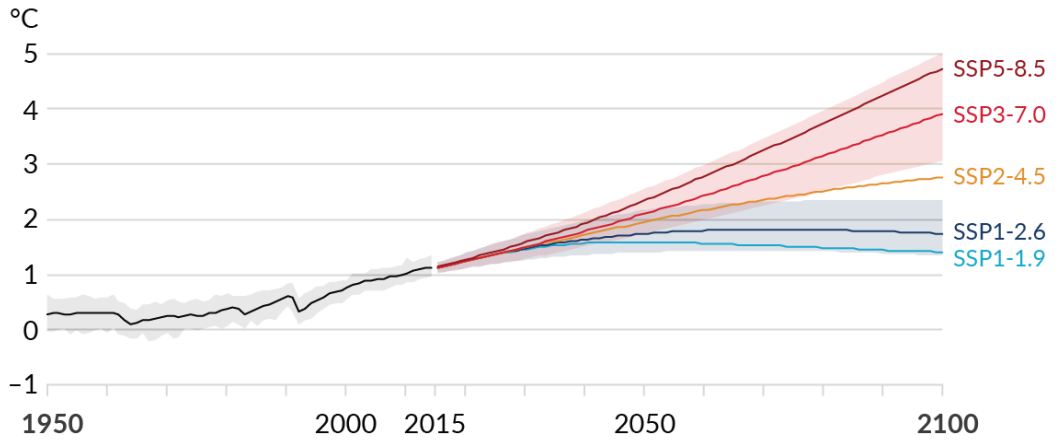

FIGURE 1.3: Global surface temperature change relative to 1850-1900, predicted for various IPCC emission pathways [20].

The climate crisis, however, will not just affect economics and biodiversity, but is expected to cause an unprecedented loss of human life. Under the 'SSP2-4.5' pathway, over 9 million excess deaths will be caused by 2100 due to direct temperature increases alone (not considering effects of disease, food supply, and war), which increases to 83 million deaths under 4 °C of warming [26]. This represents the same amount of deaths than have been caused by all major armed conflicts from 1740-1974, including both world wars [27].

Despite this sombre outlook, these consequences of climate change can be mitigated by immediately and imperatively decreasing global greenhouse gas emissions. By following pathway 'SSP1-1.9' for example, global warming could be kept to 1.5 °C or under by the turn of the century. Following this pathway, however, requires sweeping changes in our energy infrastructure, electrifying agriculture and transport, and moving towards entirely low-carbon sources of electricity and industrial heat.

1.1.3 Energy Security

Though anthropogenic climate change is perhaps the greatest risk of fossil-fuel dependence, it is by no means the only risk. The lack of energy security and national energy independence is a growing and considerable concern, since the global supply of fossil fuels are now heavily dependent on only a handful of producers. In fact, 40,000 TW hr of natural gas was consumed globally in 2021 [28], but 40 % of this was produced by just two countries: the United States and Russia. Similarly, 51,000 TW hr of oil was used in 2021 [28] but 36 % of the supply originates from just four countries: the United States, Saudi Arabia, Iraq, and the United Arab Emirates.

As a result of the growing lack of energy security, there have been several economic crises caused by variability of fossil fuel suppliers. Chief among these is the 1973 oil crisis, sparked by the Yom Kippur War, a conflict between Israel and an

Arab coalition led by Egypt and Syria in October 1973 [29]. As a result of this war, the Organization of Arab Petroleum Exporting Countries introduced an oil embargo in 1973 targeting Israel-supporting nations such as the US and the UK. The embargo caused an increase in oil price of nearly four times, from $2.90 to $11.65 after the embargo in 1974 [30]. Coupled with the effects of the Vietnam war, this led to the most significant economic crisis in the US since the great depression, with unemployment rising to 9 % in 1975 [31]. Inflation also increased from 3 % in 1972 to 12 % in 1974 in the US, and GDP shrunk by 2 % in 1974 [32].

Another key example of consequences of energy insecurity is the economic fallout of the Ukraine-Russia conflict of 2022. In February 2022 Russia began a full-scale invasion of Ukraine, and was met with international condemnation and sanctions [33], [34]. In response to sanctions from the West, Russia threatened to cut off its supply of natural gas to certain EU member states. This decrease and uncertainty in supply caused a skyrocketing in gas prices, particularly in Europe. In the 12 months preceding December 2022, UK gas prices rose by 128.9 % and electricity prices rose by 65.4 % [35]. This was a main driver of inflation, and annual consumer price index inflation peaked at 11 % in October 2022, the highest rate on record [36].

Whenever a country is hit with a strong fiscal crisis, it is often the poor and vulnerable who are impacted the hardest. In fact, modelling from The Economist estimates higher energy prices brought about by the Russian invasion of Ukraine caused over 68,000 deaths in Europe in the Winter of 2022/2023 [37]. The onset of financial crises is associated with an increase in poverty and income inequality, most acutely affecting the most vulnerable [38]. As a consequence, it is important from the perspective of human welfare to avoid these crises, by fostering a supply of energy which is more independent of geopolitics.

1.1.4 Alternative Energy Sources

By now it should be clear that there is a dire need for sweeping changes in our supply of energy. Transitioning to a reliable, highly available, and low-carbon energy supply that does not greatly depend on natural resources is not desirable, but vital. Of course, for years there have been a plethora of excellent scientific and social remedies to the energy crisis. Specifically, the advent of renewable energy sources such as hydroelectric, onshore and offshore wind, solar, and geothermal energy have reduced our dependence on fossil fuels. Indeed, nearly 30 % of global electricity consumption now comes from renewables, a number expected to increase to 60 % by 2030 [39].

However, every power source has its drawbacks, and relying too heavily on a handful of renewable energy sources may be costly. This is because many renewables such as wind and solar vary in their generating output; from minute to minute, to diurnally and seasonally. Of these, significant seasonal variation is the most difficult to compensate for. In Canada and the Netherlands, solar generation output can vary by a factor 6 seasonally [40], and the generating output of wind in Europe has

been shown to vary seasonally by a factor 1.5 [41]. To counteract these variations, a world powered entirely by renewables would either need a highly connected grid (from Norway to the Equator), investment in long-term storage such as artificial fuels, a generation capacity vastly over the average use, or a combination of the three [40].

Each proposed method of dealing with seasonal variability, however, typically decreases the efficiency of the grid and adds cost; particularly when approaching a 100% renewable grid. In fact, a study modelling the cost of renewable penetration in the US found that in the highest cost models, achieving a 100% renewable grid would have 60% higher system costs than a grid which had no requirement on renewable penetration [42].

Notwithstanding, if nuclear energy is included in these renewable grids, models predict a much lower (roughly 10 % [42]) increase in system cost. This illustrates that nuclear power, which is highly reliable, can be a cost-effective way of generating power when conventional renewables experience intermittency. And if nuclear can help a renewable grid be more cost effective, this increases the chances of transitioning to renewables faster. The reverse can be seen in Germany, which recently decided to completely phase out its nuclear reactors. As a result, Germany is still highly reliant on fossil fuels, despite a growing renewable industry and reduction in energy consumption. In fact, in 2022, German electricity generation from coal *increased* by nearly 10 % [43].

Though nuclear fission has great potential to contribute to decarbonisation and energy security, it also has its disadvantages. A conventional 1 GW uranium fission reactor, for example, produces 30 tons of high-level radioactive waste per year, which requires costly long term storage [44]. Additionally, at the current rate of consumption, the reasonably assured resources of fissile uranium will be depleted in 100 years [45]. These uranium resources may also cause energy security risks in the long term, since over 75% of global uranium is produced by just four countries: Kazakhstan, Canada, Australia, and Namibia [46]. Because of this, it is desirable to have a transition in the long term to a low-carbon source of power which has the reliability of fossil fuels or fission, but without the prolonged issues of either. One of the most promising candidates for such an energy source is nuclear fusion.

1.2 Introduction to Nuclear Fusion

1.2.1 Nuclear Fusion

Though humanity has considered a plethora of methods of energy generation, most of these methods truly begin with energy from the sun. Whether it be directly from solar cells, or from combusting long-dead fauna which once basked in solar radiation, our energy supply consists of a chain of conversion processes that begin with

nuclear interactions in the sun. It is only in the last century that we thought of skipping these intermediate processes and building our own power-generating star on Earth, by harnessing and controlling nuclear fusion.

Nuclear fusion is the process by which nuclei from several atoms combine and fuse together to create a single more massive nucleus. In doing so, this process can release energy, which is how fusion is able to power the sun and every other active star in the universe. Principally, the energy released by fusion stems from the strong interaction, the fundamental force that binds quarks into nucleons, and nucleons into nuclei [47]. Every nucleus held together by the strong force has an associated binding energy; the energy required to break apart the nucleus into its constituents. When nuclei are broken into their constituent nucleons, then reformed into different elemental nuclei, the end products can have a different binding energy than the initial nuclei. This will release energy, if the binding energy per nucleon is higher for the product than it is for the reactants.

Figure 1.4 [48] shows the binding energy per nucleon of common elemental nuclei. This figure illustrates that for the majority of atomic numbers higher than iron, breaking nuclei apart will release energy. This is the process of nuclear fission, and is the source of power for present-day nuclear reactors. For certain nuclear transitions below iron, however, creating larger nuclei from smaller ones (such as the transition from H_1^2 to He_2^4) releases energy. This is the process of nuclear fusion, and per reaction, can be significantly more energy dense than fission, as can be seen in Figure 1.4.

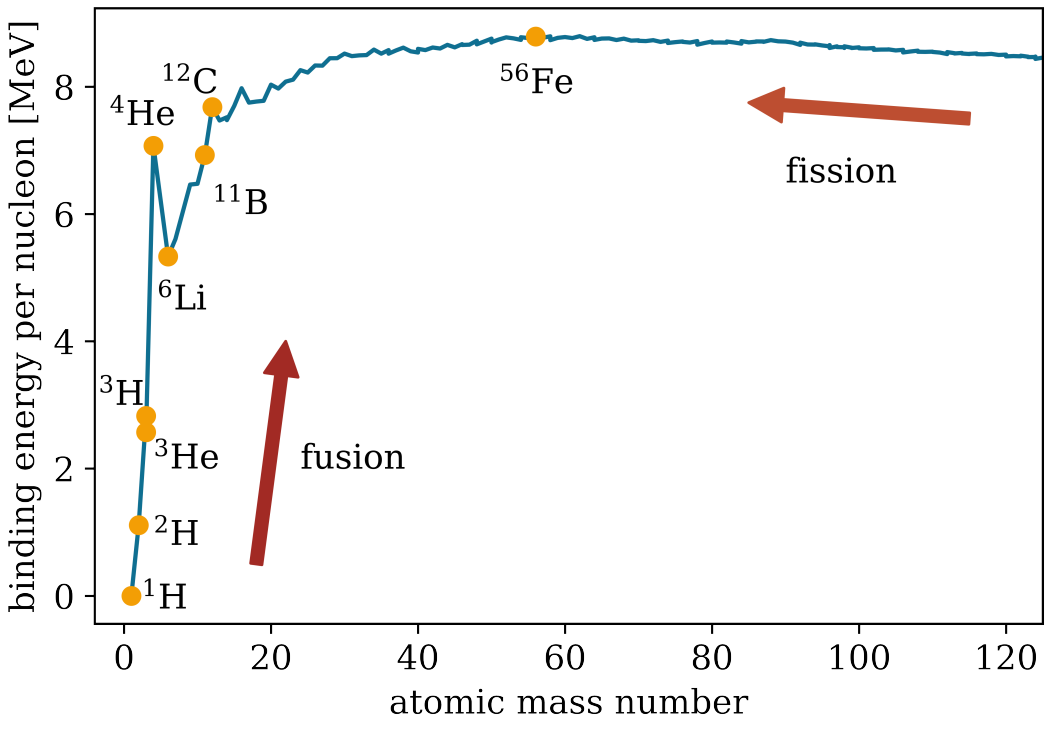

FIGURE 1.4: The binding energy per nucleon as a function of atomic mass number for some common nuclei.

Though fusion reactions are significantly more energy dense than fission, they are also monumentally less likely to occur. This is because fusion requires two positively charged nuclei to combine; nuclei which feel a tremendous force of electrostatic repulsion between each other. Fusion reactions are so unlikely, in fact, that if we collected all the hydrogen atoms in the observable universe, and contained them with 1 atmosphere of pressure, the total fusion power output wouldn't be enough to power a light bulb. So how is the sun much stronger than a light bulb, and how can we get nuclei on Earth to do the same? The first step is to give the fuel nuclei sufficient energy to overcome (or tunnel through) the Coulomb barrier. This is usually done by heating the fuel until it transitions into the state of matter that comprises the sun: a plasma.

1.2.2 Plasma Physics

Under any thermonuclear fusion scheme, the fuel must be heated to at least the KeV level, or roughly 10°C million. At this point, gasses become ionised; the majority of atoms separate into ions and electrons, forming a plasma. A plasma can be described as a combination of electrons, the ions, and neutrals, with density and temperature n, T; n_i, T_i; and n_0, T_0 respectively. For the remainder of the thesis, temperatures will be expressed in eV.

Because the fuels of fusion energy are in the plasma state, the physics of plasmas is fundamental to the study of nuclear fusion. This is particularly true for this thesis, which is first and foremost a study in plasma physics. As such, it is first important to define a plasma, and describe the unique properties that they possess. A fundamental characteristic of plasmas is ionisation, and plasmas can range from weakly to partially to completely ionised, depending on what fraction of the atoms have been separated into ions and electrons.

The presence of charged particles caused by ionisation leads to the most crucial property of a plasma: collective behaviour. Collective behaviour refers to the fact that the charged particles in the medium are unbound and influence each other through their charges, and thus the plasma can respond to perturbations in the electromagnetic field [49], [50]. The characteristic timescale of this collective behaviour is defined by the (electron) plasma frequency [49], [51]:

$$\omega_p = \sqrt{\frac{ne^2}{m\epsilon_0}}, \tag{1.1}$$

where m is the electron mass and ϵ_0 is the vacuum permittivity. In addition to this timescale, a length scale of this collective electromagnetic behaviour can be described. This length scale stems from charge screening, a phenomenon by which the potential of a free charge is screened by surrounding particles of the opposite charge. The length scale of this potential screening, and hence the length scale under

which plasma particles may interact electromagnetically with each other, is defined by the Debye length [49]:

$$\lambda_D = \sqrt{\frac{\epsilon_0 k_B T}{ne^2}}. \tag{1.2}$$

Due to this charge screening, at length scales much larger than the Debye length, the plasma is effectively neutral. This property by which plasmas are locally charged but macroscopically neutral is known as quasi-neutrality [49], [52].

The final important aspect of collective behaviour is how significant it is relative to the fluid properties of the plasma. The statistical importance of collective behaviour is described by the plasma parameter, Λ, which is a measure of the number of electrons in a sphere of radius equal to the Debye length [49]:

$$\Lambda = \frac{4\pi}{3} n \lambda_D^3. \tag{1.3}$$

When this plasma parameter is much less than 1, this means the Debye sphere is sparsely populated. Such a plasma is described as strongly coupled, and in such a plasma the collective behaviour is less important than particle collisions. Contrarily, a plasma with Λ much greater than 1 is a weakly coupled plasma, in which many charged particles exist within a Debye sphere and collective behaviour is dominant [50]. The plasmas dealt with in magnetic confinement fusion are weakly coupled plasmas.

The three collective behaviour parameters ω_p, λ_D, and Λ are in many ways the most important parameters of a plasma. Yet they are by no means the only important quantities. One property which is important and reoccurring in this thesis is that of collisionality. Collisionality is a measure of how frequent particle collisions are relative to the observational length scale. Though the dimensionless collisionality of various plasmas can have different definitions, the definitions always involve the collision frequency of two species in a plasma. This collision frequency ν of test particle 1 on bulk medium 2, is defined by [49], [52]:

$$\nu_{1,2} = \left(\frac{q_1 q_2}{\epsilon_0 m_1}\right)^2 \frac{n_2 \ln\Lambda}{4\pi (m_r/m_1) \mathrm{v}_1^3}, \tag{1.4}$$

where q_1 and q_2 are the charges of the two species, n_2 is the density of the bulk medium, v_1 is the speed of the test particle, m_1 is the mass of the test particle, and m_r is the reduced mass of the two particles. It is important to note that in a weakly coupled plasma, the plasma frequency is much greater than the electron-ion collision frequency. However, the importance of plasma collisionality extends past this, as it describes how frequently energy is distributed between particles and species. For example, the collisionality can strongly affect the heat conductivity of a plasma. Additionally, highly collisional species will converge to a Maxwellian distribution of energies, and if two species are very collisional, they will equilibrate to the same temperature.

1.2.3 Confinement

The first step in achieving efficient nuclear fusion on Earth is creating a hot plasma, but this is by no means the only step. To illustrate what other factors are required, consider the total fusion power output in a mixture of two fuels of ion density $n_{i,1}$ and $n_{i,2}$, which is given by [53]:

$$P_{fusion} = E_{fusion} n_{i,1} n_{i,2} \langle \sigma \mathrm{v} \rangle . \tag{1.5}$$

Here σ is the reaction cross section, a measure of the probability of a successful fusion reaction, and E_{fusion} denotes the energy released per reaction. v is the relative velocity of the two reactants, and $\langle \sigma v \rangle$ is the distribution-averaged product of cross section and velocity, also known as the reactivity. To find the total power output one must also consider the power lost from the fusion fuel, which can be related to the thermal energy density and a so-called energy confinement time τ_E [53]:

$$P_{loss} = \frac{\frac{3}{2}(n_e T_e + n_{i,1} T_i + n_{i,2} T_i)}{\tau_E}. \tag{1.6}$$

From these equations some requirements for efficient fusion can be gathered. First, it is clear the choice of fuel is important, as E_{fusion} and $\langle \sigma \mathrm{v} \rangle$ vary with fuel mixture. In particular, a fuel mixture which has a high E_{fusion} is desirable, but also a sufficiently high reactivity at low enough temperatures, such that losses can be minimised. A plot of reactivities against temperature for multiple candidate fusion fuel mixtures is shown in Figure 1.5. From this figure, the fuel mixture Deuterium-Tritium (D-T) has the highest reactivity peak, and peaks at lower (40 KeV) temperatures than other fuels. Because of this, D-T is the most commonly used fuel mixture, with nuclear equation:

$${}^{2}_{1}D + {}^{3}_{1}T \rightarrow {}^{4}_{2}He\ (3.5\ \mathrm{MeV}) + {}^{1}_{0}n\ (14.1\ \mathrm{MeV}). \tag{1.7}$$

Though D-T has high reactivities, it also comes with pragmatic issues. Crucially, tritium is not naturally occurring, and is radioactive and can easily contaminate water. Additionally, D-T fusion produces high energy neutrons, meaning reactors must be built to withstand high neutron fluxes and the nuclear damage sustained as a consequence. Now under the case of D-T fusion with a 50/50 fuel mixture, and equal temperature for all ions and electrons, Equations 1.5 and 1.6 become

$$P_{fusion} = E_{fusion} \frac{1}{4} n^2 \langle \sigma \mathrm{v} \rangle , \tag{1.8}$$

and

$$P_{loss} = \frac{3nT}{\tau_E}. \tag{1.9}$$

From these equations it becomes clear that - apart from a good choice of fuel - a high density of reactants is required, as fusion power scales with n^2, whereas losses

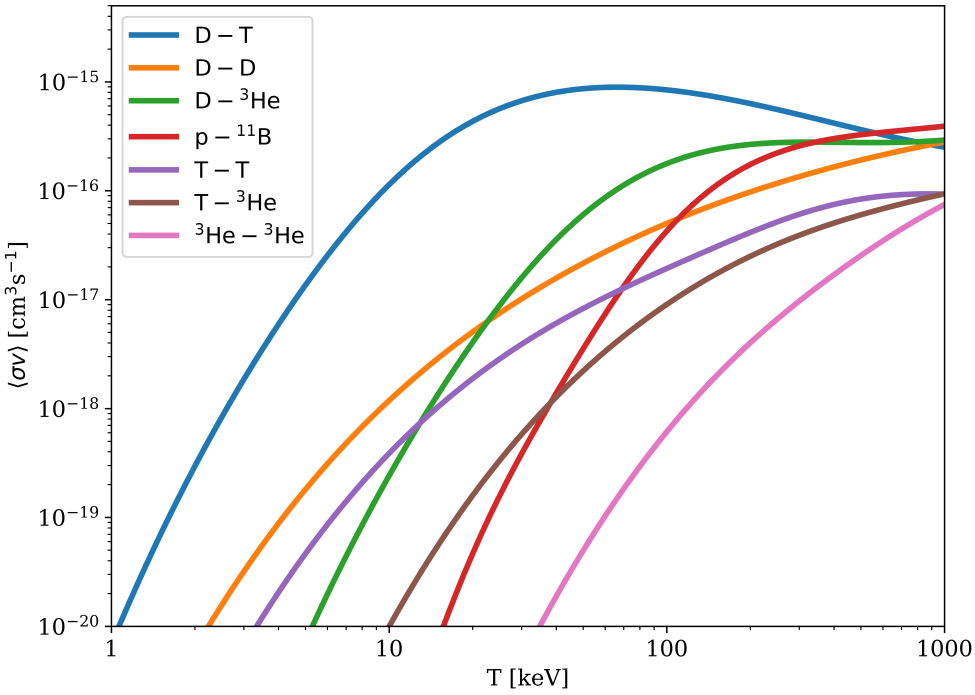

FIGURE 1.5: The reactivities of seven common fusion reactions, plotted as a function of centre-of-mass reactant temperature [54].

scale only linearly with n. Furthermore, a high temperature is required to maximize reactivity. For D-T fusion this means achieving ion temperatures in the tens of KeV. Finally, to reduce losses the energy confinement time should be maximized. Because of these three requirements of high density, high temperature, and high confinement time, a common figure of merit for nuclear fusion devices is the so-called 'triple product', $nT\tau_E$.

In summary, to achieve economic fusion on Earth requires confining both particles and energy in a high pressure fusion plasma. This confinement effectively means keeping the plasma away from external material, preventing the fuel or energy from leaking out. Thus the ideal picture of a confined plasma is one which has a very high pressure at the centre which drops off to a very low pressure at the edge. This strong pressure gradient, however, will produce a strong force, pushing the plasma outward like air pushes against the rubber of a high-pressure balloon. In order to prevent loss of heat and particles, there must be either be a strong counteracting force or a considerable reduction in outward transport.

Of course, a balloon has the benefit of the tension of rubber, and the sun has 10^{30} kg of mass creating strong gravitational forces counteracting the pressure gradient. In a man-made fusion reactor, however, there is no material that can withstand contact with the high-temperature plasma directly, and there is not nearly enough material to create a noticeable gravitational field. So what other methods could be

used to confine a fusion plasma? There have been a number of proposed methods of generating this confinement, including using an inward driven shock to rapidly heat and compress a fuel. This approach is known as inertial confinement fusion [55]. However, by far the most well-researched method is by magnetically confining a plasma using a tokamak.

1.2.4 Tokamaks

The fundamental basis of a tokamak is to use magnetic fields to achieve the confinement required for nuclear fusion. Specifically, a tokamak leverages the fact that the motion of a charged particle in a magnetic field orbits magnetic field lines [49]. So for a plasma in a magnetic field, the only way particles or energy can be transported perpendicular to the magnetic field is through collisions with other particles. The radius of a particle's guiding centre orbit is inversely proportional to magnetic field strength, and as a consequence a strong magnetic field **B** can massively reduce inter-particle collisions, and confine the transport of the plasma to the parallel (to the magnetic field) direction.

So by leveraging strong magnetic fields, the transport of heat and particles can be reduced, but not in the direction parallel to the magnetic field. To nullify this transport, the ends of the plasma can be connected together, creating a loop in the parallel direction, and effectively negating bulk parallel transport. This is the idea of a tokamak (shown in Figure 1.6), a toroidal device with a set of toroidal field coils applying strong toroidal field applied to the plasma, B_{tor} [56]. In such a picture, however, the magnetic field is much stronger on the inside of the toroid than the outside, and the drifts caused by this magnetic gradient cause ions and electrons to separate vertically [49], [56]. This charge separation leads to an electric field **E**, causing a bulk drift of the plasma towards the outside of the device, and degrading confinement. To remedy this, a poloidal magnetic field can be introduced, B_{pol}. The resultant total field B shown in Figure 1.6 is then helical, and forces the charged particles to rotate poloidally; effectively short-circuiting the vertical charge separation.

This poloidal field is generated by inducing a current in the plasma, typically by leveraging a time varying current in a set of coils nearby, known as the central solenoid (shown in Figure 1.6). However, only using a central solenoid effectively means pulsed operation, since the current cannot be indefinitely increased in these coils. For true steady-state operation, non-inductive current drive is required; for example, from bootstrap current or radio-frequency current drive [57], [58].

When discussing the fundamental picture of a tokamak, it is important to keep clear the purpose of each set of magnetic coils. Here the toroidal field was introduced as the only field which leads to confinement, but that is not strictly true. A toroidal device with solely a poloidal field can also lead to confinement. In such a picture, however, the plasma is prone to instabilities such as the sausage and kink instability [56], [59] which are detrimental for the confinement of plasma. Fortunately, these instabilities can be suppressed by applying a toroidal magnetic field to the plasma

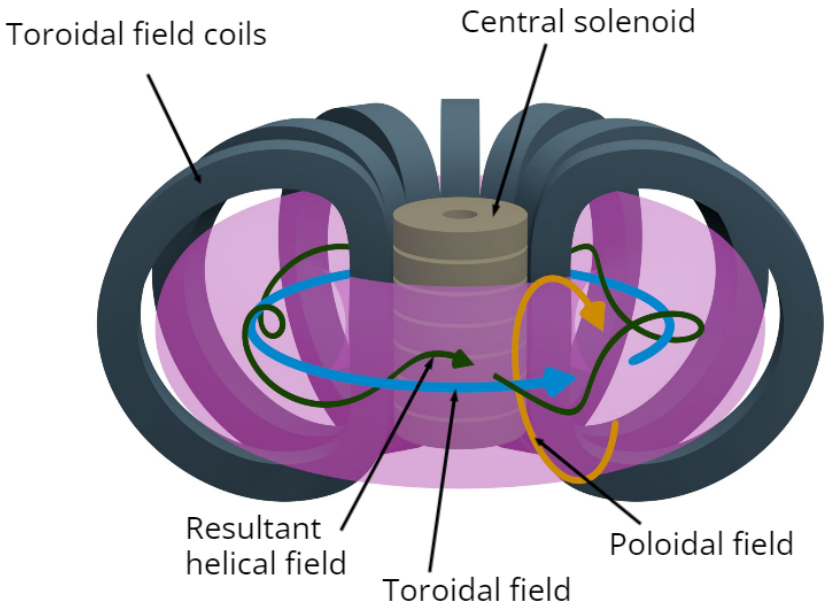

FIGURE 1.6: A conceptual diagram of a tokamak.

[59]. So both fields have their separate purposes; both can lead to confinement, the toroidal field stabilises certain instabilities, and the poloidal field prevents the formation of a vertical electric field.

In the picture of a tokamak in Figure 1.6 the radius of the toroidal column of plasma is known as the minor radius a, and the distance between the plasma column and central axis is the major radius, R. Now in real operational tokamaks, this simple picture becomes much more complex. Each of the broad design complexities, and the motivations behind these additions will be discussed throughout the following section.

One of the most important nuances to a real tokamak is the magnetic field structure. In contrast to the simple picture introduced previously, operational tokamaks modify the poloidal field using external coils for vertical stability. Additionally, the poloidal field is modified to shape the divertor, the magnetic structure used to control plasma exhaust.

In addition to the magnetic field coils, tokamaks also need sources of power and particles that allow the high pressures needed for fusion to be accessed and maintained. Deuterium and tritium can either be injected as gas or if the plasma temperatures are too high for gas to penetrate into the core, frozen pellets of fuel can be injected instead [60]. For reactor tokamaks, pumps are also required to facilitate density control and pump out the helium ash produced by fusion reactions in the core [61].

In terms of heating, moderate temperatures can be achieved through ohmic heating from the plasma current. However, this becomes inefficient at higher temperatures due to the scaling of resistivity with temperature [56]. Beyond this, a myriad of systems have been proposed and implemented, such as Neutral Beam Injectors

(NBIs) [62], and Radiofrequency heating (including Electron-Cyclotron Resonance Heating (ECRH), and Ion-Cyclotron Resonance Heating (ICRH) and lower hybrid [63]).

Surrounding the actual plasma itself are the strong, heat-resistant plasma facing material of the first wall, typically made of materials such as tungsten or beryllium. Beyond this lies the breeder blanket, whose purpose is to absorb the neutron products of the D-T reactions [64]. Since most of the fusion power in D-T fusion is outputted through neutrons, the blanket is an important component in heat capture and conversion. Moreover, the blanket can be used to breed more tritium for the fuel cycle. In order to do so, the blanket must contain lithium, and blanket material candidates include liquid lithium-lead, water cooled lithium-lead, and the helium-cooled pebble bed [64]. This section of the tokamak may also include diagnostics to monitor the machine and contribute to scientific understanding.

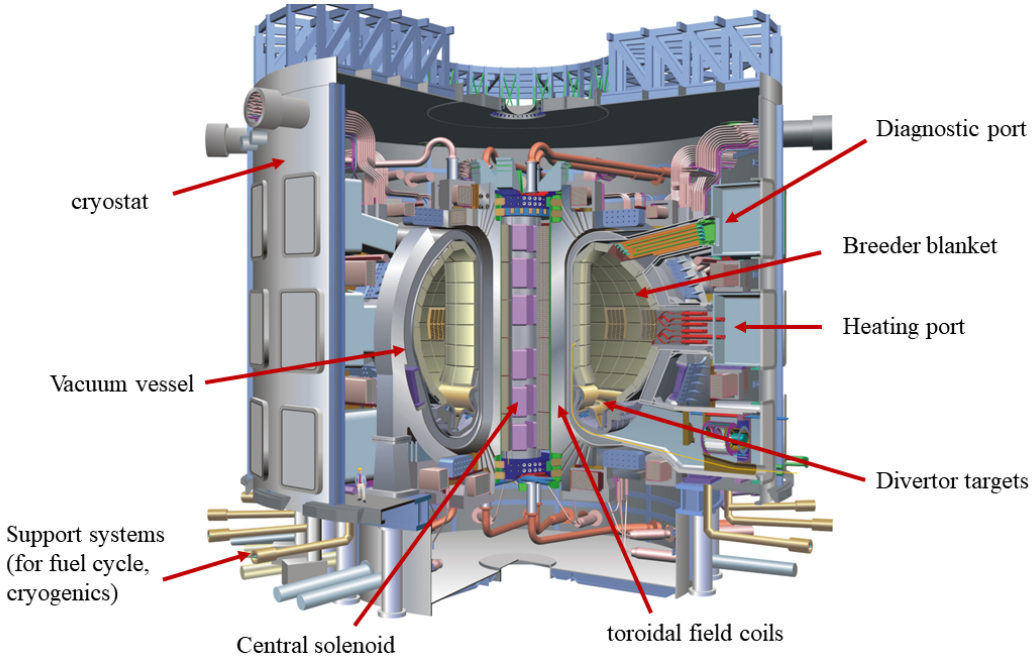

FIGURE 1.7: A cutaway diagram of the ITER tokamak. Image modified from [65].

By this point it should be clear that tokamaks in reality are exceedingly complex devices that have hundreds of different systems that must work well in unison. Currently there exist dozens of tokamaks across the globe, including the under-construction ITER project, shown in Figure 1.7. These tokamaks range in important characteristics such as machine power, size, magnetic field strength, and aspect ratio. Standard aspect ratio tokamaks have a much larger major radius R than minor radius a, whereas spherical tokamaks have more comparable major and minor radii. Principal standard aspect ratio tokamaks include the Joint European Torus (JET) [66] in the UK, the Axially Symmetric Divertor Experiment-Upgrade (ASDEX-U) in Germany [67], Japan Torus-60 (JT-60) in Japan [68], Doublet III-D (DIII-D) in the US [69], and Tokamak à Configuration Variable (TCV) in Switzerland [70]. Major spherical

tokamaks include the Mega-Ampere Spherical Tokamak-Upgrade (MAST-U) [71], and the National Spherical Torus Experiment-Upgrade (NSTX-U) [72].

Noting the wide collection of tokamaks operating today, one may ask why fusion is not powering the grid yet. The short answer is that fusion is difficult, and no tokamak has yet achieved a triple product high enough to sell electricity to the grid. Reactor and reactor-like tokamaks are being designed and built today to demonstrate fusion gain; devices such as the international collaboration ITER [65], [73] (under construction in France), SPARC (being built by the private US company Commonwealth Fusion Systems) [74], the Spherical Tokamak for Energy Production (STEP, being designed by the UK government) [75] and DEMO [76]. However, there is still a multitude of scientific challenges to be solved before fusion energy is economically viable, including finding advanced confinement regimes [77]–[79], verifying the tritium fuel cycle [80], and disruption mitigation [81]. This thesis focuses on just one potential solution to one particular challenge of tokamak operation: the plasma exhaust [82].

1.3 Plasma Exhaust and Divertors

1.3.1 Divertors

In any tokamak, no matter how well confined the plasma is, there will inevitably be plasma escaping from the core, eventually making contact with surrounding material. Even if perfect confinement existed, it would not be desirable, since the helium produced by fusion reactions must leave the core and be pumped away from the machine. As such, reactors must be designed with a good plasma-material boundary region in mind. For this reason most tokamaks operate with a divertor [56], a poloidal magnetic structure which diverts plasma particles escaping radially from the core and towards target plates, as can be seen in Figure 1.8. These divertor target plates are typically made of strong, heat-resistance material such as carbon or tungsten (though tungsten is the leading candidate for reactor tokmaks) [82].

The primary benefit of operating with a divertor is that the plasma-material boundary can be located physically far from the core (in contrast to a limiter configuration, where the surrounding material is in direct contact with the core plasma boundary). This has two main benefits: first, particles escaping from the core are forced to travel a much longer distance before they reach the targets, acting like insulation, and allowing a larger temperature drop between the core and targets [83]. Second, any sputtered material from the targets is less likely to penetrate and contaminate the core [84].

This thesis will focus chiefly on divertor plasma physics, which deals with understanding the transport of plasma and heat in the divertor. Although this realm of physics is complex, and will be covered extensively in further chapters, the simple picture can be introduced here. This picture starts with the core, which typically has

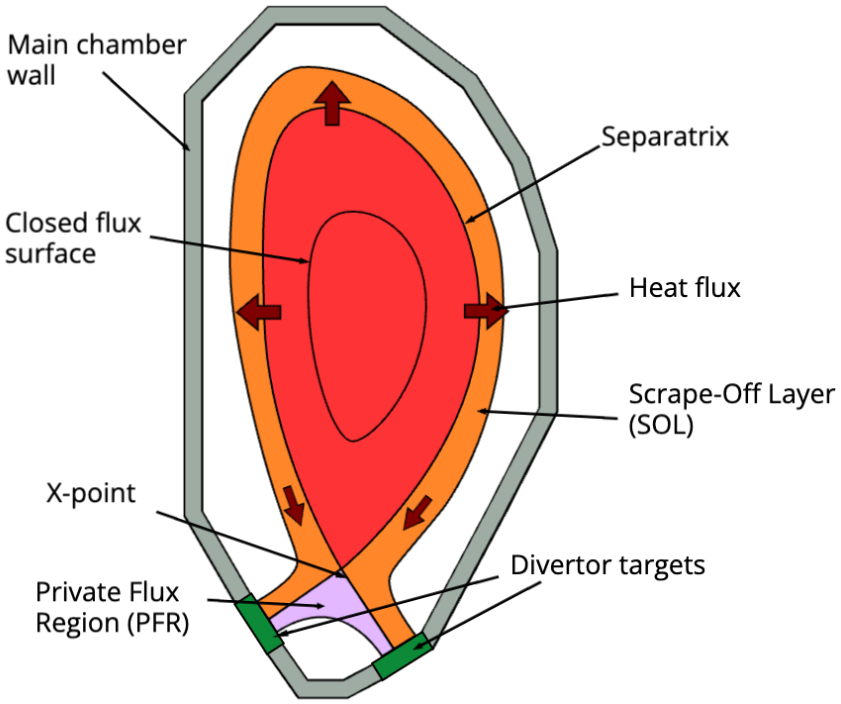

FIGURE 1.8: A conceptual diagram of a conventional single null divertor.

a relatively flat pressure profile, fuelled by gas or pellet injection and heating systems. In low confinement, or L-mode, there are shallow drops in temperature and density from the core to the edge. With sufficient power, however, the machine can enter high-confinement, or H-mode. In such a mode the core is separated from the edge by the pedestal, a region of reduced cross-field transport [85], and significant gradients in plasma pressure. In present-day devices, plasma pressures can drop from 10 kPa to a few hundred Pa through this pedestal region [86].

Further outward from the pedestal top the closed field lines of the core terminate and the open field lines of the Scrape-Off Layer (SOL) begin. The separatrix is the first open flux surface, and defines the boundary between the core and SOL, shown in Figure 1.8. The separatrix is often used interchangeably with the last closed flux surface, and though they are located at the same boundary, the separatrix defines the SOL side of this boundary, whereas the last closed flux surface defines the core side.

The power and plasma entering the SOL, P_{SOL}, comes from radial transport past the pedestal region. It is important to note that the majority of plasma being radially transported into the SOL emerges on the outboard side (higher major radius) of the core, since here turbulent instabilities are enhanced by the magnetic field curvature [52]. Consequently, the outboard divertor typically receives the majority of heat and particles (though this does not necessarily mean the peak heat fluxes will be worse on the outboard).

As a result of the open magnetic field lines in the SOL, plasma entering the

scrape-off layer is transported in the parallel direction towards the divertor targets. The competition between parallel and perpendicular transport leads to a cross-field decay in plasma temperature, density, and parallel heat flux $q_{||}$. The characteristic length scales of these decays are denoted by λ_T, λ_n, and λ_q [83]. These lengths are crucial in governing the plasma exhaust challenge in the SOL, as the peak heat flux entering the divertor scales inversely with λ_q.

When plasma enters the SOL it is transported in the parallel direction, starting from what is called the 'upstream', and towards the divertor targets, which is termed the 'downstream'. As this occurs, heat and particles are also transported radially, particularly to the cold Private Flux Region (PFR) shown in Figure 1.8. As a consequence, as the plasma approaches the target, parallel heat flux profiles broaden, and the peak heat flux both drops in magnitude and moves further into the SOL (away from the PFR). Additionally, with a fixed upstream temperature parallel conducted heat necessitates a drop in temperature towards the targets. The drop in temperature is related to the connection length $L_{||}$, defined as the parallel length along the separatrix from the upstream (typically the outer midplane) to the target.

A drop in temperature along the SOL corresponds with an increase in density if there is no large sink of plasma static pressure [83]. As such, the plasma at the divertor targets is lower power, lower temperature, and higher density and higher collisionality than the plasma upstream. Once the plasma reaches the target, it may recombine at the surface of the material, and recycle back into the main plasma. However, some plasma particles can also become trapped in the material, and some material particles can be sputtered into the plasma, affecting the plasma profile upstream [84].

Through this broad description of divertor plasma physics, one idea should become very clear: that divertor physics stands at the interface of many areas of study. The boundaries of divertors extend to the hot core at one end, and low-temperature solid materials on the other; the SOL is fed by cross-field transport, yet within it parallel transport dominates; in many cases, the opposite ends of the SOL can contain highly collisionless plasmas, and highly collisional partially ionised gasses. Because divertors lie at a fascinating junction of different areas of physics, they are exceedingly complex to fully understand. However, this is also what makes them fertile ground for study.

1.3.2 The Exhaust Challenge for Reactors

In the most high-performance present day tokamaks, heat and particle loads on divertor targets are high, but manageable. However, planned tokamaks of the future pose a significant challenge for the plasma facing materials. The reason for this is twofold. First, as tokamaks transition to reactor and reactor-like machines, the output power is expected to increase significantly, since producing power is the fundamental purpose of reactor tokamaks. ITER, for example, is expected to produce 500 MW of fusion power [73], and the output power of DEMO is expected to be of order

2 GW [76]. This power is more than one hundred times greater than the maximum fusion power output from present-day devices [87].

Secondly, reactor-like tokamaks are expected to operate with higher magnetic fields, since this leads to better confinement. However, better confinement means that plasma is also tightly confined within the SOL, leading to lower SOL heat widths and higher peak heat fluxes. Figure 1.9 shows a multi-machine scaling of divertor heat flux widths with midplane poloidal magnetic field strength. This scaling shows a decrease in heat flux width with poloidal field. Using this scaling, SPARC's λ_q will be $\simeq 0.3$ mm [88], and ITER's will be $\simeq 1$ mm (though turbulence modelling suggests the true ITER SOL width could be larger than that predicted by empirical scalings [89]). With these predicted heat flux widths, unmitigated parallel heat fluxes entering the divertor are expected to approach the GWm^{-2} level. Of course, the target heat loads can be significantly reduced by varying the striking angle of the plasma (both toroidally and poloidally), but these deposited heat flux can still be in the 100 MWm^{-2} range. This would cause significant damage, even to tungsten monoblock tiles developed for ITER, which are rated for a 15 MWm^{-2} maximum steady-state heat load [82].

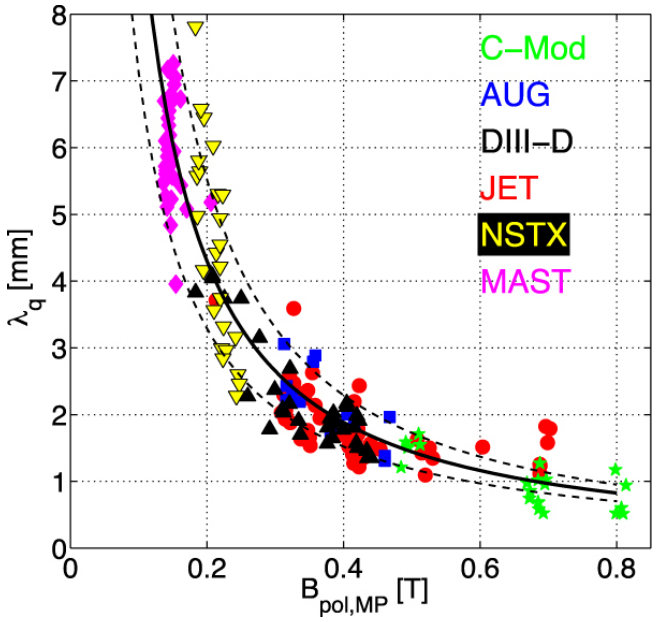

FIGURE 1.9: A multi-machine scaling of SOL widths with midplane poloidal magnetic field strength [90].

In addition to heat loads, reactor tokamaks will have particle load challenges. When high fluxes of plasmas are incident on material, a number of processes occur including reflection, desorption, sputtering, arcing, blistering, and evaporation [84]. One of the most problematic of these is physical sputtering of material atoms, which occurs when plasma particles impact material with sufficient energy to overcome the surface binding energy [84]. Because of the requirement of sufficient incident particle energy, sputtering yield increases significantly with temperature in divertor relevant regimes. Moreover, future reactors are set to operate at higher pressures,

which means the total flux of plasma incident on materials is set to increase. This sputtering can be a primary cause of material erosion for metal targets [91], which may reduce divertor lifetimes and increase machine cost. Moreover, if it enters the core, sputtered high-Z material such as tungsten can radiate a significant amount of core power, severely degrading confinement and limiting operational regimes [92], [93].

Already the challenge for steady-state heat and particle load management is a significant one. Exacerbating the challenge further are phenomena which can cause transient and spatially varied target loads. For example, operating in H-mode typically brings about edge-localised modes [94], which in ITER can cause peaking in heat loads from 1-10 GWm^{-2} [95]. Edge-localised modes can be mitigated through resonant magnetic perturbations, yet these can introduce a toroidal asymmetry and highly localised heat loads [96]. Finally, most reactor and reactor-like tokamaks will require fuelling via pellets, such that the fuel can efficiently penetrate the core. Pellet fuelling, however, unlike gas fuelling, is not continuous, and may cause temporal variation in plasma density, which can affect divertor power balance [97]. Consequently, finding methods to reduce heat and plasma fluxes in the divertor, and to ensure they do not spike, is vital for operation of future tokamaks.

1.3.3 Detachment

Though the heat flux challenge for reactor tokamaks is incredibly difficult, it is not without potential solutions. Of these solutions, most consist of operating under some form of dissipative divertor. In such scenarios, either the deuterium itself, or some external injected impurity such as nitrogen, argon, or neon, radiates a significant portion of the heat entering the SOL [98]. Though the radiated power is still deposited on surrounding material, this power is more isotropic and can lead to significant reductions in peak power loads [99].

Given sufficiently high power losses along the SOL, the plasma can effectively lose most of its power before it reaches the divertor targets. In this state, the hot, high power plasma effectively terminates at some point upstream of the divertor targets, leaving a cold (<5eV) region of partially ionised gas downstream of this point, known as the detached region [4], [99]. Because the high power plasma effectively detaches from the targets, this state is referred to as *detachment*. In between the high-power region, and the cold detached region, is a transition region of significant power loss and temperature gradients, often referred to as the detachment or radiation front. Figure 1.10 shows four different levels of detachment in TCV [100], where an increase in plasma density makes the carbon radiation front detach further and further from the targets.

Because of the significant fraction of radiated power, detachment leads to drastically reduced peak divertor heat loads. Furthermore, detachment is associated with a loss of plasma pressure due to volumetric atomic and molecular processes along

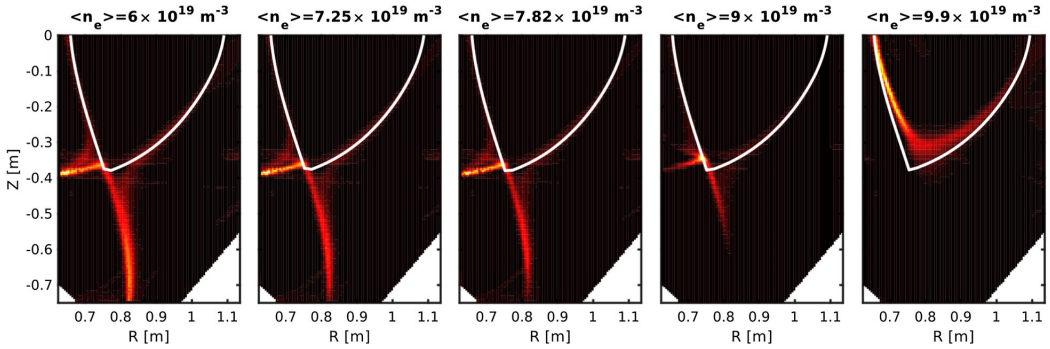

FIGURE 1.10: Tomographic inversions of carbon III radiation in the TCV tokamak. Adapted from [100].

the SOL [99], [101]. This reduction in pressure leads to a reduction in the plasma particle flux, as well as the heat flux [102]. Since detachment is one of the most effective ways of reducing particle and heat flux, it is one of the few ways reactor-tokamaks can operate without significant erosion of the divertor targets.

One final attractive aspect of detachment, is its potential to act as a shock absorber for transients [4]. In attached conditions, even small transient variations in plasma parameters can lead to significant spikes in target temperatures. In a deeply detached divertor however, as long as transient power variations do not reattach the divertor, the targets will always remain at a reasonable temperature.

1.3.4 Alternative Divertors

In addition to detachment, another key way in which reactor tokamaks may solve their heat flux challenges is through alternative divertor designs. These are divertor configurations which implement some sort of novel geometric or magnetic characteristics that differ from the standard single null divertor shown in Figure 1.8 [61]. Such features include:

- **A long connection length**, which allows for a larger temperature drop along the SOL in attached conditions, radiates more easily, and likely enhances radial transport.
- **A high total flux expansion** in the divertor volume, which spreads the instantaneous parallel heat flux density over a larger magnetic flux tube area.
- **Poloidal magnetic flux expansion** at the targets, which physically spreads power and particle loads over a larger physical area.
- **Multiple divertor targets**, to allow for sharing of heat loads between multiple surfaces.
- **Additional plasma x-points**, which may enhance cross-field transport and raise connection lengths.

- **Modified physical baffling**, which can potentially compress hydrogenic neutrals and impurities in the divertor region.

Over recent years several alternative divertor configuration designs have been proposed, some of which are shown in Figure 1.11. These alternative divertor designs include:

- The **Double Null**, which is a vertically symmetric divertor that shares power over four divertor targets.
- The **Snowflake** [103], which generates long connection lengths and power sharing between multiple targets through higher order x-points or multiple x-points near the primary x-point.
- **The X-divertor** [104], which increases connection lengths and reduces the poloidal magnetic field at the target by introducing an x-point inside the divertor targets.
- **The Super-X divertor (SXD)**, which leverages all the benefits of an X-divertor, but further increases connection lengths and introduces a total flux expansion by bringing the target strike point to a high major radius [105].
- **The X-point Target divertor** [106], which typically leverages the benefits of a Super-X, but with a secondary x-point in the plasma volume near the divertor targets. This leads to power sharing between the targets, and is thought to aid detachment control.
- **The Tightly Baffled, Long-Legged Divertor** [107], [108], which typically leverages a long physical divertor leg which is closely surrounding by physical baffling.

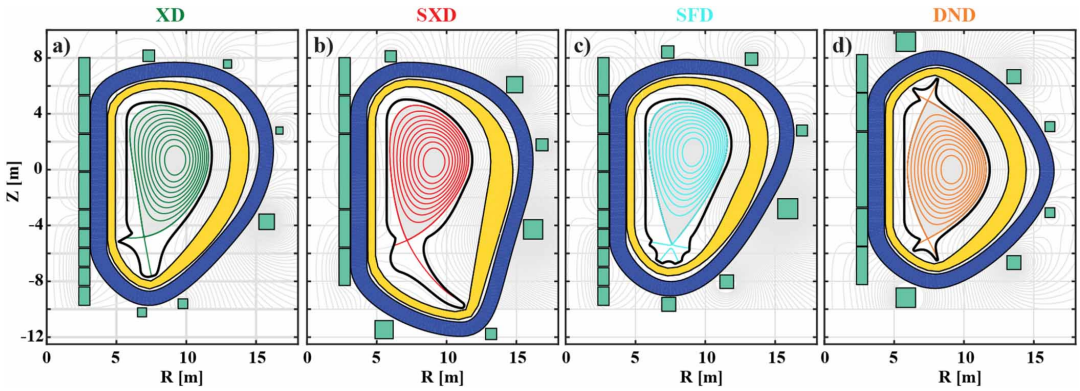

FIGURE 1.11: Poloidal diagrams for four potential alternative divertor configurations for the DEMO tokamak [109].

Currently the active field of alternative divertor research leverages theory, modelling, and experiment throughout the world. Machines such as MAST-U and TCV

have implemented and are performing experiments with alternative divertor geometries [110], [111]. The community is now building up an idea of which divertors work better than others. However, there is still work to be done in understanding *why* some configurations outperform others, and appreciating the isolated effects that individual features of divertors have on plasma exhaust. These effects could be on heat and particle fluxes, but also on detachment access and the transport of impurities. Furthering this understanding is what this thesis hopes to contribute to, primarily through modelling and simulation.

Because this work focuses on divertor features and design in general, its impacts may be useful even if alternative divertors are not explicitly used in future devices. *Because even in more conventional divertors, it is important to understand what divertor features can be changed, and what impact these modifications have on divertor performance.*

1.3.5 The MAST-U Tokamak

In the realm of alternative divertor study, an incredibly important experimental device is MAST-U. MAST-U is a spherical tokamak with a major radius 0.85 m and a minor radius of 0.65 m located at the Culham Centre for Fusion Energy in the UK. It has a maximum plasma current of 2 MA, and a maximum pulse length of 5s [112]. MAST-U is equipped with on and off-axis NBIs, which together can currently generate a maximum heating power 5 MW.

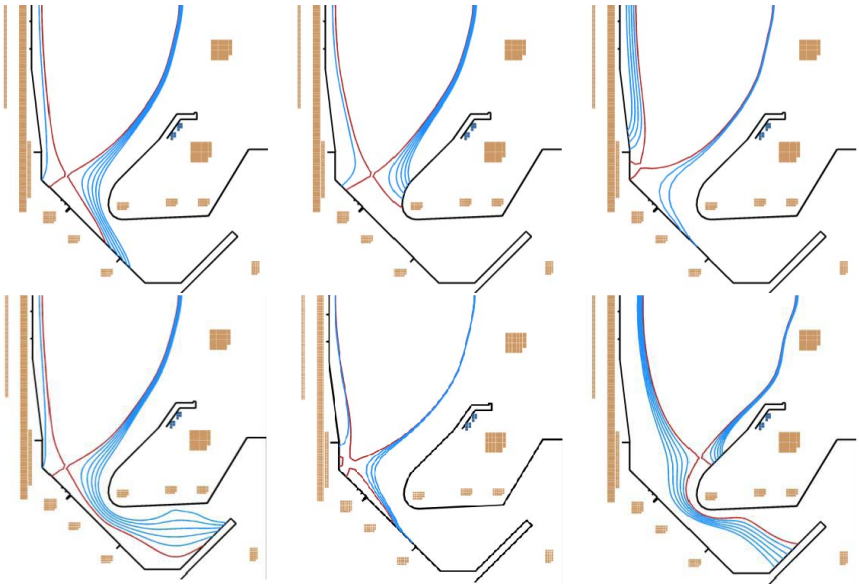

FIGURE 1.12: Examples of divertor configurations possible in MAST-U. Top row left to right: conventional, vertical target, and X-divertor. Bottom row left to right: Super-X, snowflake, and inner leg Super-X. Figure adapted from [71].

One of the key scientific motivations behind MAST-U is the study of alternative divertors. Because of this, each of the two approximately vertically symmetric divertors are surrounded by eight poloidal field coils which shape the magnetic configuration of the divertor [71]. This considerable set of poloidal shaping coils allows

MAST-U to operate with a number of alternative divertor configurations, including the X-divertor, Snowflake, x-point target, and Super-X. Several such configurations are shown in Figure 1.12.

Because MAST-U is one of the most well-equipped experimental tokamaks to study alternative divertors, it will be a focus of some work in this thesis. In particular, Chapter 4 features work simulating the Super-X divertor configuration in MAST-U, and Chapter 5 focuses on experimental data from MAST-U, comparing detachment control in the Super-X configuration with an Elongated Conventional Divertor (ECD).

1.4 Goals of This Work

The aim of the work contained within this thesis is to contribute to the understanding of how alternative divertor designs can influence the control of plasma exhaust. This work contributes to that understanding through developing and applying reduced models to advanced divertors and detachment, covered in Chapter 2. In addition, 2D SOLPS-ITER simulations of idealised geometries are used to verify predictions made by reduced models, which is covered in Chapter 3. Full geometry simulations of the MAST-U device are presented in Chapter 4, with a focus on studying the isolated effects of divertor baffling. Finally, comparison of reduced modelling to experimental results from the MAST-U tokamak is presented in Chapter 5.

Though the primary motivation of this work is for nuclear fusion, and the primary motivation for nuclear fusion is energy, this work may in fact have a myriad of other applications. Nuclear fusion, for example, as well as being a potential power source, could also be a source of neutrons for applications such as medicine [113]. Plasma physics as a subject has applications from medical plasmas [114], to plasma etching of semiconductors [115], to understanding astrophysics and space weather [116]. These applications should not be forgotten, as the aim of this thesis is to contribute - in however minor of a way - to the advancement of the broader field of plasma physics and fusion.

Chapter 2

Models for Alternative Divertors

Thus far, it should be apparent that there are many good motivations for studying divertor design and detachment physics in alternative divertors. In Chapter 1, some cursory ideas in divertor plasma exhaust have been introduced, along with key SOL plasma parameters such as λ_q. This chapter will delve much deeper into the physics governing the scrape-off layer, starting with more physically accurate models, and from those deriving simpler, more interpretable models. In particular, sections 2.4 and 2.5 contain original work on extensions made to analytical and 1D detachment modelling for alternative divertors. The theoretical groundwork laid in this chapter will be used in modelling and analysis for the remainder of this thesis. First, however, one of the most unique aspects of divertor modelling must be introduced: the target boundary.

2.1 Recycling and the Sheath

All of the physical models to be introduced in this chapter are comprised of two fundamental pillars: the governing equations which evolve a plasma solution in space and time, and the model domain and boundary conditions. Modelling parallel transport in the SOL, there are two main physical boundaries; the upstream at the core interface, and the downstream at the target, which henceforth will be denoted by subscript t. Boundary conditions at the core are typically inputs into models, which are determined by machine parameters such as fuelling rate. Conversely at the target, three important phenomena occur which act to impose boundary conditions: recycling, sheath acceleration, and sheath transmission.

Recycling is the process whereby charged particles incident on divertor targets return to the plasma as neutrals and are re-ionised, effectively self-fuelling the divertor plasma. Recycling can occur via recombination of incident plasma particles on the material surface, forming a weakly bound neutral molecules which are then desorbed back into the plasma [117]. However, fast reflection of ions as atoms can also significantly contribute to recycling [83]. Of course, plasma particles can also become embedded into the material, and not all of the particles incident on the targets will be recycled. Because of this, it is important to define a recycling fraction for a divertor target, R_{recyc}, which produces recycling flux [83]:

$$\Gamma_{recyc} = \Gamma_{i,t} R_{recyc}, \tag{2.1}$$

where Γ_{recyc} is the recycled neutral flux, and $\Gamma_{i,t}$ is the incident ion flux at the target, related to the target ion velocity $v_{i,t}$ via:

$$\Gamma_{i,t} = n_{i,t} v_{i,t}. \tag{2.2}$$

For a steady state reactor, the target material may become saturated and have a 100% recycling fraction. In such a case, though the incident and recycling fluxes are equal, it is important to keep in mind that the direction of the fluxes differ greatly. Since plasma particles travel along the direction of the magnetic field, the bulk plasma flux is in the parallel direction. Desorbed neutrals, however, are on average ejected perpendicular to the divertor targets.

The second important phenomena in modelling the target boundary is caused by the formation of the sheath, which is described as follows. At the boundary between the divertor targets and plasma, the target material acts as a sink for plasma particles. Due to the high mobility of electrons, the wall becomes negatively charged (if it is floating), and an ambipolar electric field forms, accelerating ions towards the wall [118]. As it turns out, solving for this potential results in some interesting consequences. Specifically, combining Poisson's equation with the Boltzmann relation and ion continuity results in a condition for non-oscillatory solutions. This condition, derived for cold ions ($T_i \approx 0$), places a limit on the ion flow velocity at the sheath entrance:

$$v_{i,t} \geq c_{st} = \sqrt{\frac{2eT_{i,t}}{m_i}}. \tag{2.3}$$

In other words, the ion velocity at the sheath entrance must equal or exceed the ion sound speed, c_{st}. This condition is known as the Bohm criterion [119], and implies that ions are accelerated even before they arrive at the sheath, in a region known as the pre-sheath. Although the Bohm criterion is derived for the sheath entrance, the sheath itself is typically very thin, meaning it contains negligible particle and heat sinks. As such, the heat and particle fluxes entering the sheath are equivalent to the target fluxes, and thus the Bohm criterion is often applied to target conditions, and the subscript t for target is used.

In addition to the Bohm criterion, one may attempt to solve for the plasma flow velocity in the sheath. In such a case, the solution for the isothermal plasma velocity forms a singularity for supersonic flow [83], [120]. As such, many enforce the condition that the plasma flow must be less then the sound speed. Combined with the Bohm criterion, this means the ion velocity must be equal to the sound speed at the sheath entrance:

$$v_{i,t} = \sqrt{\frac{2eT_{i,t}}{m_i}} \tag{2.4}$$

Though the plasma at the sheath is not quasi-neutral, the equation above is still a good approximation [83]. Note that this condition can be broken; in non-isothermal sheaths, but also in the presence of particular ion particle sinks [120]. Hence, Equation 2.4 is not to be taken as a general result, but can nevertheless be a useful one for modelling.

The final important interaction at the target is the transmission of heat into the material from the plasma. This target heat flux can be determined by considering the deposited power from Maxwellian distributions of electrons and ions impacting a material surface. This heat flux is typically given by the particle flux multiplied by the average energy of the impacting species. In the main plasma this energy is simply related to the Maxwellian temperature, but at the material surface the ions have been accelerated by the sheath potential, and slower electrons have been repelled from the material surface [83], [118]. To account for this sheath, a sheath transmission factor γ is introduced, which typically takes values between 7 and 8 [83]. With this transmission coefficient, the parallel heat flux at the target is:

$$q_{||,t} = \gamma e T_t \Gamma_t = \gamma n_t e T_t \sqrt{\frac{2eT_{i,t}}{m_i}}. \tag{2.5}$$

These three phenomena of recycling, sheath acceleration, and sheath transmission, are crucial to building simple models for divertors. Even for complex computational models, they help to form a set of boundary conditions enforced on the computational domain.

2.2 Computational Models

2.2.1 Edge Fluid Codes

Now that the boundaries of a divertor plasma have been introduced, the equations governing the plasma evolution may be considered. In general, when there are a range of collisionalities present, or when collision length scales are similar to the characteristic length scale of the problem, particles should be treated kinetically [121]. In this formulation, the distribution functions of particles (distributed across spatial and velocity dimensions) are evolved via kinetic equations. Indeed, kinetic codes have a range of applications in fusion plasma physics, from gyrokinetic modelling of turbulence [122]–[124], to particle in cell modelling of laser plasma interactions [125]. A particular application of kinetics to edge physics is in modelling the transport of neutral atoms or molecules, which have a range of collisionalities in tokamaks.

Though the kinetic treatment of plasmas is generally accurate, kinetic codes are often difficult to formulate and computationally expensive. When collisionalities are sufficiently high, however, plasmas can be treated as fluids. The fluid approach evolves bulk quantities of a plasma, such as density and temperature, and is a much less computationally expensive formulation than kinetics. The fluid equations for a collisional plasma can be derived by finding the moments from the governing kinetic equations. Taking the first order moment, by simply integrating the kinetic equation over velocity space, and noting that collision operators conserve particles, gives the continuity equation [51], [126]:

$$\frac{\partial n_s}{\partial t} + \nabla \cdot (n_s \mathbf{v}_s) = S_s, \tag{2.6}$$

where:

- $\frac{\partial n_s}{\partial t}$ is the time evolution of particle density.
- $\nabla \cdot (n_s \mathbf{v}_s)$ is the divergence of particle flux.
- S_s is any additional particle source or sink (from ionisation, for example).

By integrating the kinetic equation multiplied by $\mathbf{v}_s m_s$, the second order moment can be obtained, which describes the conservation of momentum[51], [126]:

$$m_S n_s \frac{\partial \mathbf{v}_s}{\partial t} + \nabla p_s + \nabla \cdot \Pi_s + Z_s e n_s (\mathbf{E} + \mathbf{v}_s \times \mathbf{B}) = \mathbf{F}_{s,col}, \tag{2.7}$$

where:

- $mn \frac{\partial \mathbf{v}_s}{\partial t}$ is the acceleration of the fluid.
- ∇p_s is the force created by the gradient of the thermal pressure p_s.
- $\nabla \cdot \Pi_s$ is the force created by viscous stress in the fluid, calculated from viscosity tensor Π_s.
- $Z_s e n_s (\mathbf{E} + \mathbf{v} \times \mathbf{B})$ is the electromagnetic force on species s, with effective atomic number Z_s.
- $\mathbf{F}_{s,col}$ is the force on species s due to collisions with other species.

Finally, by integrating the kinetic equation multiplied by $\frac{1}{2} m_s \mathrm{v}_s^2$, the third order moment can be obtained. The resulting equation is the fluid conservation law for energy [51], [126]:

$$\frac{3}{2}\frac{\partial p_s}{\partial t} + \frac{5}{2} p_s \nabla \cdot \mathbf{v}_s + \nabla (\Pi_s \cdot \mathbf{v}_s) + \nabla \cdot \mathbf{q}_s = W_s, \tag{2.8}$$

where:

- $\frac{3}{2}\frac{\partial P}{\partial t}$ is the time varying pressure (internal energy) of the fluid.

- $\frac{5}{2} p_s \nabla \cdot \mathbf{v}_s$ is the rate of work done on the fluid due to thermal pressure.
- $\nabla(\Pi_s \cdot \mathbf{v}_s)$ is the rate of work done on the fluid due to viscous stresses.
- $\nabla \cdot \mathbf{q}_s$ is the divergence of the species heat flux density.
- W_s is the rate of energy transfer to species s from collisions and radiation.

Equations 2.6, 2.7, and 2.8 form the Braginskii fluid equations for a plasma species s, which could be electrons, ions, or neutrals [127], [128]. A set of three coupled Braginskii equations for electrons, ions, and neutrals can be used to evolve species densities, temperatures, and fluxes, across a computational grid using a computational fluid dynamics code. However, the Braginskii equations by themselves do not form a complete model for a divertor plasma. To this end, one must introduce a closure scheme, which allows unknown quantities such as Π_s and $\mathbf{q}_s$ to be expressed in terms of known plasma quantities such as n_s and T_s.

The standard scheme for the Braginskii equations is the Chapman–Enskog closure scheme [129], which yields expressions for unknown quantities in terms of transport coefficients, such as conductivity and diffusivity. This is performed by expanding the kinetic distribution function in terms of a Maxwellian background and higher order corrections. Solving for the first order correction, the resultant heat flux obeys the law of heat conduction:

$$\mathbf{q}_s = -\kappa_s \nabla T_s, \tag{2.9}$$

where κ_s is the species thermal conductivity.

It is important to note however, that this closure scheme is only valid when the species distribution can be approximated as a Maxwellian with a first order correction. This is only true when particles are sufficiently collisional, such that the mean free path is much shorter than the system scale length, and expansions higher than first order can be neglected.

Closure schemes are vital for self-consistently modelling plasmas as fluids. However, the resultant viscosity and heat fluxes produced by the Chapman–Enskog closure scheme depend upon transport coefficients, such as thermal conductivity. If these transport coefficients were purely diffusive, they could be computed fairly easily from plasma parameters. However, much of transport in the SOL (and particularly radial transport in the SOL) is non-diffusive or anomalous, and emerges from phenomena such as turbulence. This is an important point, and is one of the largest sources of uncertainty in non-turbulent simulation codes for the edge. And as a consequence, fluid simulations using this closure scheme can never be fully predictive.

2.2.2 SOLPS-ITER

From the accurate yet abstract governing equations of scrape-off layer plasmas, computational models can be built to solve such equations and determine plasma solutions. Of these, one of the most widely used simulation architectures is SOLPS-ITER (Scrape Off Layer Plasma Simulator - ITER) [1], [2]. This code is a combination of B2.5, a fluid simulator solving the multi-species Braginskii equations [126], and EIRENE, a kinetic Monte Carlo solver applied to the Boltzmann equations for neutral atoms and molecules [130]. The B2.5 simulation domain is a 2D grid in the poloidal plane with assumed toroidal symmetry. The geometry of the 2D grid is aligned to the magnetic flux surfaces as shown in Figure 2.1. As a result, the standard coordinates for SOLPS-ITER are the poloidal (along magnetic flux surfaces) direction x, and the radial direction y (perpendicular to flux surfaces in the poloidal plane).

Though B2.5 and EIRENE are the two primary physics modules of SOLPS-ITER, in reality the code is a combination of the following submodules:

- B2.5, the fluid solver for the plasma species [3], [126].
- Eirene, the kinetic Monte Carlo solver for the neutrals [3], [130], [131].
- Divgeo, a graphical user interface that allows users to build the basic input structure of the simulation, such as the machine walls and targets.
- CARRE, a grid builder, required to create the plasma simulation grid domain.
- ADAS, the modules containing relevant atomic and molecular rate data, such as ionisation and recombination cross-sections.

SOLPS-ITER is the primary simulation tool leveraged in this thesis. When running SOLPS-ITER simulations, there are several important inputs to consider. First, there is the plasma domain itself, which is generated from equilibria from a real tokamak, or artificially generated. Then the surrounding wall material must be specified, including recycling and pumping coefficients and whether sputtering and tracking of wall material is active.

Finally, one must consider the boundary conditions of the plasma grid itself. The plasma boundaries in SOLPS-ITER fall into three categories:

- **The upstream boundary**, which corresponds to the core boundary for a full geometry simulation, or the x-point for an isolated leg simulation. In terms of energy, the most common boundary conditions for the upstream are a fixed flux of power, equally spread over the entire boundary, or a fixed flux density for each cell. In terms of particles, a fixed density, or fixed flux boundary condition are the two most common conditions applied. These boundary conditions are meant to model the sources of fuelling and heating in the core.

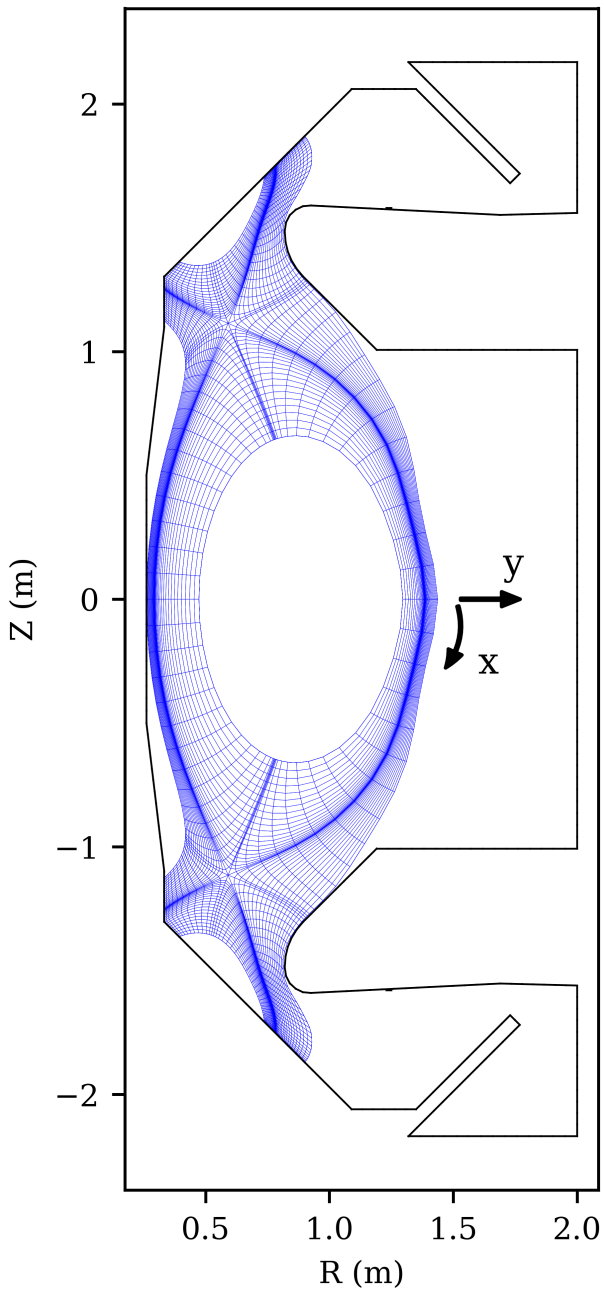

FIGURE 2.1: The poloidal B2.5 grid for a MAST-U double null divertor. The SOLPS-ITER poloidal (x) and radial (y) coordinate directions are indicated at the midplane.

- **The downstream boundary**, which corresponds to the divertor targets. At the targets, the sheath boundary conditions are applied for particle and heat fluxes. Incident ions are re-injected into the plasma - calculated through the specified target recycling coefficients. Recycled neutrals are launched through EIRENE with a distribution centred around 90°to the target surface.

- **The radial boundaries**, at the SOL and PFR edges of the plasma. At these boundaries a decay length is specified for the electron and ion temperatures. In terms of particles, either a density decay length or leakage factor are specified. An important aspect of these boundaries to keep in mind is that any plasma leaving radially from the grid is re-injected into the plasma as neutrals (at the ion temperature). This is meant to approximate main chamber recycling, but will inevitably fail to capture the real effects of having a plasma fully extend to the first wall.

It is important to remember that there are many scrape off layer plasma simulators, such as UEDGE [132], EMC3-EIRENE [133], SOLEDGE2D [134], and SOLPS-ITER. For this thesis, however, SOLPS-ITER will be the main simulation architecture used. The reason for this is that SOLPS-ITER is one of the most widely used in the boundary modelling community, and has good coupling between the fluid and kinetic species [1]–[3]. Simulations using SOLPS-ITER are presented in Chapters 3 and 4.

2.3 The Two-Point Model and Divertor Regimes

When it comes to high fidelity, accurate predictions of the divertor, fluid and kinetic simulations can be powerful tools. However, these tools can be expensive, and from the governing equations alone very little intuition can be drawn as to how divertor targets may fair in different conditions. For this reason, divertor physics also leverages reduced models, which allow for more rapid, heuristic understanding of divertor regimes and geometries. Among these, the most frequently used is the two-point model [83].

Fundamentally, the two-point model deals with energy and momentum balances similar to the Braginskii equations. However, the two-point model deals with this balance only in a single flux tube, which is defined as an elementary volume bounded by two magnetic flux surfaces, and which contains a constant value of magnetic flux along the tube [83]. The model also only considers transport in the direction parallel to the magnetic field. Because of this, the heat flux is only considered in the parallel direction.

As the name suggests, the balance of the two-point model is considered between two points. The first of these two points, shown in Figure 2.2, is the 'upstream' point, typically located at the outer midplane, and denoted by subscript u. The second of these is the downstream point located at the target, and denoted by subscript t. Since

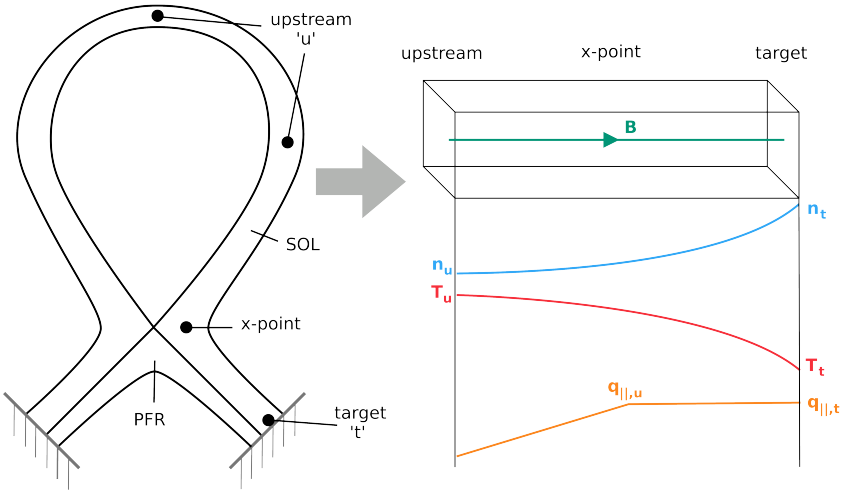

FIGURE 2.2: The basis of the two-point model.

this is a reduced model, some assumptions must be made. One critical assumption is that the heat flux upstream of the sheath is all electron conducted, such that:

$$q_{||} = q_{||,cond} = \kappa_{e,0} T^{5/2} \frac{dT}{ds}. \tag{2.10}$$

Here $\kappa_{e,0}$ is the Spitzer electron conductivity divided by $T^{5/2}$, which is typically constant for a constant ion charge state Z. Consider first the heat balance in a divertor which has no significant power losses. In such a case, the parallel heat flux density will simply scale with the parallel area of the flux tube, which decreases with total magnetic field B:

$$q_{||}(s) = q_{||,u} \frac{B}{B_u}, \tag{2.11}$$

where $q_{||,u}$ is the upstream heat flux entering the divertor, fed from radial transport from the core. From this equation one can relate the upstream and target heat fluxes via:

$$q_{||,u} = \frac{B_u}{B_t} q_{||,t} = F_R q_{||,t} \tag{2.12}$$

Here a new term known as the total flux expansion of the divertor has been introduced, $F_R = \frac{B_u}{B_t}$, a measure of the expansion of the parallel flux tube area from upstream to downstream [135]. This expansion can be a very useful geometric feature to optimize in divertors, since for a given input power, the target parallel heat flux density decreases with high total flux expansion. Now at the targets, the heat flux density must satisfy sheath transmission:

$$q_{||,t} = \gamma e n_t T_t \sqrt{\frac{2eT_t}{m_i}}. \tag{2.13}$$

Thus the upstream heat flux and target conditions are related through:

$$q_{||,u} = F_R \gamma e n_t T_t \sqrt{\frac{2eT_t}{m_i}}. \tag{2.14}$$

Second, consider the impact on temperature this conducted heat flux will have. Given the definition of conducted heat flux in Equation 2.10, the upstream and target temperatures are related through

$$T_u^{7/2} = T_t^{7/2} + \frac{7}{2\kappa_{e0}} \int_t^u q_{||} ds. \tag{2.15}$$

Then, assuming the magnetic field profile varies roughly linearly between upstream and target, this can be simplified to

$$T_u^{7/2} = T_t^{7/2} + \frac{7}{2} \frac{q_{||,u} L_{||}}{\kappa_{e0}} \left[\frac{\ln(F_R)}{F_R - 1} \right]. \tag{2.16}$$

Finally, consider the balance of pressure from upstream to downstream. Assuming no loss of total pressure along the SOL, $p_u = p_t$. Upstream, we expect the flow velocity to be low, and hence the total upstream pressure p_u should be dominated by static pressure $p_u = 2n_u T_u$. At the target, however, the accelerated ions have a high velocity, and hence the downstream pressure is a combination of static and dynamic pressure,

$$p_t = 2n_t T_t + n m_i c_s^2 = 4 n_t T_t. \tag{2.17}$$

Thus, equating the upstream and downstream pressures gives the relation:

$$2 n_t T_t = n_u T_u. \tag{2.18}$$

In other words, the Bohm criterion means without pressure loss, the static pressure at the target is half of the upstream static pressure. Equations 2.14 , 2.16, and 2.18 form the basis of the two-point model [83]. Given an upstream density and heat flux, the upstream temperature, and target density and temperatures can be computed. Thus, this model can be a very powerful tool to study the relationship between upstream and target, and how this relationship varies with regime and divertor configuration. The two point model equations can be interrogated and modified to study different divertor regimes, which will be done over the following sections.

2.3.1 The Sheath Limited Regime

First consider a regime where temperatures in the SOL are sufficiently high, such that the temperature gradient from conduction is negligible compared to the upstream temperature. To put this mathematically, $T_u^{7/2} \gg \frac{7}{2} \frac{q_{||,u} L}{\kappa_{e0}} \left[\frac{\ln(F_R)}{F_R - 1} \right]$. In such a case, the SOL is effectively isothermal, $T_u \approx T_t$.

How then is this isothermal temperature set in the context of the two point model? Using Equation 2.14 for sheath transmission, and substituting $T_u \approx T_t$ gives:

$$T_u^{1/2} \approx \frac{2q_{||,u}}{F_R \gamma e p_t} \sqrt{\frac{m_i}{2e}}. \tag{2.19}$$

Then, noting the relationship between upstream and downstream pressure in 2.18, this equation can be expressed:

$$T_u^{3/2} \approx \frac{2q_{||,u}}{F_R \gamma e n_u} \sqrt{\frac{m_i}{2e}}, \tag{2.20}$$

or

$$T_u \propto \frac{q_{||,u}^{2/3}}{n_u^{2/3}}. \tag{2.21}$$

Thus, in this high temperature regime, the upstream (and downstream) SOL temperature is simply proportional to the ratio of upstream heat flux to density to the power 3/2. Quite intuitively, this means operating with lower densities or higher input powers should lead to higher temperatures in the SOL. Because this SOL temperature is determined by the heat flux boundary for sheath transmission, this regime is termed the sheath-limited regime. Additionally, though it is trivial, the target density can be found using pressure conservation and $T_u \approx T_t$. The result is:

$$n_t = \frac{n_u}{2}. \tag{2.22}$$

Consequently, for the sheath-limited regime, the target density is entirely determined by the upstream density (though not exactly equal due to the presence of dynamic pressure at the sheath). When considering the sheath-limited regime, remember that the equations of the two-point model rely on the assumption of equal electron and ion temperatures. However, the sheath-limited regime by definition is high temperature, and not very collisional, meaning there is no reason to assume electron and ion temperatures will equilibrate.

2.3.2 The Conduction Limited Regime

Now consider the characteristics of the SOL if the upstream temperature is significantly reduced past the sheath-limited regime. The $T^{5/2}$ term in Equation 2.10 indicates that with a constant heat flux, lower temperatures will lead to higher temperature gradients along the SOL. As such, if temperatures are reduced past the sheath limited regime, conduction can begin to drive a significant temperature drop. In fact, this drop can be significantly larger than the target temperature, $T_t^{7/2} \ll \frac{7}{2}\frac{q_{||,u}L}{\kappa_{e0}}\left[\frac{\ln(F_R)}{F_R - 1}\right]$. In such a case, the upstream temperature is entirely determined by the conduction-driven temperature difference:

$$T_u \simeq \left(\frac{7}{2}\frac{q_{||,u}L_{||}}{k_0}\right)^{2/7}\left[\frac{\ln(F_R)}{F_R-1}\right]^{2/7}. \tag{2.23}$$

Unsurprisingly, this regime of conduction determining upstream temperatures is known as the conduction-limited regime. Inspecting Equation 2.18 for pressure conservation, note that by driving low target temperatures, the conduction-limited regime also results in high target densities. According to Equation 2.2, higher densities at a constant pressure leads to higher particle fluxes. These high particle fluxes are characteristic of the conduction-limited regime, and the recycled fluxes can therefore be an important source of particles in the divertor. As a result, the conduction-limited regime is also known as the high-recycling regime.

From 2.23 there are already a few apparent consequences for the conduction-limited regime. In particular, this equation shows the upstream temperature - an extremely important parameter for the pedestal - is impacted by divertor geometry in several ways. First, obtaining a higher upstream temperature can be achieved through a long divertor leg with a high $L_{||}$. Additionally, T_u can be raised by lowering the total flux expansion of the divertor. Both of these effects, however, are weak, and the effect of flux expansion is particularly so.

In addition to upstream temperatures, the conduction-limited two-point model can be used to study how target temperature can be reduced through divertor design. Combining equations 2.14 and 2.18 yields

$$T_t = \frac{m_i}{2e}\frac{4q_{||,u}^2}{F_R^2\gamma^2e^2n_u^2}\left(\frac{7}{2}\frac{q_{||,u}L_{||}}{k_0}\right)^{-4/7}\left[\frac{\ln(F_R)}{F_R-1}\right]^{-4/7}, \tag{2.24}$$

or:

$$T_t \propto q_{||,u}^{10/7}n_u^2L_{||}^{-4/7}F_R^{-2}. \tag{2.25}$$

Equation 2.25 indicates that longer connection lengths can be used to reduce target temperatures, in addition to increasing upstream temperatures. Moreover, since the F_R^{-2} term dominates over other flux expansion terms in Equation 2.24, an increase in total flux expansion can be a powerful way to reduce target temperatures.

Finally, the two-point model may be used to determine how target particle flux varies with divertor configuration in the conduction-limited regime. In particular, the target density can be determined by combining equations 2.14 and 2.18, resulting in:

$$n_t = \frac{n_u^3F_R^2}{q_{||,u}^2}\left(\frac{7}{2}\frac{q_{||,u}L_{||}}{k_0}\right)^{4/7}\frac{\gamma e^2}{2m_i}\left[\frac{\ln(F_R)}{F_R-1}\right]^{6/7}. \tag{2.26}$$

Combining this with Equation 2.2 Equation 2.24 leads to the relation:

$$\Gamma_{i,t} \propto n_u^2q_{||,u}^{-3/7}L_{||}^{2/7}F_R \tag{2.27}$$

From this equation, we see that many tools which can be used to reduce target temperatures, also increase target densities. This is unsurprising, given that total pressure must remain constant, but leads to the result that low target temperatures may exacerbate the issue of particle erosion. However, particle sputtering, though proportional to target flux, is also proportional to the sputtering rate. This rate has a strong dependence on temperature, and often, even if raw particle fluxes increase through a reduction in temperature, the lowering of the sputtering rate is typically sufficient to *lower* the overall erosion rates [83]. Particle fluxes can be reduced, however, even at low temperatures, by accessing strongly radiating regimes and detached regimes.

2.3.3 The Strongly Radiating and Detached Regimes

If temperatures are reduced past the conduction-limited regime, access to low target temperatures can catalyse a plethora of atomic and molecular processes in the divertor. These processes such as ionisation, radiation (from hydrogen or some injected impurity), and charge exchange, can act as significant sinks of power and momentum. This regime of strong power and pressure sinks is known as the strongly radiating regime [99].

Clearly, such a regime breaks the assumptions of the simple two-point model in that neither pressure nor power are conserved from upstream to target. However, one can assume most of these losses occur in a small region near the target, and introduce fractional loss terms of momentum and heat. These factors of f_{mom} and f_{rad} are defined by [101]:

$$2n_t T_t = (1 - f_{mom}) n_u T_u \tag{2.28}$$

$$q_{||,t} = \gamma n_t k T_t c_{st} = (1 - f_{power}) \frac{q_{||,u}}{F_R} \tag{2.29}$$

These equations, combined with the usual expression for upstream temperature, form the extended two-point model. Using these equations to formulate expressions for target temperature and density results in:

$$T_t = \frac{m_i}{2e} \frac{4q_{||,u}^2}{F_R^2 \gamma^2 e^2 n_u^2} \left(\frac{7}{2} \frac{q_{||,u} L_{||}}{k_0} \right)^{-4/7} \left[\frac{\ln(F_R)}{F_R - 1} \right]^{-4/7} \frac{(1 - f_{power})^2}{(1 - f_{mom})^2}. \tag{2.30}$$

and

$$n_t = \frac{n_u^3 F_R^2}{q_{||,u}^2} \left(\frac{7}{2} \frac{q_{||,u} L_{||}}{k_0} \right)^{4/7} \frac{\gamma e^2}{2 m_i} \left[\frac{\ln(F_R)}{F_R - 1} \right]^{6/7} \frac{(1 - f_{mom})^3}{(1 - f_{power})^2}, \tag{2.31}$$

From these equations it is clear to see how important these momentum and power losses are in determining target conditions. As the power loss along the SOL increases, the target temperature and heat flux will decrease, which will lead to more

gentle heat loading at the target. However, power losses alone may not solve all the exhaust challenges of a divertor, since target density increases with $(1 - f_{power})^{-2}$, and thus the particle flux will increase with a higher f_{power}. Combining the two equations above, it is clear that $\Gamma_t \propto \frac{(1-f_{mom})^2}{(1-f_{power})}$. Thus, momentum loss is a crucial method of reducing particle fluxes at the target.

This modified two-point model can be used to study and understand the strongly radiating regime, and the detached regime. Detachment can reach temperatures in the sub-eV range, and is also associated with significant pressure loss, such that in the detached regime the total particle flux at the target begins to *decrease* with decreasing temperature. In fact, the point at which the particle fluxes change from increasing to decreasing with temperature is known as the rollover point, and is commonly associated with the threshold of detachment [99], [101]. This is by no means the only definition, as definitions such as a low (5 eV) peak target temperature are also used to define the detachment threshold.

One interesting output of the two-point model is that it can be used to determine the upstream density required to achieve a specific target temperature, and hence, to access detachment. This can be done by combining equations 2.28 and 2.29 to result in:

$$\frac{1}{2}\gamma k c_{st}(1 - f_{mom}) n_u T_u = q_{||,u}(1 - f_{power}) F_R^{-1}. \tag{2.32}$$

Rearranging for upstream density, this gives:

$$n_u = F_R^{-1}\left[2\frac{q_{||,u}}{\gamma k c_{st} T_u}\frac{(1 - f_{power})}{(1 - f_{mom})}\right]. \tag{2.33}$$

Given a constant upstream heat flux density, and constant power and momentum losses, a given target temperature means everything but T_u and F_R on the right hand side of Equation 2.33 will remain constant. Now with a constant upstream heat flux, connection length, and target temperature, T_u is weakly dependent only on total flux expansion. Here this effect is neglected, and a roughly constant T_u is assumed. In this case Equation 2.33 can be expressed:

$$n_u \propto F_R^{-1} = \frac{B_t}{B_X}. \tag{2.34}$$

This is an important result, as it shows the density required for a given low target temperature scales with the inverse of total flux expansion. In other words, this equation predicts that the density required for detachment access should be lower for divertors with high total flux expansions. As a result, configurations such as the Super-X divertor which leverage high total flux expansions should have easier detachment access.

Though this is a powerful prediction, it is also a severely limited one. In particular, inherent to this scaling is the assumption that power and momentum losses (or at least the ratio of the two) remain constant across different divertors with the

same target temperature. There is no basis for this assumption, and in fact the use of power and momentum loss specified as inputs of this model is a severe limitation to generally applying the two-point model to the detached regime. Detachment - at its core - is characterised by power and momentum losses, and the two-point model on its own can predict nothing when it comes to these losses. Thus, any application of the two-point model to the detached regime must be considered with a healthy dose of caution.

Another limitation of the two-point model is its inability to effectively describe deeply detached divertors, which may be desired in future reactors to prevent reattachment. This is because, to derive the extended two-point model equations, it was assumed that all the power and momentum loss occurs near the divertor targets. One alternative model, known as the Detachment Location Sensitivity model, can be a useful tool to self-consistently study such deeply detached states.

2.4 The DLS Model

One of the most vital ways in which alternative divertors influence plasma exhaust is through the process of detachment. As such, a simple way of understanding how divertor features can influence access to and control over detachment would be of great utility for divertor design. Here the Detachment Location Sensitivity (DLS) model is introduced; a model that predicts how detachment is accessed and evolves in a given divertor when key plasma parameters are varied. This model uses previous work on thermal fronts and detachment location sensitivity [4], [136]. In this thesis, extensions are made to the model, including formulating the model with an arbitrary magnetic field profile, and allowing calculations of self-consistent heat and temperature profiles.

2.4.1 The Simple DLS Model

At the centre of the DLS model is the idea of the thermal front. A detached thermal front is defined as the region of strong temperature gradients, transitioning from a hot conduction-dominated plasma to the cold convection-dominated detached region [136]. This thermal front typically coincides with regions of steep power loss from radiation, which are often referred to as radiation fronts. Fundamentally, the DLS model deals with the location of the cold end of these fronts, where the heat flux and temperature are effectively reduced to 0, as shown in Figure 2.3. This location is an important measurable quantity related to the degree of detachment, and this location will henceforth be referred to as the detachment front or location of detachment.

The DLS model can be derived by first considering heat balance between the location of a detachment front and upstream. Assuming all heat flux is dissipated entirely by radiation from some injected or intrinsic impurity species α, we can write

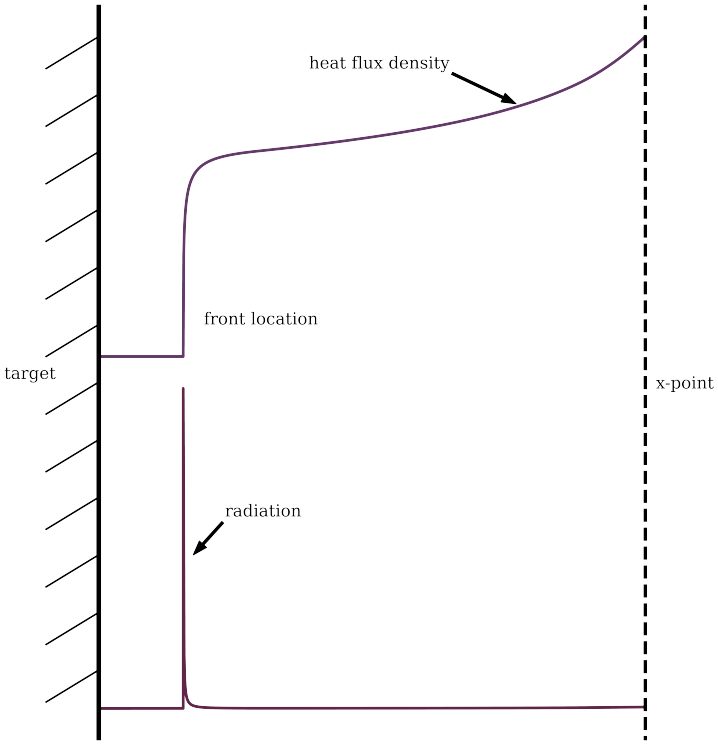

FIGURE 2.3: A conceptual diagram showing the fundamental basis of the DLS model.

the volumetric impurity radiation W_α in terms of an impurity fraction $f_\alpha = \frac{n_\alpha}{n}$, where n_α is the total ion density of impurity α, summed over all charge states. The impurity radiation is then given by the product of this impurity fraction, n^2, and the electron cooling function of the impurity $L_\alpha(T) = \frac{W_\alpha}{n n_\alpha}$ [137]. This function is also called the radiative loss parameter and can be computed for a given impurity at coronal equilibrium. In the divertor, however, impurities are generally not at coronal equilibrium, as the average time a given impurity spends in the divertor before being transported away can be as short as ionisation and recombination times [98]. This so-called residence time τ_α, leads to non-coronal effects, and the cooling curve for short residence times can be calculated using collisional radiative models.

Using this formulation for impurity radiation, heat balance along a flux tube can be written:

$$B\frac{d}{ds}\left(\frac{q_{||}}{B}\right) = n^2 f_\alpha L_\alpha(T). \tag{2.35}$$

By multiplying the equation by $\frac{2q_{||}}{B^2}$, and using the chain rule, Equation 2.35 can be written:

$$\frac{d}{ds}\left(\frac{q_{||}^2}{B^2}\right) = 2\frac{q_{||}}{B}\frac{d}{ds}\left(\frac{q_{||}}{B}\right) = \frac{2q_{||}n^2 f_\alpha L_\alpha(T)}{B^2}. \tag{2.36}$$

This may be integrated from the x-point, denoted by subscript X, to the leading edge of the detachment front, denoted by subscript f:

$$\frac{q_{||,X}^2}{B_X^2} - \frac{q_{||,f}^2}{B_f^2} = \int_{s=0}^{s=s_X} \frac{2q_{||}n^2 f_\alpha L_\alpha(T)}{B^2} ds. \tag{2.37}$$

In the context of this simple model, the detachment front is the region where all of the heat flux is dissipated by impurity radiation, and as a result the heat flux at the downstream end of this front disappears. Hence:

$$\frac{q_{||,X}^2}{B_u^2} = \int_{s_{f,||}}^{s_X} \frac{2q_{||}n^2 f_\alpha L_\alpha(T)}{B^2} ds. \tag{2.38}$$

Next, the front is assumed to be sufficiently narrow compared to the size of the divertor, as is the case in Figure 2.3. Under this assumption, the impurity fraction and magnetic field should not vary significantly within this front, and they can be taken out of the integral as their average values at the front location:

$$\frac{q_{||,X}^2}{B_u^2} = \frac{f_\alpha}{B_f^2} \int_{s_{f,||}}^{s_X} 2q_{||}n^2 L_\alpha(T) ds. \tag{2.39}$$

Here, it is also assumed that the electron static pressure above the downstream end of the front remains constant, such that density can be expressed: $n = \frac{n_u T_u}{T}$. The resulting equation is:

$$\frac{q_{||,X}^2}{B_u^2} = \frac{f_\alpha n_u^2 T_u^2}{B_f^2} \int_{s_{f,||}}^{s_X} 2q_{||}T^{-2} L_\alpha(T) ds. \tag{2.40}$$

Then, the heat flux is assumed to be entirely electron conducted, such that $q_{||}$ can be replaced with $\kappa_{e0}T^{5/2}\frac{dT}{ds}$:

$$\frac{q_{||,X}^2}{B_u^2} = \frac{f_\alpha n_u^2 T_u^2}{B_f^2} \int_{T_f}^{T_u} 2\kappa_{e0}T^{1/2} L_\alpha(T) dT, \tag{2.41}$$

or:

$$\frac{q_{||,X}}{B_u} = \sqrt{f_\alpha}\frac{n_u T_u}{B_f} \sqrt{\int_{T_f}^{T_u} 2\kappa_{e0}T^{1/2} L_\alpha(T) dT}. \tag{2.42}$$

Finally, the upstream temperature can be expressed as an integral of heat flux above the front, using the definition of electron conducted heat flux from Equation 2.10. Because it was assumed that all heat flux is dissipated in a thin region at the front, then for the majority of the integral above, the heat flux varies only due to magnetic flux expansion. Now, however, the derivation arrives at a junction; the upstream temperature and heat flux profile above the front depend on what point is chosen for the upstream. There are two options here:

- Define the upstream temperature and density to be at the midplane, and model the heat flux to be fed by some constant source from the midplane to the x-point.
- Define the upstream temperature and density to be at the x-point, and model the heat flux to originate at the x-point.

Consider the latter case first. In this case, the heat flux above the front is $q_{||} = q_{||,X}\frac{B}{B_X}$. Integrating this conducted heat flux, and noting that $T_f^{7/2} \ll T_u^{7/2}$ gives:

$$T_u = \left(\frac{7}{2\kappa_{e0}}\frac{q_{||,X}}{B_X}\int_{s_{f,||}}^{s_X} B ds\right)^{2/7}. \tag{2.43}$$

Substituting this definition of upstream temperature into Equation 2.42 results in

$$\frac{q_{||,X}}{B_u} = \sqrt{f_\alpha}\frac{n_u}{B_f}\left(\frac{7}{2\kappa_{e0}}\frac{q_{||,X}}{B_X}\int_{s_{f,||}}^{s_X} B ds\right)^{2/7}\sqrt{\int_{T_f}^{T_u} 2\kappa_{e0}T^{1/2}L_\alpha(T)dT}, \tag{2.44}$$

or

$$\frac{n_u\sqrt{f_\alpha}}{q_{||,X}^{5/7}} = \frac{B_f}{B_X}\left(\frac{1}{B_X}\int_{s_{f,||}}^{s_X} B ds\right)^{-2/7} 7^{-2/7}(2\kappa_{e0})^{-3/14}\left(\int_{T_f}^{T_u} T^{1/2}L_\alpha(T)dT\right)^{-1/2}. \tag{2.45}$$

The above equation gives us a very powerful relationship between parameters controlling detachment - parameters such as the divertor impurity fraction or upstream density - with the location of a detachment front in a given geometry. To make this relationship more clear, a lumped detachment control parameter C can be introduced,

$$C = \frac{n_u\sqrt{f_\alpha}}{q_{||,X}^{5/7}}. \tag{2.46}$$

Here C takes into account the variation of the three parameters one may use to access and control detachment: plasma fuelling (n_u), impurity seeding (f_α), and power variation ($q_{||,X}$).

To express Equation 2.45 more clearly, three terms can be introduced on the right hand side of the equation. First, one can incorporate the parameter C_0,

$$C_0 = 7^{-2/7}(2\kappa_{e0})^{-3/14}\left(\int_{T_f}^{T_u} T^{1/2}L_\alpha(T)dT\right)^{-1/2}. \tag{2.47}$$

This parameter depends on the impurity electron cooling function, and (in this simple version of the model) remains constant with a sufficiently high T_u and low T_f

(out of the effective range of $L_\alpha(T)$), such that the radiation is not affected by variations in these limits. However, a constant C_0 also assumes a constant κ_{e0} across the divertor, which is not true in regions of sufficiently high collisionality [120].

Secondly, the term $L_{||,f} = s_X - s_{f,||}$ can be introduced; the parallel connection length between the detachment front and upstream (x-point). Finally, the line-averaged magnetic field upstream of the front can be introduced, given by:

$$\langle B \rangle_{\text{above } f} = \frac{\int_{s_{f,||}}^{s_X} B ds}{L_{||,f}}. \tag{2.48}$$

With these substitutions, Equation 2.45 can be rewritten in the neater form:

$$C = C_0 \frac{B_f}{B_X} L_{||,f}^{-2/7} \left(\frac{B_X}{\langle B \rangle_{\text{above } f}} \right)^{2/7}. \tag{2.49}$$

Equation 2.49 is the primary governing equation of the DLS model, or simple DLS model as it is called here. The equation gives a clear relationship between parameters controlling detachment, and the location of a detachment front in a given geometry. In particular, we see that the parameters controlling detachment (n_u, f_α, $q_{||,X}$) required to achieve a given front position f are affected by:

- The parallel distance from the front to the x-point, $L_{||,f}$.
- The total flux expansion of the magnetic field from the x-point to the front location, $\frac{B_X}{B_f}$.
- The line-averaged magnetic field above the front, relative to the magnetic field at the x-point, $\frac{B_X}{\langle B \rangle_{\text{above } f}}$.

Consequently, the DLS model can be an effective way to determine how detachment is accessed and evolves in different geometries. However, just like the two-point model, there are many assumptions built in that are certainly to be broken in experiment. As such, the DLS model is likely most well-suited to qualitative comparisons between geometries, rather than accurate predictions concerning the specific movement of detachment fronts in a single geometry.

Before examining such applications of the model, let us briefly return to the junction concerning the definition of the most upstream point in this model. If, instead of the x-point, the midplane is chosen to be the location of n_u and T_u, then $q_{||}$ must be modelled above the x-point. For this region, $q_{||} = 0$ is assumed at the midplane, and the heat flux fed by a constant source of radial transport from the core, rising to $q_{||,X}$ at the x-point:

$$q_{||} = q_{||,X} \frac{B}{B_X} \frac{(L_{||} - s)}{(L_{||} - s_X)} \qquad \text{for} \qquad L_{||} > s \geq s_X. \tag{2.50}$$

Using this new profile of heat flux, the upstream temperature becomes (for $s_{f,||} < s_X$)

$$T_u^{7/2} = \frac{7}{2\kappa_{e0}} q_{||,X} \left(\int_{s_X}^{L_{||}} \frac{B}{B_X} \frac{(L_{||} - s)}{(L_{||} - s_X)} ds + \int_{s_{f,||}}^{s_X} \frac{B}{B_X} ds \right), \tag{2.51}$$

and the detachment control parameter is:

$$C = C_0 \frac{B_f}{B_X} \left(\int_{s_X}^{L_{||}} \frac{B}{B_X} \frac{(L_{||} - s)}{(L_{||} - s_X)} ds + \int_{s_{f,||}}^{s_X} \frac{B}{B_X} ds \right)^{-2/7}. \tag{2.52}$$

Inspecting this equation reveals that flux expansion, connection length, and the magnetic field upstream of the front still play a roll in determining the detachment control parameter. However, the length that matters here is a combination of the distance between the front and x-point, and distance between the x-point and midplane. When the distance between x-point and midplane is small compared to the divertor, the model converge with results form Equation 2.49. When this distance is large, then C should vary less with the location of the front.

2.4.2 Detachment Threshold Predictions

Now that the equations of the DLS model have been derived, the model can be used to gain insights pertaining to detachment access and control. First, consider predictions from the formulation which models only up to the x-point. One of the simplest uses for the DLS model is to set the front location to be at the target, $s_{f,||} = 0$. In this case Equation 2.49 becomes:

$$C_t = C_0 L_{||}^{-2/7} F_R^{-1} \frac{B_X^{2/7}}{\langle B \rangle_{\text{above } t}^{2/7}}, \tag{2.53}$$

Where the control parameter on the left hand side is the detachment threshold C_t, the parameters required to just barely detach. In other words, this number describes how easy or difficult detachment is to access in a given divertor. Equation 2.53 shows first that the threshold of detachment depends on $L_{||}^{-2/7}$, and consequently longer divertors should have lower detachment thresholds (remember $L_{||}$ here is the distance between the target and x-point, not midplane). In the derivation of the DLS equations, this term arises because the upstream temperature, and hence the upstream pressure, scales with $L_{||}^{2/7}$ with a fixed upstream density. A higher upstream pressure means higher density in the radiation region, and thus longer divertors radiate more strongly. This is an important point, as one may assume longer divertors radiate more strongly because they have 'more space to radiate'. In the context of the DLS model, however, the use of conduction allows the total integrated radiation to be expressed as an integral of temperature, and the size of the divertor does not explicitly play a role in this integral. Instead, the divertor connection length affects the pressure, which allows for more or less total radiation.

In addition to connection length, Equation 2.53 indicates that the total flux expansion of the divertor, $F_R = \frac{B_X}{B_t}$ has a role to play in determining the threshold of

detachment. In particular, the DLS model predicts an inverse relationship between detachment threshold and total flux expansion; in other words, detachment threshold scales linearly with target magnetic field given a constant x-point magnetic field. In the derivation of the DLS model, this term arose because the parallel heat flux density varies with magnetic field along a field line, since lower magnetic fields correspond to larger parallel flux tube areas. Thus heat flux density entering the front is not $q_{||,X}$, but $q_{||,X}\frac{B_f}{B_X}$. This heat flux, which is effectively the heat flux density that must be dissipated, scales with $\frac{B_f}{B_X}$. Another way of viewing this term is that for a finite flux tube with fixed input power, a higher total flux expansion leads to more volume available to radiate the total power.

Finally, Equation 2.53 shows that detachment threshold scales with the divertor averaged magnetic field relative to the x-point magnetic field, $\frac{B_X}{\langle B\rangle_{\text{above } t}}$. Specifically, with a constant target and x-point magnetic field, if the divertor averaged magnetic field increases (through a change in equilibrium between target and x-point) then the detachment threshold should decrease. In the derivation of the DLS model, this term arose in the expression of upstream temperature, since a high divertor magnetic field means a high average electron conducted heat flux density. This leads to a higher upstream temperature and pressure, which leads to more radiation; as a result, divertors with a higher averaged magnetic field are easier to detach. This relationship, however, is very weak, since the averaged field itself is difficult to significantly modify, and since the C does not scale with the averaged field, but with the averaged field to the power 2/7.

When discussing a reduction of C_t, it is important to remember that C does not scale the same with all control parameters. Specifically, a lower detachment threshold C_t means a lower minimum density or impurity fraction required to detach, but can also mean a higher maximum allowable power before the plasma reattaches.

2.4.3 Relationship to the Two-Point Model

Some of the discussion concerning the DLS model and detachment thresholds may seem eerily familiar, since detachment access was discussed in the context of the two-point model in Section 2.3.3. One may remember that in this section, the two-point model predicts that the density required to detach scales with the inverse of total flux expansion. Then, in section 2.4.2 it was shown that the DLS model can predict how the control parameters required to access detachment vary with divertor configuration. In fact, if Equation 2.53 is rearranged slightly to find only the density required to access detachment, the result is:

$$n_u = \frac{q_{||,X}^{5/7}}{\sqrt{f_\alpha}} C_0 L_{||}^{-2/7} F_R^{-1} \frac{B_X^{2/7}}{\langle B\rangle_{\text{above } t}^{2/7}}. \tag{2.54}$$

With a constant upstream heat flux and impurity fraction, and neglecting the contribution of $\langle B\rangle_{\text{above } t}$ then the scaling

$$n_u \propto F_R^{-1} \tag{2.55}$$

is recovered. And so, quite fortuitously, DLS model seems to give the same result as the two point model; The upstream density required to detach is predicted decrease linearly with total flux expansion. One may think that the agreement of these two models is expected, and indicative of some deep, shared physics. However, the agreement is a complete coincidence. In fact, both models arrive at this prediction because both models find a linear proportionality between target heat flux and upstream pressure. However, the models arrive at this proportionality for completely different reasons.

On one hand, the two-point model arrives at this condition using sheath transmission, which states for a constant temperature the target pressure and heat flux are proportional. On the other hand, the DLS model does not consider target temperatures nor target heat fluxes at all. Instead, the DLS model considers impurity radiation, which is proportional to upstream pressure. For all the heat flux in the flux tube to be dissipated, this radiation must equal the effective heat flux at the front location, which for detachment access is at the target. Hence, upstream pressure scales with target heat flux.

This difference between the two models is worth emphasising, since the scaling of detachment access with total flux expansion is an important one, and one may think the two models are saying the same thing. They are not, and this must be kept in mind if they are used predict or analyse the threshold of detachment in simulation or experiment. Fundamentally the models have different definitions of detachment, and different physics is considered and neglected in each.

2.4.4 The Window of Detachment

Another important detachment parameter that varies with different divertor configurations is the detachment window. This key value is a measure of how much detachment control parameters can vary before detachment causes a severe degradation of the core plasma - through a MARFE, for example (Multifaceted Asymmetric Radiation From the Edge) [136], [138], [139]. In effect, the window of detachment specifies the operational limits of the control parameters. In past experiments, the onset of a MARFE or some form of radiative collapse has been associated with detachment fronts approaching the x-point. As such, the detachment window can be defined as the ratio of the detachment control parameter(s) corresponding to a front at the x-point compared to those corresponding to detachment onset, $\frac{C_X}{C_t}$.

In other words, a detachment window of 2 means that electron density can be at maximum doubled whilst still maintaining stable operational detachment. Now of course a detachment front moving to the main x-point does not always correspond with radiative collapse. In fact, there are divertor regimes such as the x-point radiator which benefit from stable radiation fronts at the plasma x-point [138], [140],

[141]. Nevertheless, many tokamaks still aim to achieve a stable detachment front in the divertor region, and for this purpose the window of detachment is a very useful parameter.

So what does the DLS model predict concerning the window of detachment in different geometries? It is relatively straightforward to notice that in the context of the DLS model which only extends to the x-point (Equation 2.49), C_X is infinite, and so is the window of detachment. In other words, it is infinitely difficult to push a detachment front to the x-point; this should make sense, as in this version of the model the x-point is the source of heat. Hence, this version of the model is not very useful concerning the window of detachment. Instead, one can turn to the version of the model which extends to the midplane (Equation 2.52). In this case, the window becomes:

$$\frac{C_X}{C_t} = F_R \left(1 + \frac{\int_0^{s_X} \frac{B}{B_X} ds}{\int_{s_X}^{L_{||}} \frac{B}{B_X} \frac{(L_{||}-s)}{(L_{||}-s_X)} ds} \right)^{2/7} . \tag{2.56}$$

This equation produces several interesting consequences. First, the window of detachment scales linearly with the total flux expansion of the divertor. In addition, the window scales with the ratio of two line integrals in different regions of the equilibrium. From these integrals, it should be clear to see that the window of detachment increases if the distance s_X is increased relative to the distance $L_{||}$. This means that if the length of the divertor is increased relative to the total connection length (from midplane to target), then a wider detachment window can be achieved.

Crucially, Equation 2.56 also shows that if two divertor equilibria have the same configuration upstream of the x-point, then the detachment window is entirely dependent upon the threshold of detachment. Thus, comparing divertor configurations with the same rough upstream profile, any difference in detachment threshold tells us how the detachment window changes. For this reason, much of the analysis and discussion in subsequent sections will focus on detachment thresholds.

This last conclusion is quite an important one, and is related fundamentally to setup of the DLS model. After all, the DLS model deals with the characteristics of a plasma and magnetic equilibrium *upstream* of the cold end of a detachment front. Consequently, any physics downstream of the front location is not important for the location of detachment in the context of the DLS model. This implies that plasmas which have a similar magnetic configuration upstream of the x-point should show similar front movement physics as the detachment fronts approach the x-point. Whether it be a Super-X divertor or X-point target or standard configuration, if two equilibria look the same upstream, then the behaviour of detachment fronts should converge as the fronts are pushed upstream. Of course, a reader should not infer from this discussion that the DLS treatment of detachment front movement is correct. One may expect that physics downstream of a detachment front can affect power balance, through the strength of recycling for example. This aspect of the

DLS model is explored in Chapter 5.

2.4.5 Detachment Location Sensitivity

In addition to examining how detachment thresholds vary, the DLS model, as the name suggests, can be used to study the location sensitivity of detachment. Here, the detachment location sensitivity is defined as the rate of change of a detachment front location with respect to a change in the lumped control parameter C. In other words, if a detachment front moves a great deal when the power of a device is modified slightly, then the detachment front is in a region of high sensitivity. Sensitivity is a crucial parameter for detachment control, and if it is beneficial for a detachment front to be passively held in a location, that location should be engineered to have low detachment location sensitivity.

To find an equation for detachment location sensitivity, Equation 2.49 can be differentiated with respect to parallel front location from the target, $s_{f,||}$. Taking the inverse of the resulting expression gives:

$$\frac{ds_{f,||}}{dC} = \frac{1}{C}\left(\frac{1}{B_f}\frac{dB_f}{ds_{f,||}} + \frac{2}{7}\frac{1}{L_{||,f}} - \frac{2}{7}\frac{1}{\langle B\rangle_{\text{above } f}}\frac{d\langle B\rangle_{\text{above } f}}{ds_{f,||}}\right)^{-1}, \tag{2.57}$$

the equation for parallel detachment location sensitivity. From this equation several conclusions can be drawn. Firstly, detachment location sensitivity should decrease with an increase in fractional magnetic field gradient at the front location, $\frac{1}{B_f}\frac{dB_f}{ds_{f,||}}$. Physically, this is because if a detachment front will encounter higher magnetic fields moving along a SOL ring, this effectively means it encounters higher heat flux densities (or less volume for radiation). Consequently, it becomes harder to dissipate this higher heat flux density, and the control parameter must increase significantly to compensate.

Concerning this magnetic field gradient term, Equation 2.57 indicates that it should be theoretically possible to have a negative detachment sensitivity, given a sufficiently negative $\frac{dB_f}{ds_{f,||}}$ term. In other words, given a sufficient total flux contraction along a divertor - as is seen in horizontal inner leg divertors for example - there may be regions of negative location sensitivity. This negative sensitivity means that a lower control parameter is needed to access a more detached state; in other words, it is 'easier' to be more detached. Hence, the location of fronts in these regions should be unstable, as any detachment front in a negative sensitivity region should become increasingly more detached until a region of positive sensitivity is reached.

Additionally, Equation 2.57 demonstrates that sensitivity should naturally decrease as detachment fronts move towards the x-point. This is because, as detachment fronts move further from the targets, the control parameter C tends to increase, and the effective connection length $L_{||,f}$ decreases. From Equation 2.57, both of these changes will contribute to lowering the detachment sensitivity. One may understand

this as partly due to the non-linear variation of upstream pressure with effective connection length. Because $T_u \propto L_{||,f}^{2/7}$, a given step in parallel length will cause a much larger relative upstream temperature drop if a front is very close to the x-point.

Inspecting Equation 2.57, one may notice that if the detachment front approaches the x-point, and $L_{||,f}$ goes to 0, the sensitivity will approach 0. In short, it becomes infinitely hard to push a detachment front to the source of heat, which is the x-point. Remember, however, that the upstream can also be defined as the midplane, through Equation 2.52. Under this formulation, the detachment sensitivity will not be reduced to 0 at the x-point, and detachment fronts may move past the x-point towards the midplane. However, this is not an incredibly useful application. This is because as radiation fronts move past the x-point, it has been experimentally observed that they tend to start moving radially inwards to the core, rather than continuing in the parallel direction along a flux tube [138]. As such, a detachment model for movement along a flux tube is not well suited here.

Additionally, Equation 2.57 tells us that the gradient of the averaged magnetic field also contributes to sensitivity. However, this slope will always be less than the magnetic field gradient at the front, and its contribution is less given the 2/7 factor. As such, this term will generally have negligible contributions to the detachment location sensitivity.

Thus far the sensitivity of detachment front locations measured in the parallel direction have been considered. Indeed, the front location in parallel space may be important for determining parameters such as the upstream temperature. However, it is also useful to consider the poloidal distance between front and target, $s_{f,pol}$. Since this is typically how the front is measured and controlled in experiment, and determines the proximity of the front to physical structures. Using coordinate transformation $ds_{pol} = \frac{B_{pol}}{B} ds$, Equation 2.57 can be rewritten in poloidal space,

$$\frac{ds_{f,pol}}{dC} = \frac{1}{C}\left(\frac{1}{B_f}\frac{dB_f}{ds_{f,pol}} + \frac{2}{7}\frac{1}{L_{||,f}}\frac{B_f}{B_{pol,f}} - \frac{2}{7}\frac{1}{\langle B\rangle_{\text{above } f}}\frac{d\langle B\rangle_{\text{above } f}}{ds_{f,pol}}\right)^{-1}. \tag{2.58}$$

Now it is clear Equation 2.58 looks very analogous to Equation 2.57, but with an additional term $\frac{B_f}{B_{pol,f}}$. This term indicates that in regions of low poloidal pitch, that the detachment location sensitivity should be low in the poloidal plane. Because this term is not present in Equation 2.57, the term does not impact the physics of detachment, but is simply a result of coordinate transformations. As such, when the location of a detachment front becomes less sensitive in regions of low poloidal pitch, this is simply be due to the change in conversion between parallel and poloidal space; poloidal distance being smaller in that region, for a given change in parallel distance.

2.5 The Extended DLS Model

2.5.1 Formulation of the Model

When it comes to detachment, the DLS model is a powerful tool to understand how certain features of divertor geometries influence detachment. However, the interpretability and quasi-analytical nature of this formulation comes at a price, as many assumptions have been made that may be broken in real divertors. One assumption in particular changes very little about the formulation of the model, but makes the output of the model more interpretable; and that is the assumption of a thin thermal front. For high power reactors with radiators with wide electron cooling functions, this assumption may be broken. Consequently, it may be useful to solve the heat balance of the DLS model without making this assumption. The resultant formulation has been created as part of this thesis, and is termed the *Extended DLS Model*.

The formulation of the extended DLS model is similar to the simple DLS model, in that it solves Equation 2.35 upstream of the cold end of the detachment front, assuming constant static electron pressure. Like the simple model, the extended DLS model takes a front position in a given divertor geometry as an input, and outputs control parameters required to achieve said front location. Rather than making attempts to solve the power balance analytically, the extended DLS model solves it through numerical integration. The equations

$$d\left(\frac{q_{||}}{B}\right) = \frac{n_u^2 T_u^2 f_\alpha L_\alpha(T)}{BT^2} ds, \tag{2.59}$$

and

$$q_{||} = \kappa_{e0} T^{5/2} \frac{dT}{ds}, \tag{2.60}$$

form a set of coupled differential equations that can be solved using any computational integrator to give temperature and heat flux profiles for a given divertor geometry.

The only extra information needed are the boundary conditions, and the values of κ_{e0} $L_\alpha(T)$, T_u, n_u, f_α. For the boundary conditions, the model begins by integrating from the front, and in the previous formulation of the model, this is where both T and $q_{||}$ should reduce to 0. The same treatment cannot be made for computational integration, since electron cooling functions are 0 at $T = 0$. Consequently, if the heat flux is 0, the temperature cannot evolve, and if the temperature is 0, the heat flux cannot evolve, and the profiles are entirely invariant. Because of this, one may simply specify a low temperature and heat flux density. As shown in Appendix A, the specific choice of these values does not matter as long as they are sufficiently low. For results in this section, the choice of $q_{||,f}$ =1 MWM^{-2}, and T = 1 eV is used.

In terms of the constants, $\kappa_{0e} \simeq 2000$ Wm^{-1}eV$^{-7/2}$ [83]. Moreover, for a given impurity residence time, $L_\alpha(T)$ [142] can be calculated from a collisional radiative model, or an analytical approximation can be made. T_u is more difficult to provide,

since it is both an input to the dissipation model, and an output of the numerical integration. As a result, the extended DLS model runs this integration iteratively in order to determine the correct T_u, and begins this iteration with an initial guess:

$$T_{u,initial} = \left[\frac{7}{2\kappa_{e0}} q_{||,X} \left(\int_{s_X}^{L_{||}} \frac{B}{B_X} \frac{(L_{||} - s)}{(L_{||} - s_X)} ds + \int_{s_{f,||}}^{s_X} \frac{B}{B_X} ds \right) \right]^{2/7}, \tag{2.61}$$

or

$$T_{u,initial} = \left(\frac{7}{2\kappa_{e0}} q_{||,X} \int_{s_{f,||}}^{s_X} \frac{B}{B_X} ds \right)^{2/7}, \tag{2.62}$$

depending on the definition of the upstream. Integration with this initial guess will then produce an output upstream temperature $T_{u,output}$, which will inevitably be different from the input T_u. Thus, the integration will be repeated, with a new input temperature $T_{u,input} = (1 - F_{Tu})T_{u,input} + F_{Tu}T_{u,output}$. The under-relaxation factor F_{Tu} is typically 0.2. The iteration is complete when the difference between the input and output upstream temperature is below a user-requested tolerance.

The final requirement now to produce a self-consistent detached temperature profile from the extended DLS model is the knowledge of n_u, f_α, and $q_{||,X}$. However, remember that the purpose of the DLS model is to determine the control parameter(s) required for a detachment front in a particular location in a given geometry. As such, one of these three parameters is the output of a model run, and the other two are inputs. Specifying and measuring n_u and f_α is straightforward, but the control parameter $q_{||,X}$ is less so. If the modelled region extends up to the x-point, $q_{||,X}$ is simple to define, since it is simply the fixed heat flux entering the top of the modelled region. If the modelled region extends up to the midplane, however, $q_{||,X}$ is controlled through a fixed radial source of heat from the x-point to midplane.

In the case of n_u and f_α as inputs, the code determines whether the area from x-point to midplane is being modelled or not. If not, iterations of the integration are performed until the input and output upstream temperatures agree. The final temperature and heat flux profiles are the output of the model, and with this output $q_{||,X}$ can be found, and thus the lumped control parameter C is calculated.

If the upstream area between x-point and midplane is considered, however, then there is an additional iterative loop that guesses a strength of the radial heat source, and varies it until a heat flux at the midplane of 0 is achieved (within a user specified tolerance). The x-point heat flux can then be extracted from the resultant heat flux profile.

When $q_{||,X}$ is used as an input for the model, the situation is more intricate dealing with a domain ending at the x-point, and less so for a domain extending to the midplane. For a domain extending to the midplane, a constant radial heat source is specified, and either n_u and f_α are varied until the heat flux density at the midplane is 0 within the user-specified tolerance.

In the case of a domain spanning to the x-point, initial guesses must be made for the output of the model (be it density or impurity fraction), and when the consistent temperature profiles are achieved, the code determines whether the outputted $q_{||,X}$ is greater or less than the requested input $q_{||,X}$. If the output heat flux is greater, the control parameter output (either density or impurity fraction) will be lowered, and the entire process begins again. In this way the code iterates until the residual between the requested and determined heat flux is lower than some user-determined threshold.

Though using $q_{||,X}$ can be slightly more difficult to run with than the other control parameters, it is still worth using since - the context of the extended DLS model - not all control parameters are equivalent. As shall be shown shortly, using different control parameters produces different detachment windows and sensitivities for the same geometry.

2.5.2 Results from the Extended DLS Model

The formulation of the extended DLS model has several advantages over the simplified DLS model. First, the model does not simply produce control parameters as a model output, but entire self-consistent profiles of temperature, heat flux, and radiation which may be interrogated. For example, the DLS model has applied to an outer leg geometry for the MAST-U Super-X divertor, with an upstream density of 5×10^{19} m^{-3}. The model has been run for five detachment front locations using a cooling curve approximating neon at $\tau = 1$ ms, shown in Figure 2.4. The output control parameter was upstream heat flux, and the impurity fraction was fixed at 5%. The resultant heat flux and temperature profiles for these extended DLS model runs can be seen in Figure 2.5.

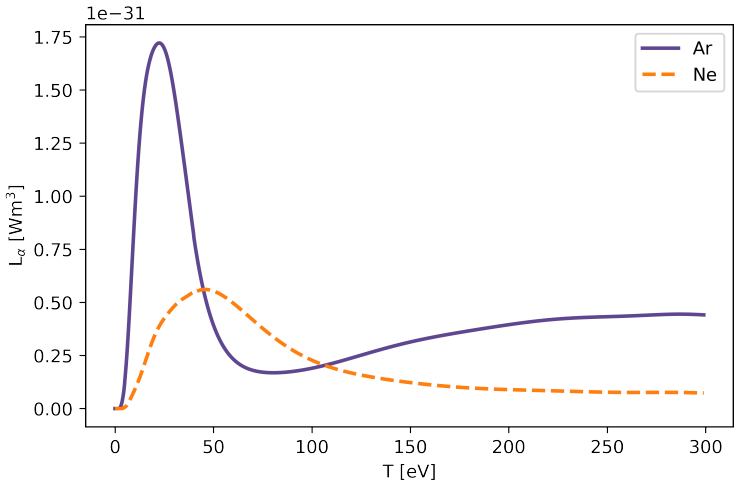

FIGURE 2.4: Analytically approximated electron cooling function for argon and neon at $\tau = 1$ ms.

Figure 2.5's results show that using neon, even at incredibly high powers, results in very gradual radiation along the divertor leg. In these cases, the concept of a thin

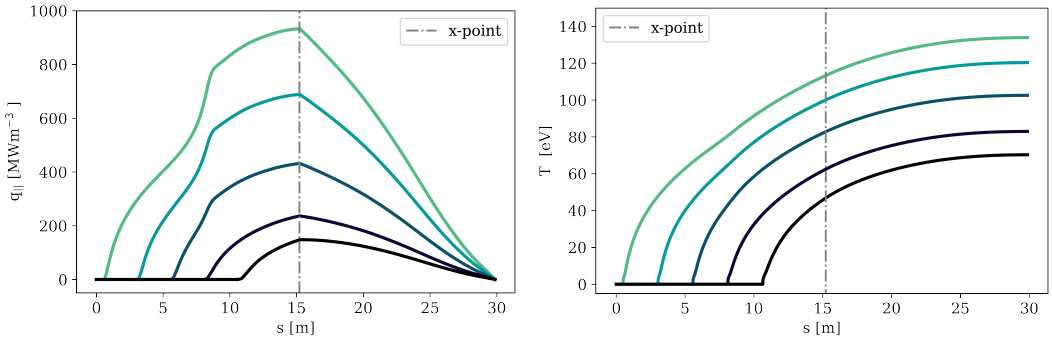

(a) (b)

FIGURE 2.5: The a) electron conducted heat flux density and b) temperature profiles for four varying degrees of detachment as calculated by the extended DLS model with an artificial neon impurity.

radiation region or thermal front is likely not valid, and thus the simple DLS model will likely not be perfectly suited. To quantify just how much the detachment front movement results may differ to the simple DLS model predictions, a more fine scan using neon at n_u=5×10^{19} m^{-3}, f_α = 5% was performed, but this time with 30 points along the scan. This process was also repeated with a cooling curve approximating argon radiation at $\tau = 1$ ms, shown in Figure 2.4. The results of front movement against normalised control parameter are shown in Figure 2.6a, where the control parameter is $q_{||,X}^{-5/7}$.

From Figure 2.6a it is clear to see the variation in front movement of the extended DLS model (labelled 'neon C=$q_{||,X}^{-5/7}$)' can differ significantly from the results of the simple DLS model (labelled 'Simple DLS'). In particular, the extended model run with neon predicts nearly a 2x higher window than the window of 2.78 from the simple DLS model for a front to move from 0m to 12m (roughly 80% to the x-point). Even running with argon produces a difference in window or location sensitivity, shown by the curve labelled 'argon C=$q_{||,X}^{-5/7}$)'. However, the reduction in sensitivity here is only ≈10%. This lessened difference for argon is expected, since the cooling curve in Figure 2.4 has a much more localised peak than that of neon, and thus radiation occurs in a much more narrow physical region.

Overall Figure 2.6a indicates there can be significantly different detachment location sensitivities and windows when the effects of a wide thermal front are considered, but it does not indicate exactly what these effects are. Remembering the formulation of the simple DLS model, the assumption of a thin thermal front allowed four simplifications:

- The upstream temperature can be found analytically, since the heat flux density upstream of the front location is assumed to vary only due to magnetic field variation.
- The term C_0 remains constant, since with a thin thermal front the changing temperature limits of $\int_{T_f}^{T_u} T^{1/2} L_\alpha(T) dT$ do not significantly impact the integral.

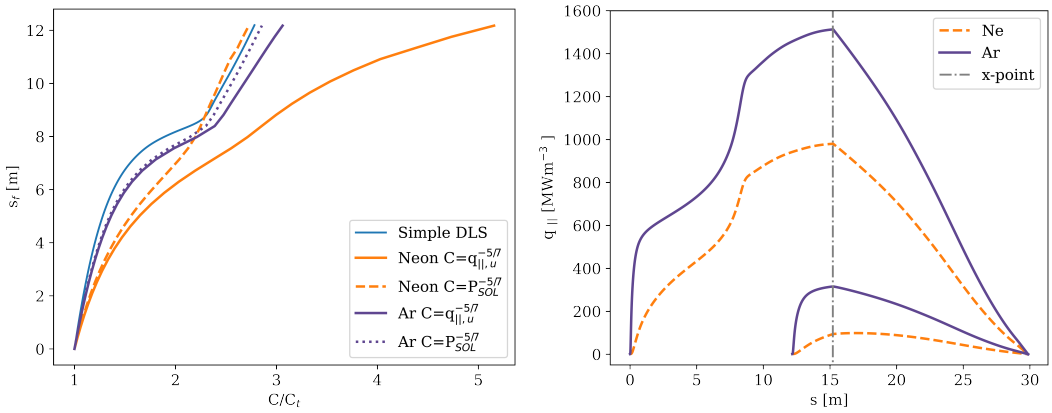

(a) (b)

FIGURE 2.6: The a) The parallel detachment front position plotted as a function of detachment control parameter for several power scans in the MAST-U Super-X geometry. Results are for the DLS model, and the extended DLS model with neon and argon impurities, using two definitions of the power control parameter. b) The parallel heat flux profile along a field line for the first and last points of the scans in a).

- The magnetic field can be taken out of the integral of impurity losses, as its value at the front location. Remember that this term can be thought of as a scaling of volume available for radiation.
- The total dissipated power corresponds to the peak heat flux at the x-point, since there it is assumed there is no dissipation upstream of the x-point.

The degree of breaking of each of these simplifications can be assessed for the extended DLS model data, to determine what the leading causes of difference are. In the case of both neon and argon, the upstream temperature difference of a front at 0m vs 12m is only ≈10% lower than the simple DLS model predictions. Hence, the difference in upstream pressure is not a significant source of variation between models.

The constant C_0, however, increases by 50% as the detachment front moves from 0 to 12m in the neon power scan, making the scan less sensitive. This increase should be expected, since in this power scan the conducted heat flux is lowered considerably, as can be seen in the heat flux profiles for the 0m and 12m runs in Figure 2.6b. This leads to a sizable drop in upstream temperature, drastically reducing the integral $\int_{T_f}^{T_u} T^{1/2} L_\alpha(T) dT$, and increasing C_0. In the case of argon, the constant C_0 is also raised as the divertor becomes more detached, though only by 27% as the cooling function is much more localised around a lower temperature of 25 eV.

In terms of the effect of magnetic field, an impurity with a wide radiation region is expected to have more sensitive front movement than the simple DLS model. This is because in such a case the volume available for radiation does not scale with the magnetic field at the cold end of the front, but instead scales with the magnetic field over the entire front region. Consequently, as detachment fronts move in a given

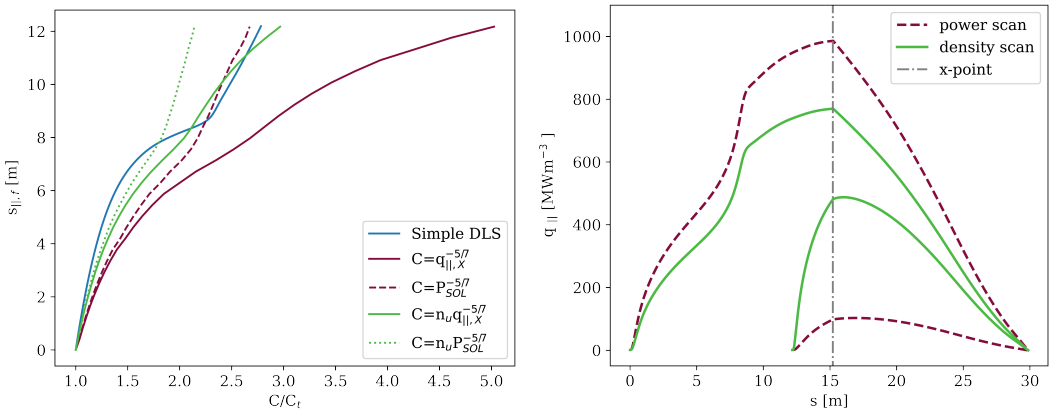

(a) (b)

FIGURE 2.7: The a) The parallel detachment front position plotted as a function of detachment control parameter for a power and density scan in the MAST-U Super-X geometry. Results are for the DLS model, and the extended DLS model with a neon impurity, using two definitions of the power control parameter. b) The parallel heat flux profile along a field line for the first and last points of the scans in a).

geometry, the effect of the front magnetic field on movement is lessened. Indeed in the case of neon, this effect of a non-constant magnetic field in the radiating region increases the sensitivity on average by 50%. In the case of argon, this magnetic field effect increases the sensitivity by 30%.

Finally, the extended DLS model results may differ significantly from simple DLS predictions since $q_{||,X}$ does not always correspond to the total heat flux dissipated by impurity radiation. This is because radiation upstream of the x-point may cause the peak $q_{||}$ to drop for the same total heat source. As such, as input power is reduced and a front moves close to the x-point, $q_{||,X}$ may drop more than the total input power, and the front movement should appear less sensitive. Indeed, the location sensitivity of the entire power scan for neon is reduced by a factor of 2 due to his effect. For argon, the sensitivity reduces by 10%. This can be seen explicitly if the same curves are plotted, but with the power into the SOL, P_{SOL}, used as the control parameter. This power can be calculated using the strength of the heat source above the x-point, and the curves using P_{SOL} as a control parameter are labelled with '$C = P_{SOL}^{-5/7}$'. Comparing these curves to the curves which use $q_{||,X}$ as a control parameter indeed reveals a sizable reduction in detachment location sensitivity when $q_{||,X}$ is used.

Now another interesting output of the extended DLS model alluded to previously is that not all control parameters have the same impact on detachment, and the regime of the run can impact results. In other words, a percentage change in n_u is not necessarily the same as an identical percentage change in $q_{||,X}^{-5/7}$. In particular, the upstream heat flux is a key parameter in determining how physically wide a radiation front is, and heat flux scans can therefore change the physics of detachment in more nuanced ways than the simplified model assumes.

To demonstrate this, the detachment scan performed previously with neon was repeated, but with density as the varied control parameter rather than power. The comparative results of the power and density scan are shown in Figure 2.7a. From the curve labelled Figure2.7a the density scan is *more sensitive* in certain locations than simple DLS model predictions, in stark contrast to the power scan. Why are the two scans so different? Well, the reduced importance of magnetic field due to wide fronts increases the location sensitivity of the density scan by roughly 30%. However, this is similar to the power scan, and does not explain the difference between the two.

The primary difference between the two scans is that the peak heat flux is not reduced as much in the density scan, and so the front width at the end of the scan is smaller when density is the varied control parameter. This can be seen in the parallel heat flux profiles of the start and end of each scan, shown in Figure 2.7b. This thinner front in the density scan has two effects; first, the integral in C_0 is not as affected, and indeed C_0 is only raised by 10% in the density scan. Secondly, there is less radiation upstream of the x-point at the end of the density scan. Thus, the reduction of $q_{||,X}$ with a fixed P_{SOL} only reduces the overall location sensitivity by 40%. In the power scan, on the other hand, this effect reduces the sensitivity by roughly a factor of 2. The impact of this effect can be seen comparing the density scan with $q_{||,X}^{-5/7}$ incorporated as a control parameter, and the same plot where $P_{SOL}^{-5/7}$ is instead used as a control parameter (labelled '$C = n_u P_{SOL}^{-5/7}$'). Though there is a significant reduction in sensitivity between these two curves, it is not as stark as the difference between the two versions of the power scan.

Overall, these initial results from the extended DLS model reveal several conclusions about the impact of wide thermal fronts on detachment evolution. In particular, these results have shown that there is no uniform deviation of the extended DLS model from the simple DLS model. Several effects act to reduce the location sensitivity of detachment, whereas others act to raise the location sensitivity. A key effect which increases detachment location sensitivity is the lessened dependence of control parameters on the magnetic field at the cold end on the front. An important effect which reduces location sensitivity is the variation of C_0, assumed to be constant in the simple DLS model. Finally, these results highlight how there can be important nuances related to the choice of control parameters. It has been shown that both the choice of varied controller, and the specific definition of divertor heat flux, can have significant effects on the perceived location sensitivity of a detachment scan.

2.6 Summary

Throughout this chapter the underlying physical principles of transport in tokamak divertors has been outlined, and various models for divertor physics have been introduced. When it comes to high-fidelity accurate models, SOLPS-ITER is a standard

widely used architecture in the community. The code is a combination of a fluid code and Kinetic Monte-Carlo code modelling the plasma and neutral species respectively, and can model the full 2D geometry of a tokamak divertor. SOLPS-ITER is used in later chapters of this thesis to further understand how divertor conditions and detachment control vary with alternative divertor configurations.

In addition to complex 2D simulations, reduced modelling is a very powerful tool for developing understanding of divertor transport. The two-point model is one of the most powerful of these reduced tools, and predicts how upstream and downstream conditions along a flux tube vary with divertor configuration. Several versions or corrections of the model exist depending on the regime of focus.

Finally, the DLS model is a more recently developed tool which predicts the variation of detachment access and the movement of detachment fronts with respect to changes in detachment controllers [4], [136]. One particularly important application of the model is in predicting and understanding how resistant or sensitive front movement is in different geometries.

As part of this thesis, the DLS model has been generalised to be applied to any arbitrary divertor configuration and corresponding magnetic field profile. Several versions of the simple DLS model have been developed, including a version which treats the upstream as the midplane, and one which treats the upstream as the divertor entrance. Finally, an 'extended' version of the DLS model has been developed, which outputs numerically computed, self consistent heat and temperature profiles along a detached flux tube. This extended version of the model can deal with an arbitrarily wide radiating region, and can be applied using different impurity cooling curves. The widening of this radiating region can even cause the relative effects of electron density, impurities, and power to differ relative to the simple DLS model. Consequently, this extended model could be used to study detachment where radiation is expected along an entire divertor leg, not in a localised front.

Chapter 3

Simulating the Impacts of Alternative Divertor Features

In Chapter 2, several reduced models for alternative divertors were introduced, including multiple versions of the two point model, and detachment location sensitivity model. These models can produce results quickly, and allow for better understanding of the underlying physics, which can help influence design and operation choices for reactor tokamaks. However, the benefits of clarity and intuition come at the cost of many simplifying assumptions that may be broken in reality.

As a consequence, it is important to assess the accuracy of predictions from simplified modelling, and whether given divertor features have the predicted impact on performance when more complicated physics is taken into account. To investigate this topic, SOLPS-ITER simulations [1], [2] have been developed of isolated divertor legs in simplified geometry, as shown in Figure 3.1. These simple geometry simulations allow for complex physics modelling, whilst still being able to isolate the effects of individual divertor features.

Over the following chapter, the features of divertor connection length, magnetic flux expansion - both poloidal and toroidal - and physical baffling will be investigated using these isolated divertor SOLPS-ITER simulations. Results from these simulations are compared to the two-point model and DLS model. Much of the work presented in this chapter forms the basis of a paper published in *Nuclear Fusion* [6].

The effect of individual features on target conditions, detachment access, and detachment evolution is studied. Broad agreement between these simulations and simple modelling is found, though physics such as radial transport of heat and volumetric momentum loss is required to fully understand the effect of a given feature.

Beyond simple simulations, it is also crucial to understand how individual features interact to influence the performance of a fully integrated divertor in complex simulations and experiments. These topics are investigated further in Chapters 4 and 5 respectively.

3.1 Simulation Setup and Comparison Methodology

Before delving into a comparison between simple models and SOLPS-ITER, it is first important to set out how this comparison may be achieved. The simulations presented in this chapter are of isolated divertor legs [143], which model the region of a tokamak divertor downstream of the x-point. These legs were created by *Matlab* scripts, which generate an orthogonal grid; the length, width, grid resolution, and angle of the leg to the vertical are all user-specified (though typical grid resolution is roughly 300x50). The grid is split by a ratio 1:4 into the PFR and SOL, separated by the separatrix. These rectangular divertor legs can then be further modified. Modifications used in this study include introducing poloidal flaring or contraction through conformal mapping, used in Section 3.3, and bending of the grid paths through the introduction of an intermediate circular segment, used in Section 3.5.

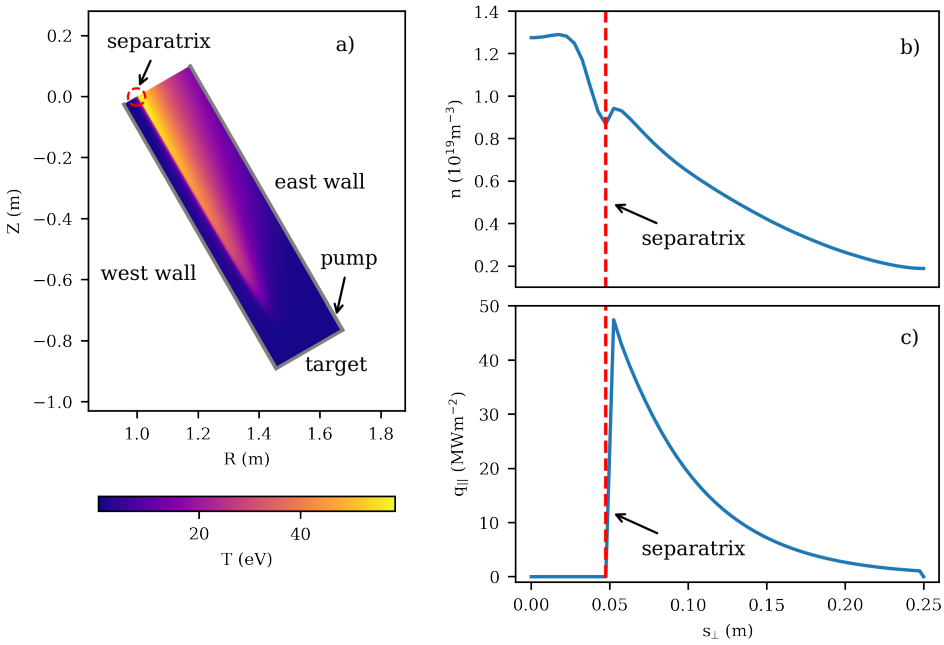

FIGURE 3.1: a) A diagram of an isolated divertor leg at 30 °to the vertical. A 2D electron temperature profile for a detached SOLPS-ITER simulation of this geometry is superimposed on the diagram. b) An electron density profile for the simulation in a) at the top of the grid, plotted as a function of cross-field poloidal distance from the inner edge at the divertor entrance. c) A conducted electron heat flux density profile for the simulation in a) at the top of the grid, plotted as a function of radial distance from the inner edge at the divertor entrance.

For this study, the grids have a magnetic field profile $B = \frac{B_0}{R}$, where B_0 is user-specified. If the grid is straight with no poloidal flaring, the poloidal field is calculated through a constant user specified poloidal pitch, $\Theta = \frac{B_{pol}}{B}$. The divertor legs have fixed density and heat flux density boundary conditions at the upstream boundary (x-point), with a user-requested heat flux and density decay profile, as shown in Figure 3.1. The upstream heat flux is split 50/50 between the electron and

ion channel, and the target has a 100 % recycling fraction. Pumps with a pumping fraction of 1% are implemented, situated near the far SOL side of the target. The upstream boundary conditions are chosen to roughly replicate what MAST-U is capable of: separatrix densities of $\approx$ 1E19 m^{-3} and peak parallel heat flux densities of $\approx$ 50 MWm^{-2}. Heat flux widths are specified such that they are of the order 1cm at the midplane, though due to flux expansion they are much larger measured at the x-point. The anomalous radial transport coefficients are constant across the entire domain, and do not change from simulation to simulation.

In order to effectively study detachment and strongly radiating regimes, the SOLPS-ITER simulations in this chapter have been run with an artificial impurity energy sink model. This model assumes a uniform user-defined impurity fraction, and uses an analytic electron cooling function which approximates that of nitrogen with non-coronal effects, at $n_e\tau_\alpha = 10^{20}$ m^{-3}ms [4], [98]:

$$L_N(T) = \begin{cases} 5.9 \times 10^{-34} \frac{(T-1)^{1/2}(80-T)}{1+3.1\times10^{-3}(T-1)^2}, & \text{if } 1 \leq T < 80. \\ 0, & \text{otherwise.} \end{cases} \tag{3.1}$$

A plot of this electron cooling function is shown in Figure 3.2. To ensure 1D models along a field line are compared meaningfully to the 2D code SOLPS-ITER, the characteristics of the 'killer' flux tube in SOLPS-ITER will be used for comparison to simple models. This is the flux tube where the target heat flux density peaks; though it can change with plasma parameters and detachment, for consistency the average killer flux tube is used. Unless otherwise stated, it is the third poloidal grid ring from the separatrix.

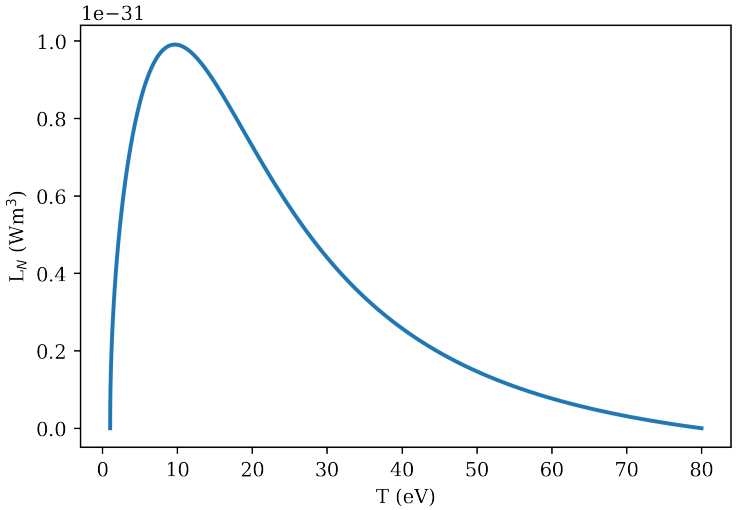

FIGURE 3.2: An analytically approximated electron cooling function for Nitrogen, the form for which is given in Equation 3.1.

In addition, comparing simple detachment models with simulation is not entirely straightforward since the location of detachment can have many definitions. In the context of the DLS model, the detachment front location is the point at which

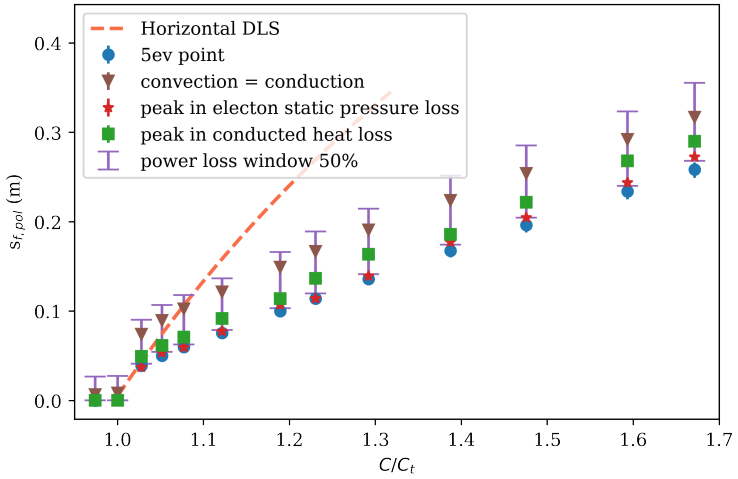

FIGURE 3.3: The SOLPS-ITER detachment location for the third SOL ring of grid II-1, plotted as a function of control parameter variation. The control parameter varied is the impurity fraction, and the detachment front position is determined using a range of different methods. These methods are compared to DLS theory, indicated by the dashed curve.

the heat flux and temperature drops to 0, and is the cold end of a thin region in which all of the heat dissipation occurs. In simulation, however, radiation can occur throughout the divertor leg, and at no point does temperature or heat flux drop to exactly 0. Consequently, one could use many analogous definitions to track the front in SOLPS-ITER. Definitions for the location of detachment considered in this work include:

- The point at which the electron temperature drops to 5eV. This uses the definition of a detachment front as the transition to a low-temperature detached region.
- The point at which conduction and convection are equal. This tracks the definition of the detachment front as the location that separates the upstream conduction-dominated plasma and downstream convection-dominated partially ionised gas.
- The location of peak static pressure loss. This uses the definition of the detached region as a region containing significant volumetric momentum sinks.
- The location of the peak in electron-conducted heat flux loss. This tracks the definition of a detachment front as the location at which all the heat dissipation occurs.
- The smallest physical region containing most (50%) of the electron-conducted heat flux loss. This is analogous to the DLS definition of a detachment front as the location at which all the heat dissipation occurs.

These various definitions of detachment can be seen for an isolated divertor leg, plotted as a function of detachment control parameter, in Figure 3.3. To match most closely to the DLS model definition of a detachment front, the peak in electron conducted heat flux loss is used as the location of detachment for these isolated divertor simulations. Moreover, from Figure 3.3 one can see that the window comprising 50% of power loss roughly encapsulates all other definitions of the location of detachment. Because of this, and because this window is analogous to the DLS model definition of a detachment front, this 50% power loss window is used for the uncertainty in detachment front position.

A final consideration to make when comparing the DLS model to SOLPS-ITER simulations is the definition of the detachment control parameter C. Unless otherwise stated, the detachment control parameter for simulations is equal to $\frac{n_u\sqrt{f_\alpha}}{q_{||,X}}$. Here, n_u is the electron density at the divertor entrance on the killer flux tube, f_α is the input impurity fraction, and $q_{||,X}$ is the parallel electron conducted heat flux density at the divertor entrance on the killer flux tube.

3.2 Connection Length and Long Leg Divertors

One of the simplest ways to change the performance of a divertor is through modifying the parallel connection length. This length - along with the machine power - is important in setting the temperature difference between the upstream and target. As such, increasing this connection length can be a powerful way of maintaining good pedestal pressures and acceptable target conditions simultaneously.

Moreover, as discussed in Chapter 2, a long connection length will increase the density at a given temperature along the SOL given a constant upstream pressure, and because of this, longer divertors generally radiate more efficiently. Of course, intuition also tells us that longer divertors should have more radial transport losses of heat, leading to broader target heat load profiles, though this is generally not explicitly incorporated into simple 1D models.

Over the following section, the effects of connection length on divertor performance and detachment will be investigated. To study the effects of connection length on divertor performance, four divertor leg grids of poloidal length 0.75, 1 , 1.25 and 1.5m were generated, and are shown in Figure 3.4. Each leg has identical flux expansion and width. All are tightly baffled, with the walls located at the edge of the plasma domain. This connection length study has implications for divertor concepts such as the x-divertor, snowflake, Super-X, and long-legged tightly baffled divertor, which all leverage long connection lengths.

3.2.1 Attached Target Conditions

Simulations of divertors of various lengths can be used to validate two-point model predictions for attached target conditions for alternative divertors. In particular,

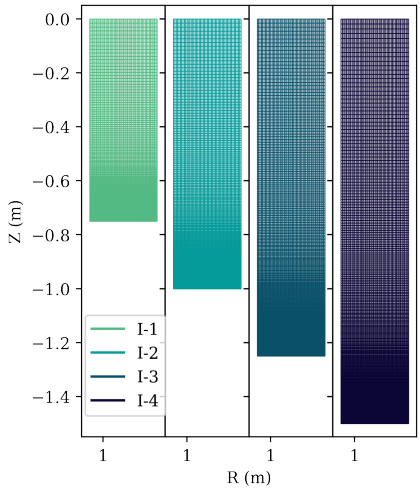

FIGURE 3.4: The poloidal cross-sections of four vertical box divertor grids with varying connection lengths.

in Chapter 2 it was shown that in an attached conduction-limited regime, the target temperature of a divertor should scale as $L_{||}^{-4/7}$, according to Equation 2.25. To verify this, the target temperatures of the killer flux tube are plotted for attached simulations of each of the four grids in Figure 3.4 with identical density, heat, and impurity boundary conditions $n_u = 1\text{E}19\ \text{m}^{-3}$, $q_{||,X} = 50\ \text{MWm}^{-2}$, $f_N = 0.1\%$.

The variation of target temperature, shown in Figure 3.5a demonstrates good agreement with the $L_{||}^{-4/7}$ dependence predicted by the two-point model. As a result, increasing the connection length of a divertor can be an effective way to alleviate target temperatures, but this change grants diminishing returns due to the nonlinear $-4/7$ dependence.

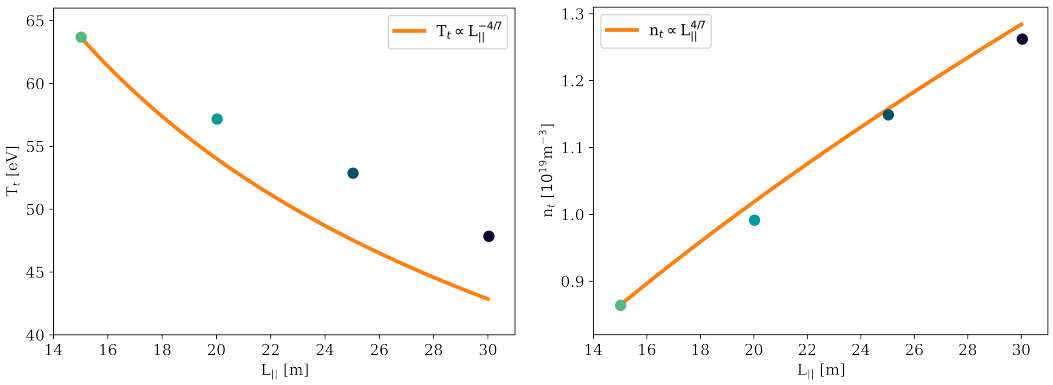

(a) (b)

FIGURE 3.5: a) The target temperatures for attached simulations of legs I-1 to I-4, plotted as a function of connection length. b) The target densities for attached simulations of legs I-1 to I-4, plotted as a function of connection length.

It is important to note the agreement in target temperature variation is not perfect, and that there is a weaker dependence of T_t on connection length in SOLPS-ITER compared to the two-point model. This is because the temperatures here are

still quite high, and the simulations are in between the conduction and sheath limited regimes.

In addition to target temperatures, the two-point model predicts that increasing the connection length of a divertor should increase the target density with $L_{||}^{4/7}$ according to Equation 2.26. A plot of target density on the 'killer' flux tube against connection length is shown in Figure 3.5b. In this figure, the target density is indeed higher with longer divertors, with an increase which matches well with the two-point model.

3.2.2 The Threshold of Detachment

In addition to variations in attached target conditions, modelling predicts divertor connection length should influence access to and control over detachment. Specifically, the DLS model predicts the detachment threshold should vary with $L_{||}^{-2/7}$ due to the higher pressures in longer legged divertors. This prediction is tested by performing a scan in impurity fraction, and determining the location of the detachment front in each simulation in the scan. The detachment threshold is then determined by finding the control parameter(s) of the last attached simulation before the front moves completely off the target. However, since the true detachment threshold is actually between the last attached and first detached simulation, we associate an uncertainty in the threshold given by the difference in control parameters between these two simulations.

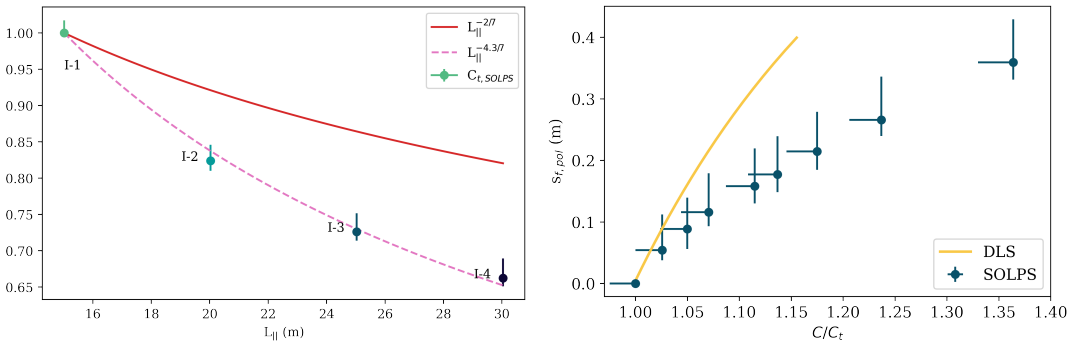

(a) (b)

FIGURE 3.6: a) The SOLPS-ITER-determined detachment thresholds, connection length to the power -2/7, and a best fit polynomial for the simulated detachment thresholds for each of the four grids, normalised to the value in case I-1. Parameters are plotted as a function of connection length. b) The detachment front position plotted against normalised control parameter for an impurity fraction simulation scan in grid I-2.

The detachment thresholds as a function of connection length for the grids in Figure 3.4 are plotted in Figure 3.6a. It is important to note that the thresholds are not absolute, but are normalised to the detachment threshold of grid I-1, since the primary use of the DLS model is for relative qualitative comparisons. From this figure, one can see the detachment threshold does decrease with longer connection lengths

in SOLPS-ITER simulations. However, the dependence is much stronger than DLS model predictions, being more akin to a $L^{-4/7}$ rather than $L^{-2/7}$, as can be seen from the polynomial fit in Figure 3.6a. The causes of this difference will be explored in Section 3.6. And as a result, doubling the divertor connection length leads to a 35% decrease in detachment threshold in these simulations, indicating modifying connection length could be a powerful tool for designing divertors around detachment.

3.2.3 Detachment Location Sensitivity

The connection length of a divertor, and the effective detached connection length $L_{||,f}$ (parallel length between the detachment front and upstream), can also have an impact on the location sensitivity of a detachment front. In fact, inspecting Equation 2.57, an increased detached connection length should decrease detachment sensitivity. In other words, as a detachment front is pushed away from the target, it becomes harder to push it further. Physically, this is due to the nonlinear decrease of pressure with detached connection length.

To test this prediction, an impurity fraction scan was performed on grid I-1 in Figure 3.4, and the detachment front location was determined for each simulation in the scan. The variation of detachment front location with normalised control parameter for this scan is shown in Figure 3.6b. From this figure, one can see a reduction in slope, corresponding to a reduction in detachment sensitivity, towards the end of the scan. In fact, the sensitivity from 0.25 to 0.35m is 2.1 times lower than from 0 to 0.1 m in the simulated data. This reduction is also seen in DLS predictions, which predict a factor 1.6 difference in sensitivity across the same regions.

Though both the SOLPS-ITER and DLS results show a reduction in sensitivity at the end of the scan, the two differ in the actual front movement. This is expected, since the DLS was formulated with many assumptions baked in, and it was never designed to be used for accurate quantitative predictions. Looking into *how* the two differ, the SOLPS-ITER results are significantly less sensitive than the DLS predictions. For a front to move 0.35m off the target, the DLS model predicts the control parameter must only increase 15% above its threshold value, but the SOLPS-ITER results show a required control parameter 37% higher than the threshold. In other words, the fronts in SOLPS-ITER are more resistant to changes in control parameter than the DLS model predicts. As will be seen later, this is a consistent outcome across many simulations, and the causes of it will be explored in section 3.6.

3.3 Poloidal Flux Expansion and X Divertors

Another effective way to optimise alternative divertors is to vary the poloidal field across a divertor. By reducing the poloidal field towards the targets, a poloidal flux expansion is introduced, defined as the ratio of poloidal pitch at the target and x-point, $F_\Theta = \frac{\Theta_X}{\Theta_t}$ [144]. This reduction in poloidal field can increase connection

lengths. However, investigations into connection length effects have been covered in the previous section. Here the effects specific to poloidal flux expansion are highlighted, and specifically the effect on detachment location sensitivity. Conclusions presented here may be relevant for configurations such as the X-divertor, Super-X divertor, Snowflake, and X-point target, which all leverage a reduction in the poloidal magnetic field strength along the divertor.

3.3.1 Detachment Location Sensitivity

According to Equation 2.58 of the DLS model, decreasing the poloidal pitch in a particular region of a divertor will decrease the sensitivity of a detachment front location in the poloidal plane. The reason for this is that the control parameter required for front movement is governed by physics in the parallel plane, according to Equation 2.57. Thus, all else being constant, a poloidally flared and non-flared divertor should have the same detachment front movement in the parallel direction. When this movement is mapped to the poloidal plane, however, there should be a difference in front movement, since the mapping from parallel to poloidal space is different for a poloidally flared geometry. As such, regions of poloidal flaring should have lower location sensitivity than comparable regions with higher poloidal field, according to Equation 2.58.

To test these predictions SOLPS-ITER simulations have been performed for a straightdown isolated divertor leg, and one which is poloidally flared near the target. The grids are shown in Figure 3.7a, with the poloidal field profile shown in Figure 3.7b. It is important to note that these geometries have identical physical baffling, and on the killer flux tube they have identical total flux expansions and connection lengths. The detachment front locations were determined for each simulation, and the movement of these fronts, with respect to control parameter variation, are shown in parallel and poloidal space in figures 3.8a and 3.8b respectively.

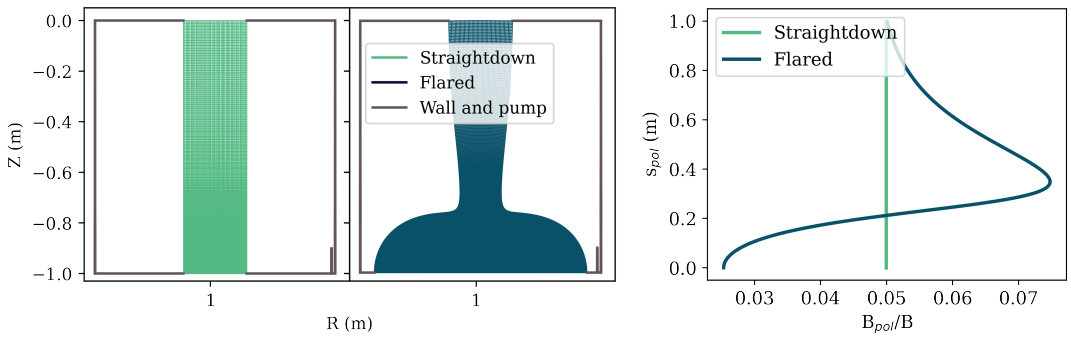

(a) (b)

FIGURE 3.7: a) The poloidal cross-sections of straight and poloidally flared vertical grids. b) The magnetic pitch profile for the separatrix of the grids in a).

From Figure 3.8b, a reduction in poloidal location sensitivity (figure slope) can clearly be seen in the flared region of the flared grid relative to the straightdown

geometry. In fact, the SOLPS-ITER results show a ≈ 2.6 times difference in sensitivity and the DLS model predicts a factor 2.1 difference in the first 0.1 m. Moreover, Figure 3.8a shows that this same movement is similar between the two grids when it is expressed in parallel space. This supports the idea that front movement is primarily governed by physics along a field line. Note that the SOLPS-ITER front positions do not move in exactly the same way in both grids in parallel space. However, this is most likely due to 2D effects, since these grids do not have identical properties (such as total flux expansion) on flux tubes which are not the killer flux tube.

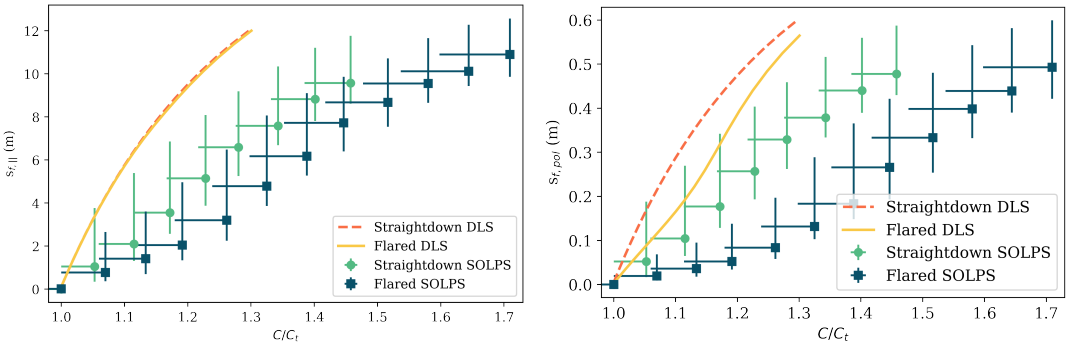

(a) (b)

FIGURE 3.8: The a) parallel and b) poloidal detachment front positions for the straight and flared grids in Figure 3.7a, plotted against the detachment control parameter normalised to the SOLPS-ITER-determined threshold. DLS location evolution profiles are indicated by the unbroken and dashed lines.

3.4 Total Flux Expansion and Super-X Divertors

One of the most powerful tools for alleviating target heat fluxes, particularly in spherical tokamaks, is modifying the total flux expansion of the divertor, $F_r = \frac{B_X}{B_t}$. This is typically done by having a target strike point at a much higher major radius than the x-point, as is the case in the Super-X divertor; but this could also be achieved with sufficient poloidal flux expansion from poloidal field coil shaping. An increase in total flux expansion will increase the parallel area of a given flux tube, and therefore decrease the local heat flux density along said flux tube. As a result, the two-point model predicts that configurations such as the Super-X should have lower peak target heat fluxes in attached conditions. Moreover, the DLS model predicts configurations with higher total flux expansions should be easier to detach than standard configurations.

To test the flux expansion effects predicted by simple modelling, four divertor legs with identical baffling and size have been generated, but are rotated with respect to the vertical from 0°to 90°. The grids, shown in Figure 3.9a, have the same x-point locations, but different target major radii. This leads to a reduction in the total magnetic field from the x-point to the target, as shown in Figure 3.9b. From

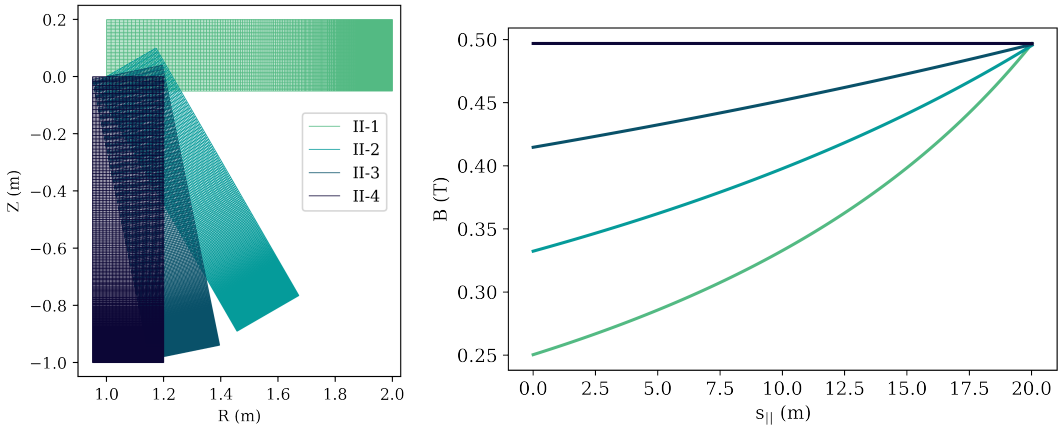

(a) (b)

FIGURE 3.9: a) The poloidal cross-sections of four box divertor grids at varying angles to the vertical. b) The total magnetic field profile along the separatrix of the grids in a).

grid II-4 to II-1, this leads to a doubling of the total flux expansion, as in these simple grids the total field is simply given by $\frac{B_X}{R}$.

3.4.1 Attached Target Conditions

To verify the scaling of target heat loads with flux expansion in the attached regime, attached simulations of the grids in Figure 3.9a were run, with identical boundary conditions $n_u = 1\text{E}19\ \text{m}^{-3}$, $q_{||,X} = 50\ \text{MWm}^{-2}$, $f_N = 0.1\%$. The target parallel heat flux densities, which are plotted in Figure 3.10a, follow a similar trend to reproduce the $\frac{B_t}{B_X}$ relationship predicted by the two-point model. However, the target heat flux in SOLPS-ITER decreases more strongly than predictions for an increase in total flux expansion. Similarly, the variation in target temperatures plotted in Figure 3.10b shows the expected decrease with increasing total flux expansion, but the variation is stronger in SOLPS-ITER.

This discrepancy between the two-point model and SOLPS-ITER is due to the fact that there are power losses along the SOL in these simulations, contrary to the assumptions of the conduction limited two-point model. Moreover, these losses become 30% stronger for grids with higher total flux expansions, as they move closer to detachment onset. Hence both the target temperatures and heat fluxes are reduced further than expected.

3.4.2 The Threshold of Detachment

For divertors leveraging total flux expansions, the DLS model predicts higher total flux expansions should lead to better access to detachment. This is because the local heat flux density that must be dissipated in order to detach is lower in divertors with higher total flux expansion. Another way to conceptualise this is that for a finite volume flux tube, the volume in the radiating region is increased. To confirm

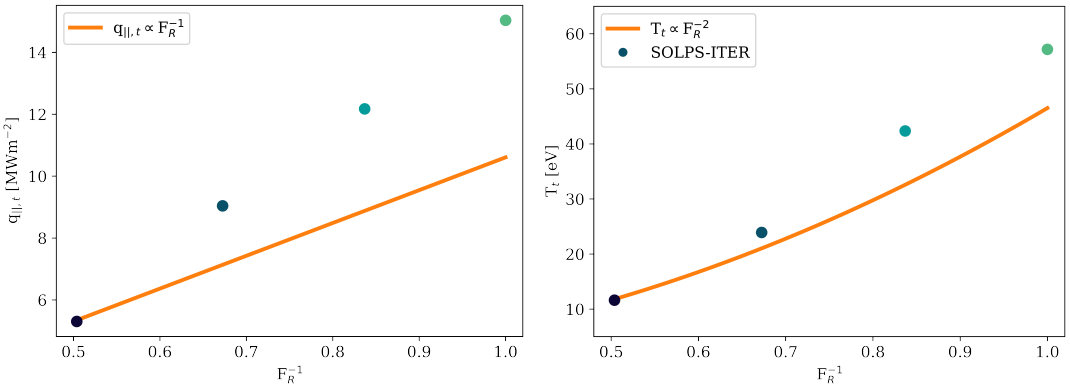

(a) (b)

FIGURE 3.10: The a) target heat flux densities and b) target electron temperatures on the 'killer' flux tubes of SOLPS-ITER simulations for the four grids in Figure 3.9a. Variations predicted by the two-point model are plotted as unbroken curves.

this, impurity fraction scans have been performed for the grids in Figure 3.9a, and the detachment threshold has been determined for each grid. The thresholds, plotted as a function of inverse flux expansion, are shown in Figure 3.11. According to the DLS model, the relationship between C_t and F_R^{-1} should be roughly linear, but slightly weaker due to the -2/7 dependence of threshold on divertor-averaged magnetic field.

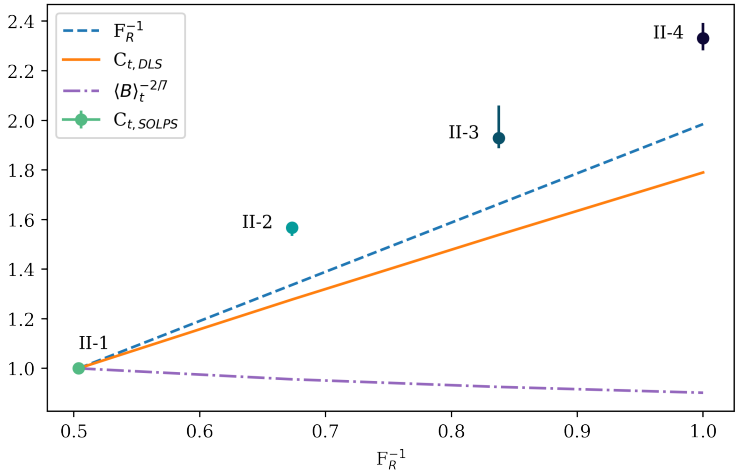

FIGURE 3.11: The SOLPS-ITER and DLS model detachment thresholds, total flux expansion to the power -1, and divertor-averaged magnetic field to the power -2/7 for each of the four grids in Figure 3.9a, normalised to the value in case II-1. Values are plotted as a function of the inverse of total flux expansion.

Inspecting Figure 3.11, SOLPS-ITER simulations show the same broad trend as the DLS predicted variation of thresholds, but the dependence of threshold on flux expansion is stronger in the simulations. Indeed, the DLS model predicts the threshold of grid II-4 should be a factor 1.75 higher than grid II-1, but the SOLPS-ITER

simulations show the threshold differs by 2.3. It is important to remember here that $C \propto \sqrt{f_\alpha}$. Hence, if the threshold control parameter is 2.3 times higher in grid II-4, the impurity concentration required to detach is more than 5 times higher.

3.4.3 Detachment Location Sensitivity

In addition to detachment threshold, the DLS model predicts that variation in magnetic field along a field line should strongly affect the sensitivity of detachment front movement. In particular, Equation 2.57 indicates that a higher total magnetic field gradient in a given location, $\frac{dB}{ds}$, should lead to a lower detachment location sensitivity in said region. To investigate this, the detachment front positions for the SOLPS-ITER impurity scans of grids II-1 and II-4 are plotted as a function of control parameter in Figure 3.12a. Here the control parameter is normalised to the detachment threshold of each grid, such that only the normalised sensitivities are compared, $\frac{1}{C}\frac{dC}{ds_{f,||}}$. The front position variation plotted as a function of absolute control parameter C is shown in Figure 3.12b.

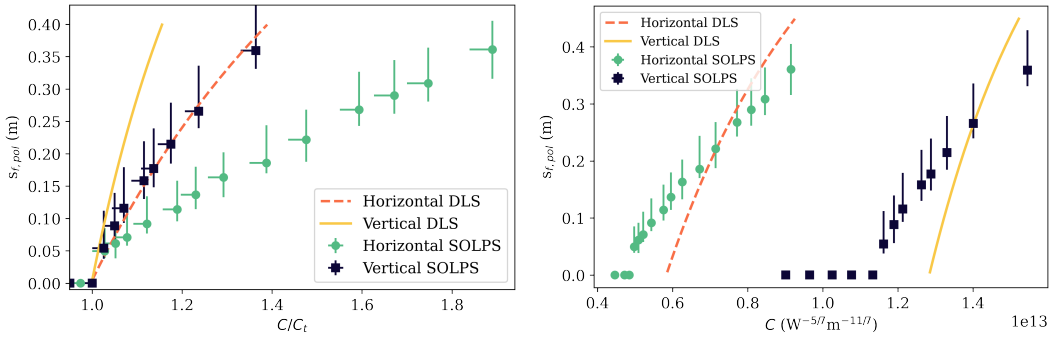

(a) (b)

FIGURE 3.12: a) The poloidal detachment front positions of grids II-1 (Horizontal) and II-4 (Vertical), plotted against the detachment control parameter, normalised to the SOLPS-ITER-determined threshold. The unbroken and dashed lines indicate the DLS predictions for each grid. b) Identical results to a), but plotted as a function of absolute control parameter C.

From Figure 3.12a, two conclusions are clear; first, both the DLS predictions and SOLPS-ITER simulations show the horizontal grid (II-1) is significantly less sensitive than the vertical grid, due to the presence of strong magnetic field gradients along the flux tube in case II-1. In fact, the difference in sensitivity between the two grids in the first 0.1m is well predicted by the model; the DLS model predicts a difference of a factor 2.5, and the SOLPS-ITER simulations show a difference of factor 2.4. Secondly, the DLS predicted and SOLPS-ITER front movement are not in perfect agreement, with simulations showing lower locations sensitivities than the DLS model predictions.

Upon first examination, Figure 3.12b seems to convey a much different story. Due to the lower detachment threshold in the horizontal grid, the absolute detachment location sensitivity appears similar in the horizontal and vertical cases. In fact the horizontal grid's sensitivity is slightly reduced, but this is not as apparent as in Figure 3.12a. However, one must be careful when making conclusions about absolute changes in control parameter. For example, even though the detachment thresholds of the two geometries are different, an experimentalist may leverage that difference to operate at a higher power, but with the same density in both geometries. Now when asking the question of how much does the upstream density need to increase by to move a detachment front 0.1m off the target, the change in absolute density is 2.6 times lower in the horizontal. In summary, changes in absolute control parameters depend upon the operating regime, and it is difficult to make general conclusions about these. For this reason the emphasis is placed upon the relative sensitivity, $\frac{1}{C}\frac{dC}{ds_{f,||}}$.

3.4.4 Detachment Stability

Finally, Equation 2.57 tells us that it should be theoretically possible to have a negative detachment sensitivity, given a sufficiently negative $\frac{dB_f}{ds_{f,||}}$ term. In other words, given a sufficient total flux contraction along a divertor - as is seen in horizontal inner leg divertors for example - there may be regions of negative location sensitivity.

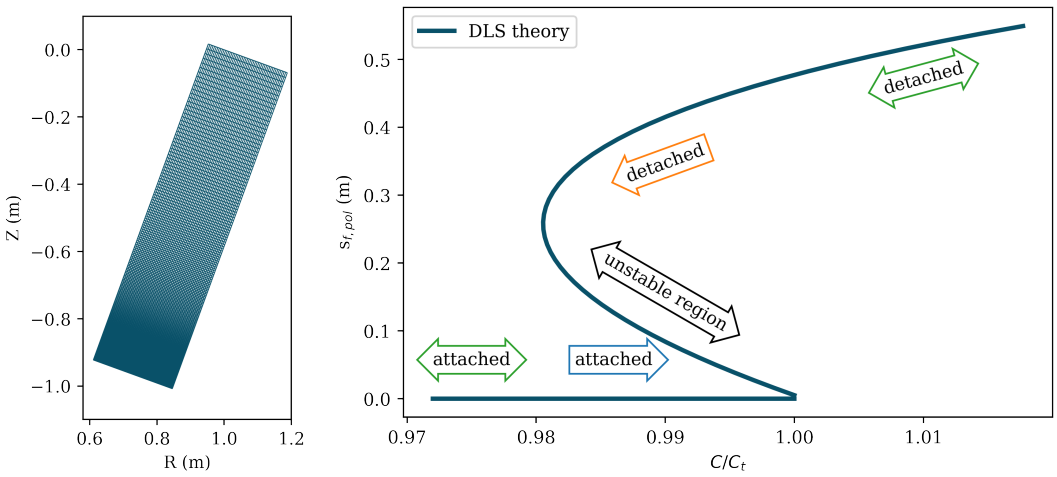

(a) (b)

FIGURE 3.13: a) A grid for a divertor leg at an angle of -10 °to the vertical. b) The detachment location evolution profile of the third SOL ring from the separatrix in a), calculated by the theoretical DLS equations. Green arrows indicate stable continuous regions, blue arrows indicate stable regimes only accessible from an attached state, orange arrows indicate stable regimes only accessible from a deeply detached state, and black arrows indicate unstable regions not accessible from either direction.

Yet what do such regions of negative sensitivity correspond to physically? To help understand this, the DLS model has been applied to a isolated divertor leg

at -10° to the vertical, shown in Figure 3.13a. The results of the DLS model are shown in Figure 3.13b. From this figure, regions of negative location sensitivity imply that it is 'easier' (one needs a lower C) to have a detachment front further away from the target, than more towards it. Thus, one may expect that when detachment fronts encounter such regions, they become unstable, and quickly move further and further upstream. They should stop only when they reach the next stable (positive location sensitivity) point which requires the same control parameter as the start of the unstable region. So in Figure 3.13b, as the divertor detaches at $C/C_t = 1$, the front should quickly jump past the unstable region and stop at $s_{f,pol} \approx 0.4$, the next location with $C/C_t = 1$.

Another interesting consequence of negative sensitivity is that when the divertor begins attached and detaches, it should immediately move past the unstable region, but also move past the region from 0.25m to 0.4m, which is stable with a positive sensitivity. There is no reason, however, that this area should be inaccessible if the divertor started very detached, and the control parameter was lowered. In this case, the control parameter can theoretically be lowered even below the detachment threshold, to $C = 0.98C_t$. If decreased further, the divertor would immediately reattach, as there are no valid detached solutions beyond this point. This presence of a bifurcated detached solution is another unique property of negative sensitivity geometries.

To verify these fascinating behaviours predicted for divertors with strong total flux contraction, two impurity fraction scans were performed for the divertor leg in Figure 3.13a. The first scan ('forward' scan) starts in an attached state and successively the impurity concentration is increased, whilst the second scan ('backwards' scan) begins in a deeply detached state and the impurity fraction is decreased. The measured front locations are plotted as a function of control parameter (normalised to the forward scan threshold) in Figure 3.14.

In Figure 3.14 one can see that both qualitative behaviours predicted by the DLS model are present in SOLPS-ITER simulations. Firstly, if the impurity concentration is increased marginally above its threshold value, the detachment front jumps more than 0.25m upstream. Secondly, if the divertor begins detached and the impurity concentration is decreased, it seems that detachment can still be maintained with a control parameter 8% lower than the 'forward' detachment threshold. In other words, for the same control parameters, two bifurcated solutions exist; one clearly attached, and one deeply detached.

These conclusions concerning divertors with strong total flux contraction may have important consequences for geometries such as inner divertor legs on spherical tokamaks. For example, if detachment can truly be accessed below the 'forward' detachment threshold, then it could be beneficial to detach the divertor early in a pulse, then decrease the seeding of impurities. Or, the divertor targets themselves could be modified to shorten the divertor leg, to avoid the presence of an unstable region entirely.

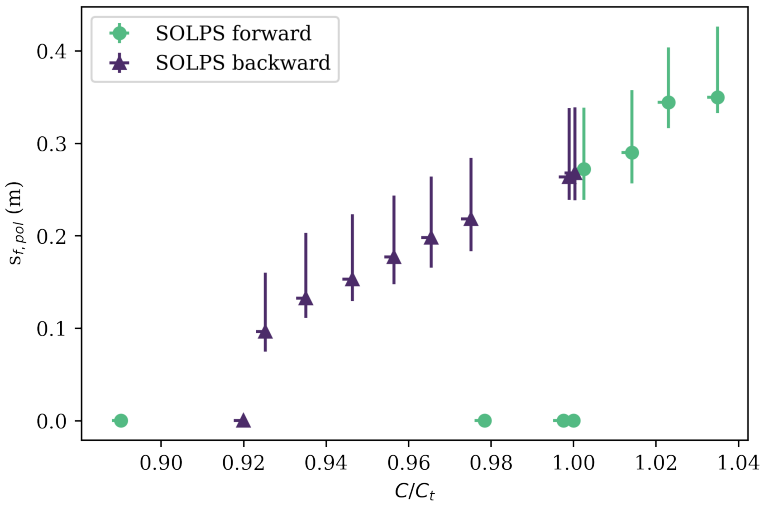

FIGURE 3.14: The detachment location evolution profile for the grid in Figure 3.13a, calculated from SOLPS-ITER data. The circular data points labelled 'SOLPS forward' are for an impurity fraction scan starting from an attached state and becoming more detached. The triangular data points labelled 'SOLPS backward' indicate an impurity fraction scan starting from a detached state and becoming less detached.

These results must be expressed with a few caveats. Firstly, the SOLPS-ITER simulations here lack a full geometry, drifts, and impurity transport, which all may modify detached solutions. Furthermore, the SOLPS-ITER simulations presented are steady state solutions, and do not describe how detachment truly evolves in time from one state to another. Finally, detachment bifurcations have been seen in previous models and experiments [145]–[147], where detachment fronts may oscillate between two significantly different solutions on the threshold of detachment. However, this is the first time cliff behaviour and detachment bifurcation has been shown to be explicitly caused by total magnetic flux contraction, since identical outer leg geometries in this study show no such behaviour. The verification of such specific predicted behaviour from the DLS model tends to support at least some physics principles of the model.

3.5 Averaged Magnetic Field and Pathing

According to the DLS model, the divertor averaged magnetic field is a contributing factor to the detachment threshold in a given divertor geometry. The model predicts that with the same target and x-point magnetic field, $C_t \propto \langle B \rangle_{abovet}^{-2/7}$. Thus divertors with high divertor-averaged magnetic fields should have a lower detachment threshold.

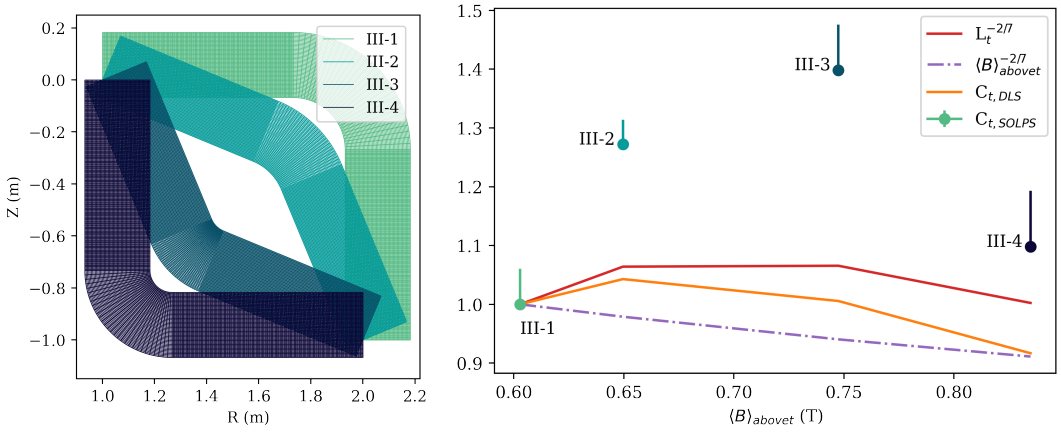

(a) (b)

FIGURE 3.15: a) The poloidal cross-sections of four kinked box divertor grids with various divertor shapes; all with the same B_x/B_t at the third SOL ring from the separatrix. b) The detachment threshold, connection length to the -2/7, averaged field to the -2/7, and the DLS predicted detachment threshold for each of the four grids, normalised to their values for case III-1. Values are plotted as a function of average divertor magnetic field strength.

To test this prediction, four divertor legs (shown in Figure 3.15a have been generated with identical total flux expansions on the flux-tube of interest, but with different paths from the x-point to the target. In grid III-4, for example, particles spend more time at a low major radius than they do in grid III-1. Consequently, the line-averaged magnetic field in III-4 is higher than III-1, and the averaged field in III-3 is higher than III-2. Impurity fraction simulation scans were performed for these four grids, and the threshold of detachment was determined for each. The corresponding variation in thresholds are shown in Figure 3.15b. Of course, it is clear to see that grids III-1 and III-2, for example, have different leg lengths as well as pathing. The difference between these grids should scale as $C_t \propto L_{||,f}^{-2/7} \langle B \rangle_{abovet}^{-2/7}$.

The variation of detachment thresholds in Figure 3.15b show a trend in opposition to DLS model predictions. Specifically, the DLS model predicts that grid III-4 should have a lower detachment threshold than III-1 by roughly 10%; however, the figure shows a detachment threshold roughly 10% higher in grid III-4. Similarly, grid III-3 has a higher threshold than III-2, which is contrary to DLS model predictions. Overall, this disagreement between the DLS model and SOLPS-ITER, in addition to the marginal differences between the grids, suggest that modifying pathing does not represent a strong or clear way of impacting detachment.

3.6 Missing Physics of Simple Models

Over the previous sections, SOLPS-ITER simulations have replicated some broad predicted trends of the DLS model. However, the actual variation in detachment thresholds, and detachment front location in SOLPS-ITER do not agree very well

with the DLS model. What is the cause of this disagreement? One may recall that in the formulation of the DLS model, several assumptions were made. In particular:

1. The impurity radiation in the divertor can be modelled by a fixed fraction of species α with cooling function L_α.
2. The parallel width of the thermal front is much smaller than the gradient length of the B field strength.
3. The electron static pressure above the cold end of the thermal front remains constant.
4. There are no sources or sinks of heat flux apart from impurity radiation, and the heat flux above the front is entirely electron conducted.
5. The electron conductivity does not vary along the divertor, and $\kappa_{e,0}$ is constant (i.e., there are no flux limiters).

Thus, if there is disagreement between SOLPS-ITER and the DLS model, it should be due to the breaking of one or more of these assumptions. Now assumption 1 is not broken in these simulations, a fixed fraction artificial impurity model is used. For the rest of the assumptions, three equations can be formulated that solve the same heat balance as the DLS model, but with various assumptions relaxed. For example, relaxing the assumption of a thin front gives:

$$\frac{n_u\sqrt{f_\alpha}}{q_{||,X}^{5/7}} = \frac{q_{||,X}^{2/7}}{T_u}\frac{1}{B_X}\left(2\kappa_{e0}\int_{T_f}^{T_u}\frac{L_\alpha(T)T^{1/2}}{B^2}dT\right)^{-1/2}. \tag{3.2}$$

Moreover, additionally relaxing the assumption of constant pressure above the thermal front gives:

$$\frac{n_u\sqrt{f_\alpha}}{q_{||,X}^{5/7}} = q_{||,X}^{2/7}n_u\frac{1}{B_X}\left(2\kappa_{e0}\int_{T_f}^{T_u}\frac{T^{5/2}n^2L_\alpha(T)}{B^2}dT\right)^{-1/2}. \tag{3.3}$$

Next, relaxing the assumption of a constant κ_{e0} (i.e., allowing for flux limiters) gives:

$$\frac{n_u\sqrt{f_\alpha}}{q_{||,X}^{5/7}} = q_{||,X}^{2/7}n_u\frac{1}{B_X}\left(\int_{s_{f,||}}^{s_X}\frac{2q_{||}n^2L_\alpha(T)}{B^2}ds\right)^{-1/2}. \tag{3.4}$$

Finally, relaxing the assumption of impurity dissipation being the dominant sink for electron conducted heat flux gives:

$$\frac{n_u\sqrt{f_\alpha}}{q_{||,X}^{5/7}} = q_{||,X}^{2/7}n_u\frac{1}{B_X}\left(\int_0^{s_X}\frac{2q_{||}n^2L_\alpha(T)}{B^2}+\frac{2q_{||}W_{other}}{B^2f_\alpha}ds\right)^{-1/2}, \tag{3.5}$$

where W_{other} is the sum of all other sources and sinks for electron conducted heat flux, including exchange with other heat flux channels like convection. With these

three equations, one can compute the predicted detachment control parameters for a given front position in SOLPS-ITER. The final equation is simply an expression for heat balance with no assumptions, and so if all the true sources from SOLPS-ITER are taken into account, this last equation should simply give the true control parameter in SOLPS-ITER. By comparing the control parameters predicted by these various models, the importance of the different assumptions in the disagreement between SOLPS-ITER and the DLS model should be revealed.

3.6.1 Connection Length Studies

To assess the importance of the DLS assumptions in the effect of connection length, Equations 3.2, 3.3, and 3.4 were applied to the detachment threshold simulations of the grids in Figure 3.4. The resultant control parameter variation is shown in Figure 3.16a. In this figure, it is clear to see going from the original DLS model and relaxing the assumption of a thin front by applying Equation 3.2 makes very little difference to results (curve labelled 'true front width'). Relaxing the assumption of constant electron pressure, however, leads to a significant difference, and brings the threshold calculations much closer to the SOLPS-ITER values (curve labelled 'true pressure variation'). Relaxing the assumption of non-impurity sources and sinks then leads to a measurable change (curve labelled 'true heat sources'). Overall, however, this figure shows that the assumption of constant pressure is the most important in causing the difference between SOLPS-ITER and DLS predictions for this study.

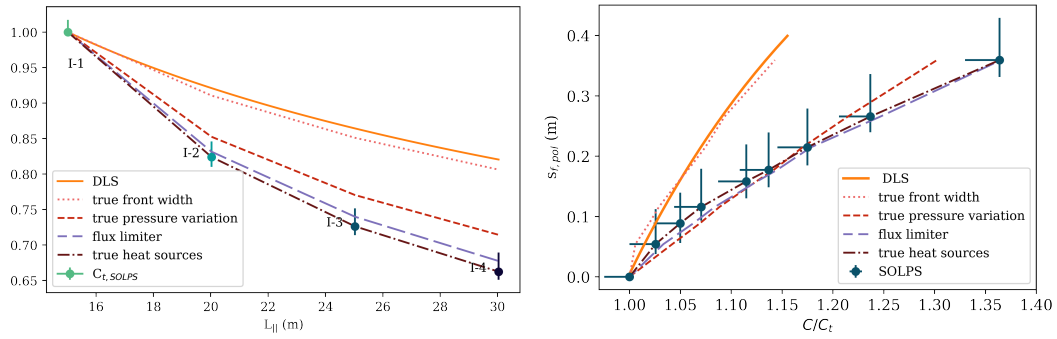

(a) (b)

FIGURE 3.16: a) The SOLPS-ITER and DLS detachment thresholds for grids I-1 to I-4, plotted as a function of connection length. The predictions from the relaxed versions of the DLS model are also shown. b) The detachment front position plotted as a function of control parameter for impurity-scan SOLPS-ITER simulations of grid I-2. The DLS determined detachment control parameter is overlaid, including the relaxed versions of the model.

Similarly, Equations 3.2 to 3.4 have been applied to a detachment scan of grid I-2, to understand what causes differences between SOLPS-ITER and the DLS model when it comes to detachment front movement and sensitivity. The application of these equations to this detachment scan is shown in Figure 3.16b. From this figure,

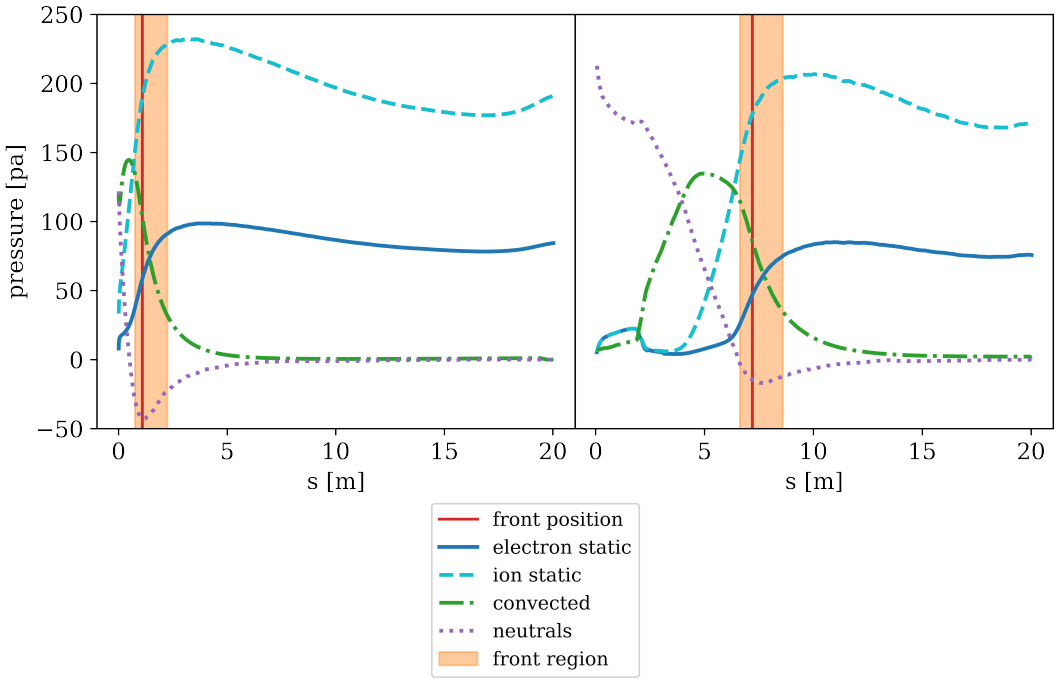

FIGURE 3.17: A decomposition of several important forms and sources of plasma pressure, plotted along the killer flux tube for detached (left) and deeply detached (right) SOLPS-ITER simulations of grid I-2.

one can again see that the relaxation of the constant pressure assumption leads to the most significant difference, and thus the variation in pressure is the primary cause for disagreement here.

To show the importance of pressure variation more clearly, the electron pressure is plotted along a field line for a barely detached and deeply detached simulation of grid I-2 in Figure 3.17. In this figure the detachment front region is indicated, and several key pressure balance quantities are also plotted, including the ion static pressure, convected pressure, and the plasma pressure sink due to neutrals (labelled 'neutrals'). Upon first glance, a reader may notice that the ion static pressure is quite high in these simulations compared to the electron static pressure. This is certainly true, and is a result of using a 50/50 split between electron and ion heat flux entering the top of the grid. In full-geometry simulations, one would expect this ratio to be more electron-dominated, due to the difference between electron and ion conductivities.

Figure 3.17 demonstrates several important points, including the fact that in the radiating region the electron static pressure is far from constant. In fact, though it remains reasonably constant upstream of the front region, inside the front region itself the electron static pressure drops more than 50%. This shows the DLS assumption of constant static electron pressure is broken. However, this figure also shows the assumption is not entirely unfounded, as the front region remains upstream of the region of total pressure loss. In fact, the electron static pressure loss in the front

region seems driven by an increase in convected momentum.

Figure 3.17 also indicates the electron static pressure in the front is subtly different between the barely detached and deeply detached simulations. In particular, there is a slight *source* of pressure from neutrals in the front region, and that source is larger in the more attached case. This reduced source in the more detached simulation partly explains why the location sensitivity in Figure 3.16b is reduced compared to DLS theory. As the front moves off the target, this source of pressure reduces, and the average electron static pressure in the front also reduces, decreasing radiation for a given upstream density and impurity fraction.

3.6.2 Flux Expansion Studies

The analysis of DLS model assumptions can be used to determine the dominant physics causing discrepancies between SOLPS-ITER and the DLS model when it comes to total flux expansion. Applying Equations 3.2 to 3.4 to the detachment threshold simulations of grids II-1 to II-4 produces the results shown in Figure 3.18a. From this figure, it is clear to see that the addition of other sinks of heat flux and the presence of a flux limiter leads to the largest difference.

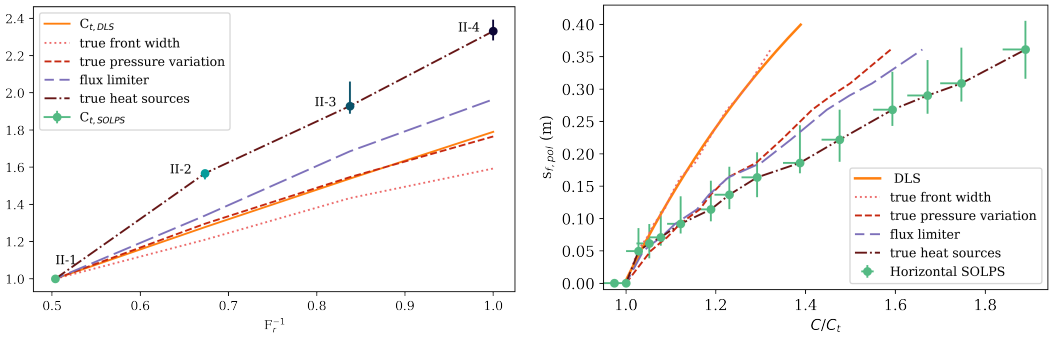

(a) (b)

FIGURE 3.18: a) The SOLPS-ITER and DLS detachment thresholds for grids II-1 to II-4, plotted as a function of inverse total flux expansion. The predictions from the relaxed versions of the DLS model are also shown. b) The detachment front position plotted as a function of control parameter for impurity-scan SOLPS-ITER simulations of grid II-1. The DLS determined detachment control parameter is overlaid, including the relaxed versions of the model.

To demonstrate this strong effect of energy sinks, the electron conducted heat flux, and several key power sinks are plotted as a function of parallel distance along the killer flux tube, and this is shown in Figure 3.19. Comparing the detachment threshold vertical leg (top left) against the horizontal leg (top right) simulations, the total impurity power losses are much (nearly 2x) lower in the horizontal case at the same upstream density. One may assume this is due to the lowering of heat flux densities due to total flux expansion, but remember this effects the heat flux per unit area; the DLS model assumes the total dissipated power in Watts is the same. Because the requirement for impurity dissipation is lower in the horizontal

leg, the detachment threshold is even lower than DLS predictions. The reason for this lower requirement on impurity losses can be attributed to the increase in losses from deuterium, which is expected given the larger volume for radiation. More surprisingly, there is also a significantly stronger sink from radial transport.

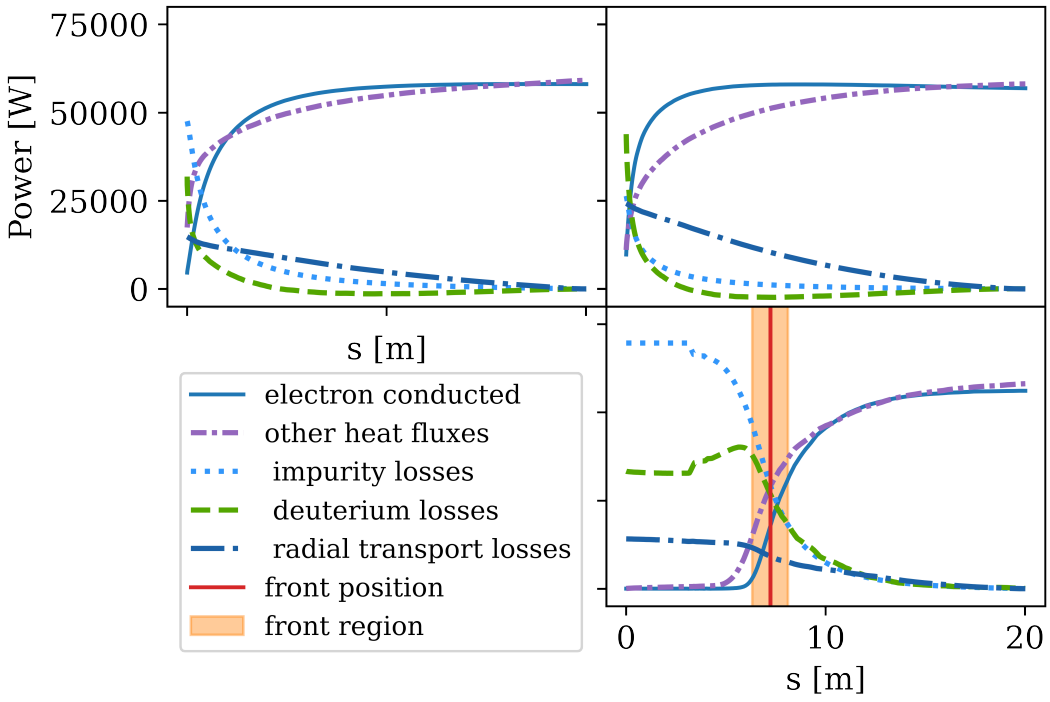

FIGURE 3.19: The electron conducted heat, and other fluxes of heat, in addition to the cumulative power sinks from deuterium, radial transport, and impurities, plotted as a function of parallel distance from the target. The data used for the plots are from SOLPS-ITER simulations of the threshold case for a vertical grid (top left), the threshold case for horizontal grid (top right), and a deeply detached case for a horizontal grid (bottom right).

In addition to threshold variation, the relaxed versions of the DLS model can be used to analyse discrepancies in detachment location sensitivity results in grids with high total flux expansion. Indeed, Equations 3.2 to 3.4 have been applied to an impurity fraction scan for grid II-1. The results, shown in Figure 3.18b, indicate that the assumption of no flux limiters and no non-impurity sinks is a significant cause of disagreement.

Delving into the role of heat sinks, one can examine the electron conducted heat flux profile and several key power sinks for a deeply detached simulation of grid II-1 in Figure 3.19 (bottom right). Comparing this to the simulation on the threshold of detachment (top left), the deeply detached simulation radiates more than 2.5x more power through impurity radiation. This increased requirement on impurities as the detachment front moves further off the target aids in explaining why the detachment sensitivity in SOLPS-ITER in this grid is significantly lower than expected.

This increased requirement on impurity radiation seems driven by the fact that

more power is lost overall in the deeply detached simulation. Additionally, there are also slight reductions in radial transport and deuterium power sinks in this more detached simulation. The radial transport reduction in particular is quite intuitive and expected. In Figure 3.19, the radial transport in the detached simulation effectively stops downstream of the detachment front. Thus, the effective length over which these radial transport losses are active is reduced. One would similarly expect radial transport in any configuration to reduce as divertors become more deeply detached.

3.6.3 Pathing Studies

Finally, in previous sections there were significant deviations between the DLS model and SOLPS-ITER when it came to the effect of pathing and divertor-averaged magnetic field. As such, to determine the source of this discrepancy, Equations 3.2 to 3.4 were applied to the threshold simulations of grids III-1 to III-4. The resultant detachment thresholds, determined with various relaxed assumptions, are shown in Figure 3.20. From this figure, it seems that the assumption of a thin width, constant pressure, and impurity-dominated losses of electron conduction all play a roughly equal role in the deviation between the DLS model and SOLPS-ITER.

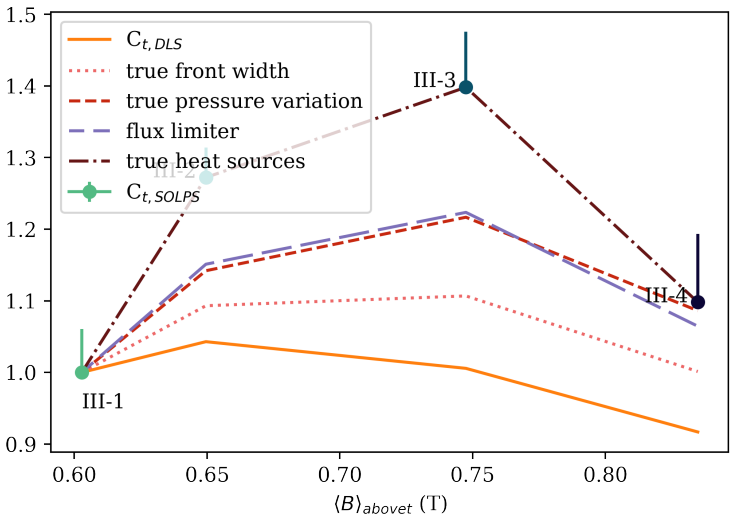

FIGURE 3.20: a) The SOLPS-ITER and DLS detachment thresholds for grids III-1 to III-4, plotted as a function of divertor averaged magnetic field. The predictions from the relaxed versions of the DLS model are also shown.

In general, analysing the sources of discrepancy between the DLS model and SOLPS-ITER simulations, several conclusions can be drawn. Firstly, it seems the assumption of a thin thermal front generally holds true in the SOLPS-ITER simulations presented. The breaking of this assumption plays a very small role in any discrepancies between the simulations and the DLS model. In many cases presented, the variation in pressure seems to contribute significantly to deviations between the DLS model and SOLPS-ITER simulations. Though the assumption of total pressure conservation seems reasonable, in the front region a great deal of momentum

is transferred from the static to dynamic pressure, and there are small momentum sources from neutrals.

3.6.4 The Impact of Different Control Parameters

Throughout this chapter detachment access and sensitivity has been studied with regards to changes in impurity fraction. An important question is how would these results and conclusions change if a different controller - such as upstream density or heat flux - were leveraged. Though the entire study has not been repeated with all three control parameters, several particular scans were. In particular, the impurity scan in the horizontal divertor leg has been repeated, but instead using a density scan (with fixed $q_{||,X}$ = 50 MWm^{-2} and f_α = 1.7), and a heat flux scan (with fixed n_u = 1×10^{19} m^{-3}). The front movement from these three scans is shown in Figure 3.21.

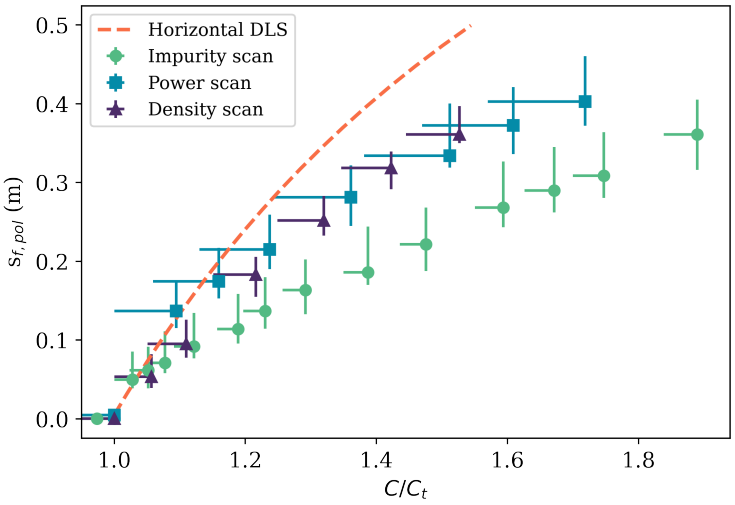

FIGURE 3.21: a) The poloidal location of detachment fronts, plotted as a function of control parameter variation for grid II-1. The three different SOLPS-ITER scans represent scans using impurity fraction, power, and density as control parameters. Also shown is the DLS predicted profile.

Figure 3.21 first and foremost shows that the effects of n_u, $\sqrt{f_\alpha}$, and $q_{||,X}^{-5/7}$, are indeed not equivalent in SOLPS-ITER simulations. Specifically, the detachment location sensitivity of the impurity fraction scan is measurably lower than that of the density and power scans. Consequently, the higher location sensitivity (or smaller detachment window) results of density and power are much closer to the DLS predictions. This is an important point, and indicates that the disagreement between SOLPS-ITER and the DLS model presented earlier may have been less pronounced if density or power were used as detachment controllers. Indeed when density scan detachment studies have been performed previously, better matching has been found with theory [143].

3.7 Summary

In this chapter, more than one hundred simulations have been performed in SOLPS-ITER for the purposes of validating simplified models. In isolated leg simulations of various lengths and magnetic field profiles, detachment was accessed and controlled by varying the fixed-fraction of an artificial nitrogen impurity. The movement of the detachment front in these simulations is compared to predictions from the DLS model, and though the broad shape of the profiles is similar, front movement in SOLPS-ITER simulations is consistently less sensitive than the DLS model. In general, the SOLPS-ITER simulations show a location sensitivity 2-3 times lower than DLS predictions.

Put simply, the difference in impurity fraction required to push the front from one location to another is always larger in simulations than DLS predictions. Put even more simply, as more complex physics is introduced, detachment fronts become more resistant to changes in the plasma. As will be seen in Chapter 5, this is a consistent finding across different avenues of study, and is important to keep in mind. The main causes of difference between SOLPS-ITER and the DLS model are the presence of electron static pressure sources and sinks, and non-impurity power losses. Specifically, it has been shown that the electron pressure can change significantly in the front region, primarily due to exchange with convected momentum, and pressure sources from neutrals. In terms of power balance, the strength of radial transport and deuterium losses can vary significantly with geometry and regime.

Instead of using the DLS model to simply predict front movement in a single geometry, this work illustrates that the real strength of the DLS model is predicting how detachment control differs *between geometries*. When comparing the DLS-predicted variation in detachment access, SOLPS-ITER simulations confirm the non-linear decrease in detachment threshold with connection length, and the roughly linear increase in detachment threshold with target magnetic field strength. The variation in the threshold between grids is consistently stronger than DLS predictions.

One of the most novel outcomes of this work is verifying how detachment location sensitivity varies between geometries. In particular, the simple DLS model predicts that detachment fronts should become less sensitive to changes in controllers as they move further from the target; a prediction verified by SOLPS-ITER simulations. Additionally, the DLS model predicts the presence of strong gradients in the total magnetic field along a divertor should lead to less sensitive front movement of detachment fronts with respect to variation in impurity fuelling. Indeed, SOLPS-ITER simulations show a reduction of factor 2.4 in location sensitivity in a horizontal divertor leg with a strong gradient in the magnetic field, agreeing well with the DLS prediction of a factor 2.5 difference. The DLS model also predicts that a reduction in the poloidal magnetic field should reduce the sensitivity of the poloidal location detachment fronts, whilst not significantly affecting the movement in the direction

parallel to the magnetic field. SOLPS-ITER simulations have confirmed this effect, with a poloidal flared grid showing a reduction in poloidal location sensitivity of 2.6 compared with a straight grid. In good agreement, the DLS model predicted a 2.1 difference in sensitivity for this case.

The DLS model even predicts the presence of unstable regions in inner leg divertors caused by magnetic field gradients, which allows for bifurcation in detached and attached solutions for the same control parameters. SOLPS-ITER simulations of increasing and decreasing impurity seeding scans confirm the presence of such regions in an inner divertor leg at -10 °to the vertical. The confirmation of such specific behaviour predicted by the DLS model seems to support the underlying physics of the model.

Overall, the work contained in this chapter has validated the idea that reduced models can be used to predict and understand the differences between alternative divertor geometries. However, the comparative simulations used in this work are still relatively simple isolated divertor legs, designed to focus in on one magnetic feature of a divertor at a time. More complex simulations of real machines, and comparisons to experiment are required to completely understand the difference between simple intuition and the governing physics of real divertors.

Chapter 4

Simulating the Impact of Divertor Baffling

In Chapter 3, simple models and predictions of alternative divertors were tested using SOLPS-ITER simulations of divertor legs in idealised geometry. By implementing such simple geometries, these simulations are able to put certain alternative divertor features under the microscope, studying each feature in isolation. Using such simple geometries, however, means that some crucial physics pertaining to the true 2D structure of a tokamak may be lost. Consequently, in this chapter more intricate simulations are performed, using real tokamak geometries.

Specifically, this chapter centres around the impacts of divertor baffling - which refers to the shape of the physical material surrounding the divertor. Baffling is a feature which is fundamentally difficult to model simply, as it impacts the 2D transport of neutral hydrogen and impurities throughout the entire tokamak chamber. As such, this chapter features SOLPS-ITER simulations of full MAST-U divertor geometries. In keeping with the purpose of this thesis of studying alternative divertor features in isolation, the geometries used implement extreme cases of baffling with no changes to the magnetic geometry. Moreover, the impacts of baffling solely on a hydrogenic plasma are explored, and the impact of impurities is neglected.

In this chapter it is found that the tightly baffled simulations tend to access detachment easier than the open baffled geometries. The tightly baffled configurations also seem to have higher upstream temperatures and heat fluxes than the open cases, which may be an important impact to keep in mind for pedestal stability. However, the simulations here show these differences between geometry reduce going from low to high power, which indicates research into baffling on low-power devices may not be very applicable to reactors. The conclusions contained within this chapter may have consequences for configurations such as the tightly baffled, long-legged divertor [107], [108].

4.1 Simulation Setup

Apart from the magnetic structure of the plasma, the other important aspect of divertor design is the baffling and shape of physical structures surrounding the divertor

plasma. Of course, this feature differs from magnetic characteristics in that simple analytical models often have very little intuition to offer. After all, effects of baffling are complex and fundamentally two dimensional. Nevertheless, one may begin to understand qualitatively what effects the physical baffling of a divertor may have on plasma performance and detachment by performing simple code experiments.

Such an experiment has been carried out, by performing SOLPS-ITER simulations of a symmetric double null MAST-U Super-X divertor. The simulations have boundary conditions for fixed density and heat flux at the core, with no external sources of gas puffing. The decision was made to fuel the plasma entirely from the core to keep the study simple and reactor relevant, since pellet fuelling in the core will be a dominant source of fuelling in reactor-class tokamaks. A radial profile of anomalous transport coefficients is implemented, with weaker radial transport in the SOL compared to the core. The coefficients were chosen to replicate midplane profiles from experimental campaigns in MAST-U, and are held constant across all simulations contained in this chapter.

To investigate the impacts of baffling, the same equilibrium is simulated with two very different surrounding physical structures. The first, shown on the left in Figure 4.1, has an extremely open geometry, and any neutrals recycled from the target are free to move around the entire chamber. The second, shown in the same figure on the right, is extremely tightly baffled around the divertor leg. Both geometries have the same plasma facing component material (100% recycling tungsten), and implement the same vertically symmetric divertor pumping system with a pumping fraction of 10%.

As part of this study, a scan in core density has been performed for both geometries, ranging from attached to deeply detached simulations. This density scan was repeated at three input powers: 3MW, 6MW, and 12MW. An artificial nitrogen impurity model was used with the cooling curve in Figure 3.2 with an impurity fraction fixed at 3%. It is important to emphasise this is an artificial impurity, since one proposed benefit of baffling is how it should modify impurity transport, keeping impurities seeded in the divertor confined in the divertor region. The study here neglects this effect, and instead attempts to isolate the other potential impacts of baffling.

4.2 Detachment Access and Power Balance

One important way in which divertor baffling may impact divertor performance is through detachment access. To investigate this, the location of detachment was calculated for each simulation in the density scans for each geometry and power level. For this study the location of detachment is defined as the point at which T=5 eV on the killer flux tube, which is the third SOL ring into the SOL. This detachment front position is plotted as a function of midplane density on the killer flux tube, shown in Figure 4.2.

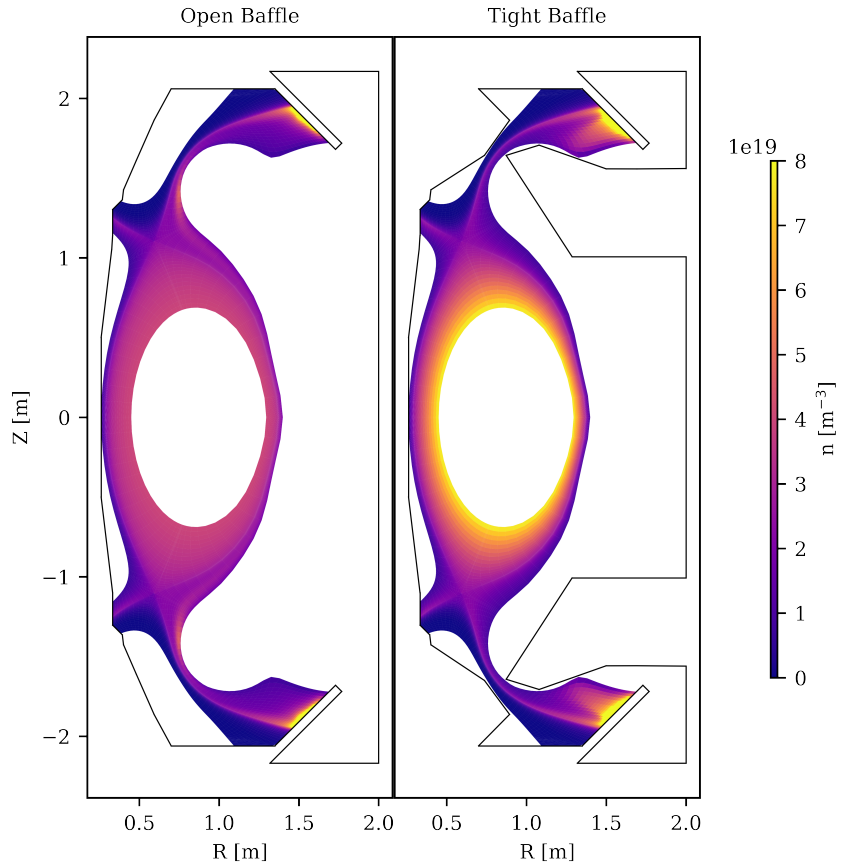

FIGURE 4.1: A 2D plot of the electron density for SOLPS-ITER simulations of an open (left) and tightly baffled (right) MAST-U Super-X divertor with 12MW input power at the threshold of detachment.

From Figure 4.2, one can see a measurable difference between the tightly baffled and open baffled cases. Specifically, at 3MW the open case detaches at a density 91 % higher than the tight case, where detachment here is defined as the last simulation with a target temperature over 5 eV. This lower threshold required for the tight configuration is present at the higher powers, though the effect is reduced. At 6MW, the difference in threshold density is 52 %, and at 12MW the difference is 8%. In general, this seems to indicate that easier detachment access can be a benefit of tightly baffled divertors, but a benefit which may not necessarily scale to reactor-like powers.

To investigate why the tightly baffled case detaches more easily than the open case, the power balance of the simulations can be examined. The sinks of total plasma power in the simulation domain are decomposed by type, including the neutral sink, nitrogen radiation, and loss to plasma facing components. This decomposition of sinks is shown for the threshold simulations at all 3 powers for the tight and open geometries in Figure 4.3a.

From Figure 4.3a, one can see that the power sinks in the tight and open baffled geometries are remarkably similar. At all three power levels, neutral losses account for roughly 30% of power dissipation, and impurities account for roughly 50%. The

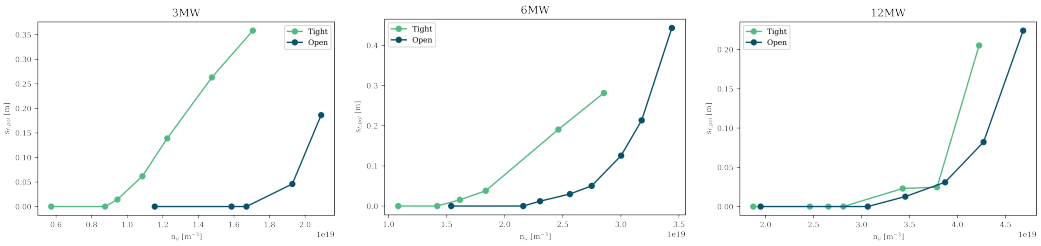

(a) (b) (c)

FIGURE 4.2: The detachment front location on the lower outer divertor, plotted as a function of outer midplane density on the killer flux tube for SOLPS-ITER simulations of a tightly baffled, and open baffled MAST-U divertor.

only exception is 12MW, where the tight case has reduced nitrogen radiation and increased heat flux to plasma facing components. This similarity in dissipation mechanisms is interesting, given that at 3MW the upstream density is 2 times lower in the tight simulation. The fact that the tight case is able to have the same strength of power sinks at a lower density begins to explain why it is able to access detachment more easily.

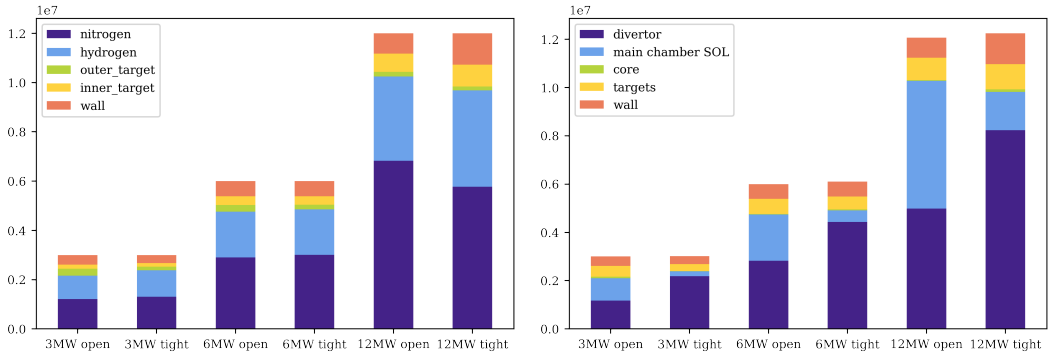

(a) (b)

FIGURE 4.3: The balance of total plasma power for the threshold of detachment simulations at three different input powers, for an open and tightly baffled geometry. a) Shows the balance of power decomposed by sink type, and b) shows the power loss decomposed by region.

The simulations can also be analysed in terms of *where* the power is being dissipated. For the six threshold of detachment simulations, the total plasma power sink is separated into the power leaving the grid towards the walls and targets, and the volumetric dissipation in three regions: the core (inside the separatrix), the SOL (outside the separatrix and upstream of the x-points), and the divertor (the regions downstream of each x-point). This decomposition of heat sink by location is shown in Figure 4.3b. From this figure, a clear distinction can be seen between the tight and open geometries in terms of location of power dissipation. In the 3MW case, there is 10 times more radiation in the divertor than SOL, in the 6MW there is 9 times more, and at 12MW there is 7 times more. The significantly reduced upstream power loss

seems characteristic of the tightly baffled geometry, and may be a key reason why some dissipation mechanisms are strong in this geometry despite the lower density required for detachment.

Inspecting Figure 4.3a there is another interesting trend concerning power balance. For the open geometry, the power incident on the outer targets at 3MW outweighs that incident on the inner targets. However, at 12 MW, this relationship reverses, and the power incident on the inner target is much greater than the other. This implies the communication between the inner and outer divertors evolves with power, and at high powers it seems the outer divertor detaches before the inner.

4.3 Neutral Transport and Power Dissipation

Noting the analysis of power balance between threshold simulations, one may ask how in the 3MW simulations, the tight case is able to dissipate the same amount of power through neutrals, with roughly half the density? As indicated by the analysis of power balance by region, it seems one of the most telling differences between the two grids is the amount of dissipation occurring in the main chamber. One would expect this is partly because neutrals can escape the divertor more easily in the open case and are ionised more upstream.

To show this explicitly, the divertor neutral trapping of the simulations can be calculated. This trapping is defined as the ratio of total ionisation rate to the total neutral recycled flux from the target. Here the ionisation is summed radially, then the cumulative poloidal sum of this ionisation is calculated for each successive poloidal grid away from the target. So, if the neutral trapping is 1 at a certain poloidal location, that means 100 % of the recycled neutrals have been ionised by that point. Comparative plots of this neutral trapping are shown in Figure 4.4 for 3MW and 12MW at the threshold of detachment.

From these figures a stark difference in neutral trapping between geometries can be seen. Unsurprisingly, the open geometry, in which recycled neutrals may leave the divertor more freely, shows barely 50% of recycled neutrals are ionised in the lower outer divertor region. In contrast, the tight geometry shows that nearly 100% of recycled neutrals are ionised in the divertor, which is consistent with the geometry making it harder for neutrals to escape. As a result of this difference in trapping, the neutral density upstream is much lower compared to that of the divertor region. This can be seen in the neutral density plots at 3MW and 12MW; shown in Figures 4.5, and 4.6 respectively.

The fact that neutrals are much more trapped in the divertor in the tight geometry explains a few outcomes of power balance. First, this helps describe why most of the power loss occurs in the divertor region in the tight case, since most of the ionisation is occurring in the divertor, and the neutral density here is much higher than upstream, leading to more neutral losses.

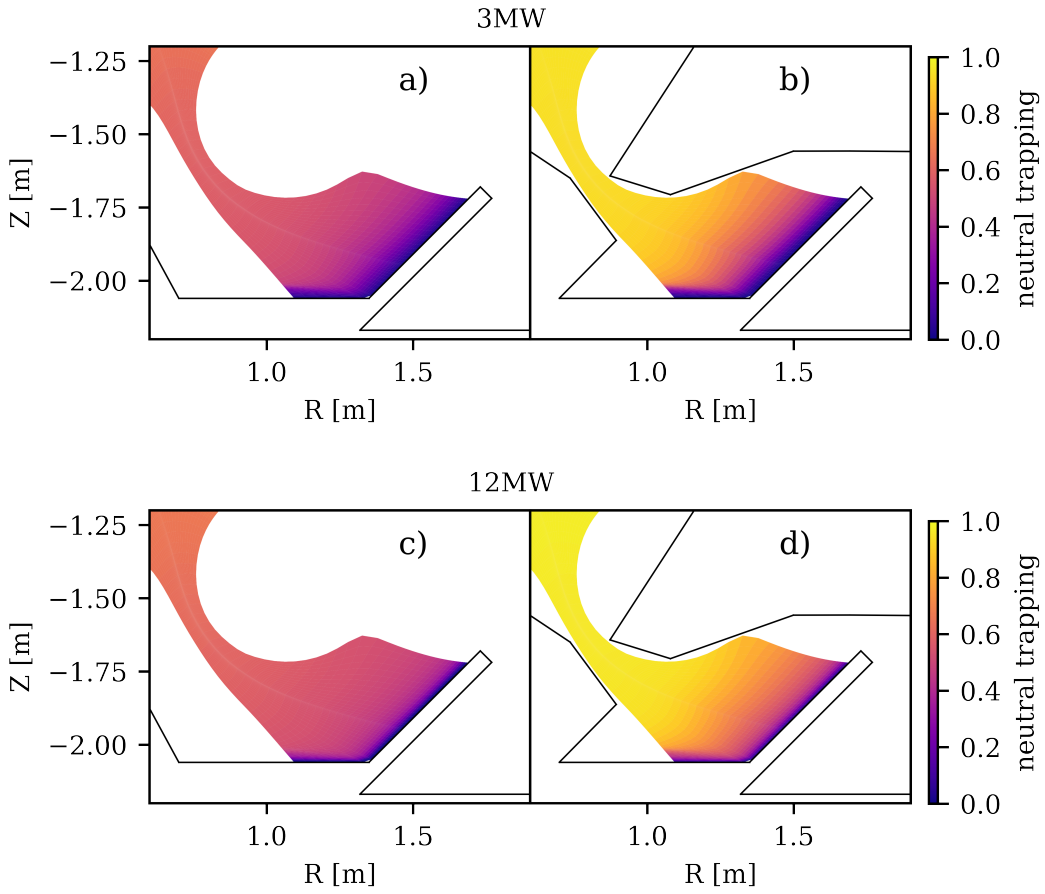

FIGURE 4.4: The neutral trapping plotted along poloidal steps of the plasma grid for SOLPS-ITER detachment threshold simulations of open (a and c) and tight (b and d) baffled geometries. Trapping here is defined as the radially summed, then cumulative poloidal sum of the ionisation particle source, divided by the total neutral recycling rate from the target. a) and b) are at 3MW input power, and c) and d) are at 12MW input power.

Differences in trapping also help explain why the same neutral losses can be achieved at a lower density in tight geometry. Ionisation near the target pushes the tightly baffled geometry into a very high recycling regime, as most recycled particles are ionised quickly and directed back towards the targets. Thus, for a given input particle source, there is significantly more ionisation in the tight case. Or for the same total ionisation rate, the tight case may operate with a lower density upstream. This is indeed the case, since at 3MW, the total ionisation rate is 1.14 $\times 10^{23}$ s^{-1} in the open case and 1.16 $\times 10^{23}$ s^{-1} in the tight case at the threshold of detachment.

Another interesting impact of this difference in trapping is how the two geometries are fuelled. Because a great deal of ionisation from recycling occurs upstream in the open geometry, it is fuelled quite effectively by the recycled particle flux. As such, the open geometry needs significantly less fuelling from the core to reach similar separatrix densities. A consequence of this is that the core density is much flatter in the open case relative to the tightly baffled case, as can be seen in the 2D electron

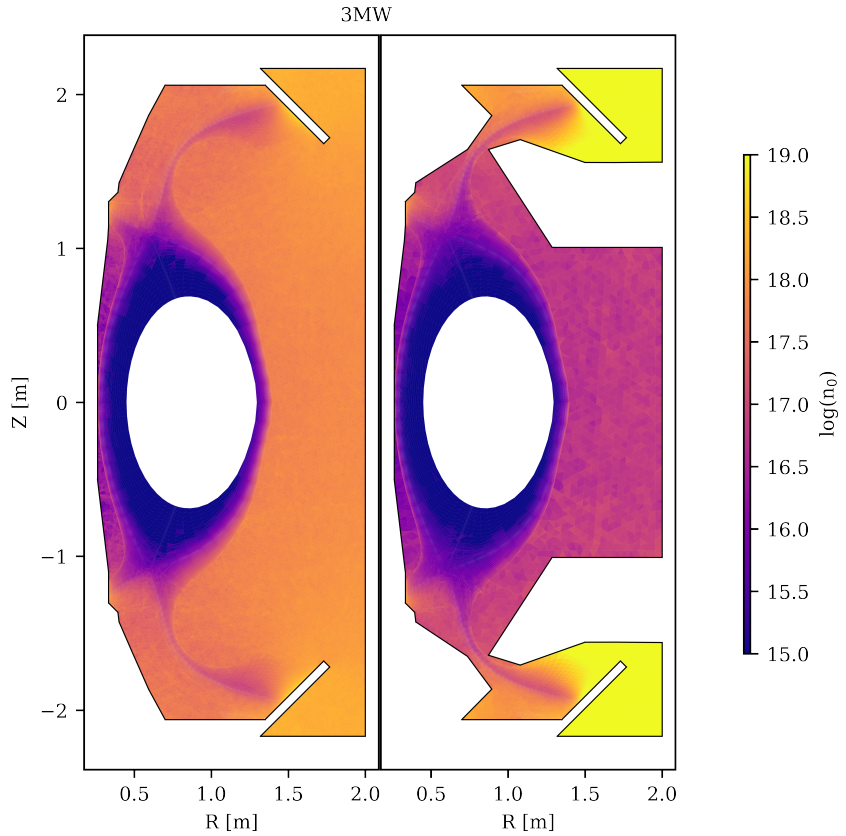

FIGURE 4.5: A poloidal plot of the logarithm of total deuterium neutral density for SOLPS-ITER simulations of an open (left) and tightly baffled (right) MAST-U Super-X divertor with 3MW input power at the threshold of detachment.

density profiles in Figure 4.1.

These trapping and neutral density figures also show interesting trends in terms of how neutral transport varies with power. In particular, Figure 4.4 also shows the neutral trapping is slightly higher in the tight case at 12MW compared with 3MW. This is expected, since the higher temperature, higher density plasma more easily ionises incident neutrals, and acts as more effective plug or baffle. In a similar manner, the trapping in the open case is also raised at 12MW. However, this is perhaps not as significantly as one may think, given that neutrals should be very quickly ionised in this high density, high power (200 MWm^{-2} peak parallel heat flux) plasma.

In fact, Figure 4.6 shows that - due to the angle of the MAST-U outer targets -recycled neutrals may enter the low-field side chamber relatively easily, as they do not have to cross a significant area of plasma. This allows the low-field main chamber to fill with neutral gas. As expected, the plasma does act more like a baffle at high powers, and this low-field side neutral gas cannot cross to the high-field side easily. As a result, Figure 4.6 shows a significant asymmetry in neutral density on the inner and outer sides of the chamber. This may partly explain why there is a change in inner-outer target communication in the open case at higher power discussed in

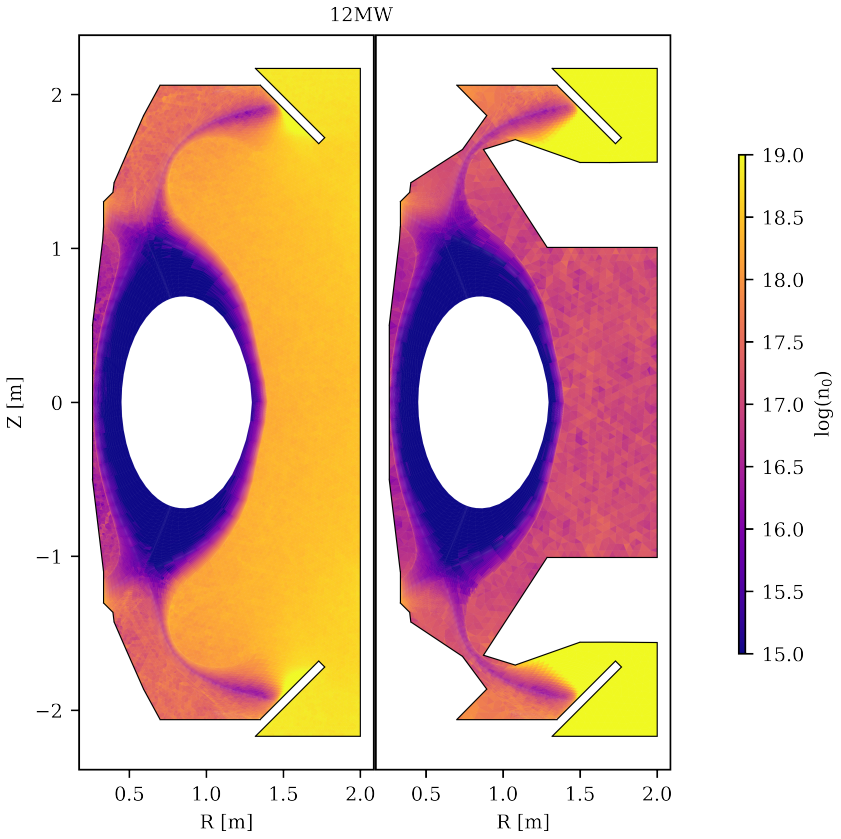

FIGURE 4.6: A poloidal plot of the logarithm of total deuterium neutral density for SOLPS-ITER simulations of an open (left) and tightly baffled (right) MAST-U Super-X divertor with 12MW input power at the threshold of detachment.

the previous section.

4.4 Nitrogen Power Dissipation

One important outcome of power balance analysis was that (particularly at low power), the tightly baffled divertor is able to achieve similar levels of nitrogen radiation than the open geometry, but with roughly half the midplane density at the threshold of detachment. Since a simple artificial radiation model is used, it is relatively straightforward to assess what may be different between the two geometries. There are two likely causes for the increased nitrogen radiation in the low power tight simulations. Either this increase is caused by a difference in where the radiation is occurring (and thus how much total volume is available for radiation) or a difference in pressure for the same density. This first point is particularly important given that the equilibrium is a Super-X, which leverages high total flux expansions and thus expanded volumes near the target.

To assess the volume available for radiation, the radiation-averaged magnetic field can be calculated for simulations at the threshold of detachment. At 3MW, this nitrogen radiation averaged magnetic field is 0.36 T for the tight geometry and 0.43

T for the open geometry. This means the effective magnetic field strength in the radiating region is higher in the open case, and thus the average volume used for radiation is 20% lower. This 20% difference in effective volume partially explains why the tight case is able to detach more easily.

To assess the difference in effective pressure, the electron temperature profiles have been plotted as a function of parallel distance from the upper outer divertor targets on the 'killer' SOL ring at the threshold of detachment. The results for all three powers are shown in Figure 4.7, and indicate that the upstream temperatures in the tight geometry are consistently higher than the open geometry. In fact, at 3MW the tight case has a 40% higher temperature than the open. Though, much like the variation in detachment access, the difference in temperatures drops to 24% at 6MW and 14% at 12MW. This higher temperature leads to higher pressures for the same density, and this partially explains why the tightly baffled grids are able to achieve the same amount of nitrogen radiation at a lower density.

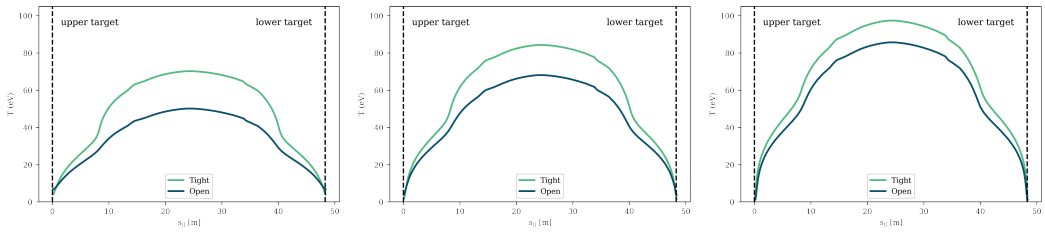

(a) (b) (c)

FIGURE 4.7: The electron temperature profiles along the killer flux tube for the detachment threshold SOLPS-ITER simulations of a tightly baffled and open baffled MAST-U geometry, at a) 3MW, b) 6MW, and c) 12MW input powers.

The fact that the upstream temperatures differ between open and tight geometries imply that the heat flux profiles in physical space also differ. To investigate this, the parallel heat flux density profiles at the divertor entrance (x-point) have been plotted for the threshold simulations for both geometries, at all 3 input powers. These plots in Figure 4.8 show the peak heat flux entering the divertor in the open geometry is roughly half that entering the tight geometry at 3MW. This difference is primarily caused by the increased power losses in the region upstream of the x-point in the open geometry. Consistent with the variation in upstream temperature and detachment access, the difference between the peak heat fluxes reduces at high power. The main reason for this change in relative heat fluxes is the variation in heat flux widths with power. As input power increases, the heat flux width of the open case decreases whilst that of the tight geometry increases.

This difference in heat flux alone, however, is insufficient to completely explain the difference in upstream temperature. After all, in these simulations at the threshold of detachment, one would expect $T_u \propto q_{||,X}^{2/7}$. Using this relation, a factor 2 reduction in the peak heat flux at 3MW should not cause the factor 2 reduction in T_u that is observed. One may think that perhaps the average *electron conducted* heat flux

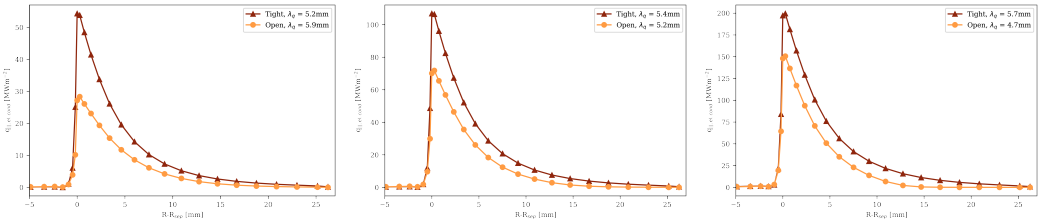

(a) (b) (c)

FIGURE 4.8: The parallel heat flux density profile at the lower outer divertor entrance, plotted as a function of radial distance from the separatrix mapped to the midplane. The heat flux profiles are for tightly and open baffled geometries at a) 3MW, b) 6MW, and c) 12MW of input power.

along the entire flux tube changes more significantly. However, this is not the case as the line integrated electron conducted heat flux only changes by a factor ≈2. This implies that the effective electron conductivity also varies between the geometries. Indeed, a flux limiter is implemented in these simulations. However, such a flux limiter is an approximation for varying collisionalities, and the flux limit applied is fairly arbitrary. As such, it is not wise to draw any conclusions about the physical implications of this conductivity variation.

These higher temperatures for a similar level of detachment are not only optimal for achieving good detachment thresholds, but can also impact the height and shape of the pedestal. Though in general a high pedestal temperature is desirable for performance, it may also adversely impact the pressure gradients across the pedestal, degrading pedestal stability [148].

When discussing the conclusions from this simple baffle experiment, one must keep in mind these simulations neglect one of the most important predicted impacts of baffling: impurity transport. The simulations presented here have a fixed-fraction model for impurities, where the concentration is the same at all locations. In reality, baffling is predicted to have a significant impact on impurity transport, and tightly baffled divertors are thought to compress impurities more in the divertor chamber. It is also important to recall that these simulations have fixed core density boundary conditions. As such, the plasma is fuelled entirely from the core and recycling. One would expect these results could change significantly with an external puff. Finally, remember that this comparison was performed with the same pumping fraction, but not the same total pumping rate. It would certainly be interesting to see this comparison repeated with the same total pumping rate.

4.5 Summary

Over the course of this chapter, real-geometry simulations of the MAST-U divertor have been performed. In particular, SOLPS-ITER simulations have been performed with a tightly baffled MAST-U Super-X divertor with high neutral trapping, and

compared against a more open divertor with less neutral trapping. It is found that the more tightly baffled divertor may access detachment easier, at lower upstream densities. By comparing simulations on the threshold of detachment, the differences in profiles and power balance can be assessed.

One stark difference between geometries is that ionisation and power loss occur mostly in the divertor in the tightly baffled case, whereas power loss occurs along the entire SOL in the open geometry. Baffling also impacts the transport of neutrals, and the greater fraction of ionisation in the divertor occurring in the tightly baffled geometry leads to more neutral losses for the same density, and leads to higher gradients in the core density profile. At higher power, the communication between the inner and outer legs of the open geometry seems reduced, due to the plasma acting as baffling for neutrals in different sections of the chamber.

Another key difference in geometries is an enhancement of nitrogen radiation and upstream temperatures with tight baffling. This enhancement of nitrogen radiation is partly because radiation occurs more near the targets in the tightly baffled geometry. In the Super-X configuration this divertor radiation occurs in regions of low magnetic field, where there is more volume available for radiation. Moreover, because the majority of power loss occurs downstream in the tightly baffled geometry, the upstream heat flux tends to be higher, and this leads to higher upstream temperatures. These two effects mean the tightly baffled divertor can access detachment more easily.

One curious conclusion from this simulated baffling study is that the benefits of a tightly baffled divertor seem to reduce at higher power. Specifically, the upstream temperature at higher power is more similar between tightly and open baffled geometries than it is at lower powers. This leads to more modest nitrogen radiation, and thus a reduced difference in detachment threshold. This conclusion could be important when considering tightly baffled divertor designs for tokamak reactors. However, it must be emphasised that the study here does not feature true impurity transport, which is expected to be affected significantly by divertor closure.

Chapter 5

Comparison of Detachment Modelling to Alternative Divertor Experiments

Over the previous chapters, various models for alternative divertors have been introduced, and simulations have been performed to study the physics of alternative divertors and detachment. However, even the most sophisticated models incorporate assumptions and numerical approximations, and will never perfectly represent reality. For the most substantial understanding of the underlying physics, these models must be compared to experiment.

Over the following chapter, detachment front movement is experimentally measured and analysed from experiments performed on the MAST-U tokamak. This front movement is compared to predictions made by the DLS model, and the experimental front movement is found to be consistently less sensitive than DLS model predictions.

Some qualitative predictions made by the DLS model are compared against the experimental movement of detachment fronts, including the effects of changing divertor configuration on location sensitivity, and the dominating influence of the plasma upstream of the detachment front. Though the DLS model is not expected to work well in the regime of these experiments, there is evidence to suggest broad predictions made by the model agree with experiment.

Despite the positive outlook, significant further study is required, analysing larger sets of data across campaigns in MAST-U, and comparing results to other devices. However, this work makes a useful step forward in the physical understanding of detachment control in experiment, which could be used to optimise design choices and control algorithms for future devices.

5.1 The MAST-U Device and Diagnostics

The focus of this chapter is the study of experimental detachment front movement, and the comparison of such movement to DLS theory. In order to achieve these goals, a specific set of experimental data is required. In particular, such a study

requires experiments from a machine which can operate with alternative divertors in a range of detached states. For this investigation the MAST-U tokamak is used, which is one of the most capable machines when it comes to detachment studies and alternative divertors [112].

Additionally, to compare against the DLS model, two sets of experimental data are required. The first is an accurate measurement of the detachment front location. To this end, the Multi-Wavelength Imaging (Section 5.1.2) and Divertor Monitoring Spectroscopy systems (Section 5.1.3) are used. Secondly, a measurement of the variation in detachment control parameters (density, power, and impurity fraction) is required. For the experiments in question, density is the primary varied controller. As such the midplane Thomson (Section 5.1.4) and interferometry (Section 5.1.5) diagnostics are used for midplane density measurements.

5.1.1 The MAST-U Experimental Campaign

The scope of this study focuses on the second campaign of MAST-U, MU02, and in particular the RT22-07 EUROfusion work package experiments. These shots were run for the purposes of physics understanding of alternative divertors, as a risk mitigation strategy for DEMO. As part of these experiments, the device was operated with a deuterium plasma in L-mode, a plasma current of 750 KA, and an input power of 1.5 MW. The shots consisted of divertor configurations including a conventional configuration, an Elongated Conventional Divertor (ECD), and a Super-X Divertor (SXD); all vertically symmetric, roughly connected double nulls.

Though there are many more detached experiments in MAST-U, and in particular in the first campaign of MAST-U, MU01, only a handful of shots from MU02 were chosen for this study. The choice to omit shots from the first campaign are twofold; first, MU01 experiments were operated at a lower power, meaning the DLS model is less applicable. Moreover, the low plasma densities needed to achieve more attached scenarios led to locked modes in the plasma. As a result, the splitting of the plasma strike point was observed [110], [149], which makes detachment tracking difficult. In MU02, strike point splitting was significantly reduced.

5.1.2 The Multi-Wavelength Imaging System

When investigating detachment evolution in experiment, it is of primary importance to detect and track the location of a detachment front reliably. In MAST-U, one of the most effective ways to do this is through the Multi-Wavelength Imaging diagnostic (MWI). This diagnostic is a tangentially-viewing camera with 11 different filtered imaging channels, and a maximum acquisition frequency of 400Hz [149]–[151]. Cameras 1 to 10 have filters from 380 - 950nm, whilst camera 11 is reserved for coherence imaging spectroscopy [152].

Of the filtered imaging channels in the MWI, the primary channel for detachment tracking is camera 9, which filters the deuterium Fulcher band, located at $\approx$

600nm [110]. This Fulcher band corresponds to excitation emission from deuterium molecules. Since the molecules need sufficient energy for excitation, but not so much as to cause complete dissociation, Fulcher emission is typically strong only within a small range of plasma temperatures. Hence, Fulcher emission can be a powerful way to track low temperature locations corresponding to the location of detachment [110].

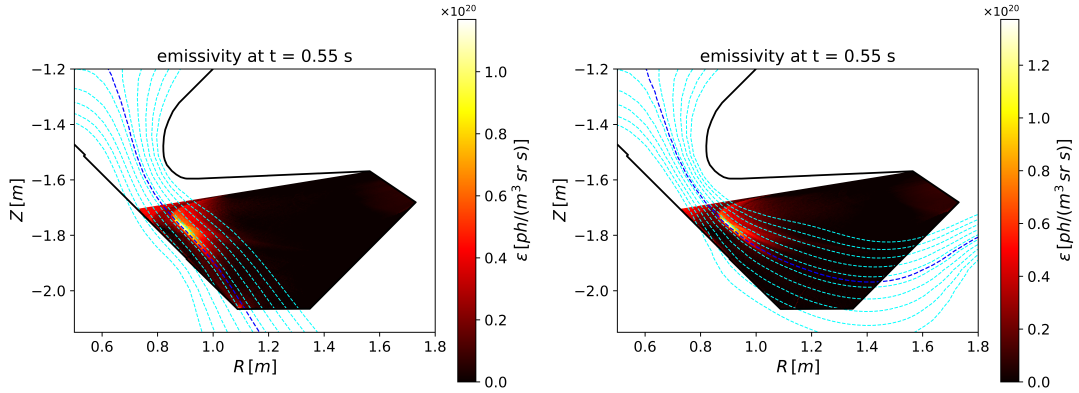

(a) (b)

FIGURE 5.1: The inverted emissivity profile from the MWI diagnostic in MAST-U, at t=0.55s for shots a) 47079 (elongated conventional configuration) and b) 46860 (Super-X configuration).

Because the MWI does not view poloidally, the image data must be inverted to determine the poloidal emission profile of the plasma. Such inverted profiles for an elongated conventional shot and a Super-X shot are shown in Figures 5.1a and 5.1b. Using this inverted profile, combined with equilibrium data from the equilibrium fitting (EFIT) code, one may construct an emission profile along a SOL ring, an example of which is shown in Figure 5.2. Here this profile is integrated between normalised flux surfaces of $\psi = 0.97$ to $\psi = 1.1$, so as to not place too much importance on the emissivity of one radial location.

After obtaining a profile of integrated emissivity along a SOL ring, the peak of the emission can then be determined. This maximum strongly correlates with a temperature of roughly 4 eV [110]. Though this peak could be chosen as a definition of a detachment front, the point corresponding to a fall-off in this emission is chosen instead, which marks the trailing edge of detachment at lower temperatures. Values used for this study include the 50% fall-off and 20% fall-off, corresponding to 2.4 and 2 eV respectively.

Though the MWI is an incredibly effective tool to study detachment, it is not without its limitations. In particular, though the MWI can technically view up to the nose of the MAST-U baffle, the inversion becomes highly uncertain in this region. Additionally, certain inversion artifacts can form, such as the apparent bending of the emissivity profile towards the underside of the baffle in Figure 5.1b. This means that data close to the divertor entrance may not be very accurate, and indeed, when the MWI is compared to the divertor monitoring spectroscopy for the same time, the

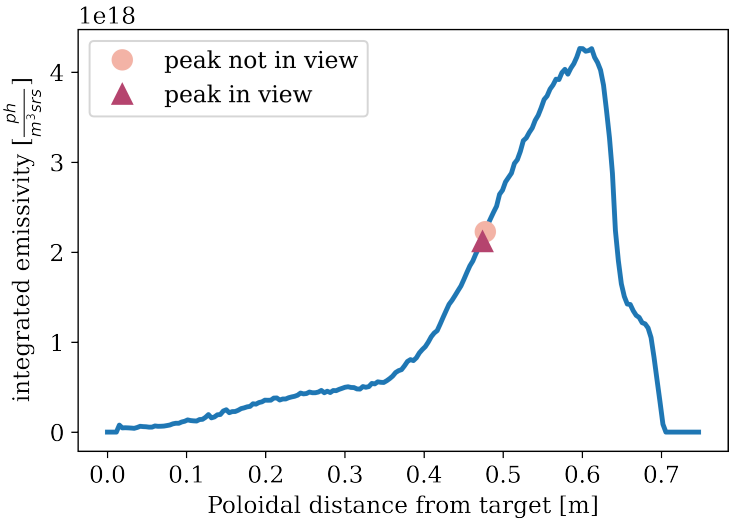

FIGURE 5.2: The inverted MWI emissivity plotted as a function of distance along the separatrix, integrated cross-field between $\psi = 0.97$ and $\psi = 1.1$. The profile is from shot 46860 at t=0.55s. The 50 % drop in Fulcher emissivity is marked, calculated assuming the peak in emissivity is in the MWI range (peak in view), and assuming the true peak has moved out of view, and a constant peak value is chosen instead (peak not in view).

data upstream for the MWI seems inaccurate. Such a comparison is shown in Figure 5.4, and from this figure one can see a drop in emission from the MWI after the 17th line of sight, which is not measured by the spectroscopy.

Because the validity of the MWI is uncertain near the divertor entrance, and because the peak in emission often occurs near the divertor entrance, there is consequently a significant uncertainty around the true peak in emission used for the front tracking. To help quantify this, two methods of front tracking for the MWI are used. The first method assumes the peak in the MWI range for a given time is the true peak. The second method assumes the peak is beyond the range of the MWI, and instead takes the peak in emission to be a constant value throughout the shot, independent of the peak measured at a specific time. In this method, the constant peak is simply the average peak throughout all times; for shot 47079 this value is 5.89×10^{18} $\frac{ph}{m^3 srs}$ and for shot 46860 this value is 4.51×10^{18} $\frac{ph}{m^3 srs}$. The front position and uncertainty are then given by the average and standard deviation of these two methods. An example of the front location determined by these two methods is shown in Figure 5.2.

5.1.3 The Divertor Monitoring Spectroscopy System

In addition to the MWI, another useful diagnostic to study detachment front movement is the Divertor Monitoring Spectroscopy (DMS) system. This diagnostic is composed of two spectrometers, observing different spectral ranges, from high-n hydrogenic Balmer lines at 365nm, to the D_2 Fulcher band at 600nm [110]. Each

spectrometer system has 20 different fibers, whose lines of sight spread across two fans covering the entire lower divertor chamber, as shown in Figure 5.3.

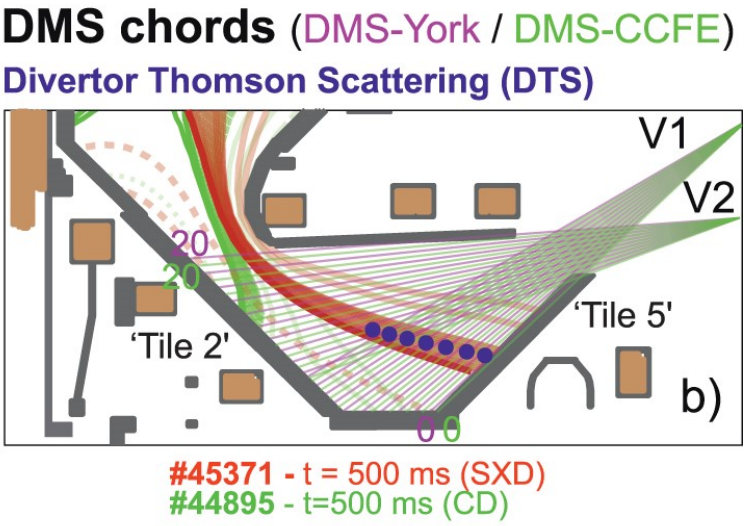

FIGURE 5.3: The lines of sight of the MAST-U DMS diagnostic. Adapted from [110].

To track the location of detachment using the DMS, one can employ a similar method to front tracking with the MWI. Specifically, the Fulcher emission from each line of sight can be calculated. Then, by finding the intersection between a given line of sight (LOS) and the separatrix at a given time, the emission for each LOS can be associated with a position along the separatrix. The profile of emission along the separatrix can be analysed to find the peak, and then the 50 and 20% fall-off in this peak can be found through interpolation of the emission profile. The DMS views throughout the entire divertor, and since the raw data does not require inversion, the data is likely to be more accurate than that of the inverted MWI. For every shot analysed, the peak of the DMS emission always occurred within the viewing range, so there was no uncertainty associated in the peak location.

Despite its low uncertainties in emission profiles, the DMS also has its associated disadvantages. In particular, the spatial resolution of the emission profile is much worse than the MWI, since the DMS only has 20 lines of sight. Moreover, the DMS was operated with an acquisition frequency of 70 Hz, which means significantly less data for a given shot than the MWI. The DMS data is also associated with a line of sight, not a location in the divertor plasma. For this study, the DMS data can be associated with a location by finding the intersection between the line of sight and plasma separatrix. However, each line of sight will inevitably have integrated emission from other areas of the plasma.

Finally, upon analysing the DMS data for MU02 it was found that the lines of sight were misaligned. This was determined by integrating the MWI emissivity across the DMS lines of sight for shot 46860 at t=0.54s. This gives a synthetic DMS

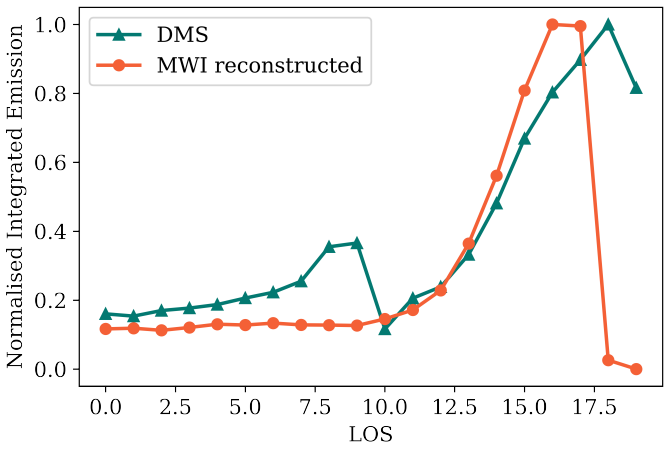

FIGURE 5.4: The integrated emission from the DMS diagnostic, plotted as a function of line of sight (labelled 'DMS'), for shot at 46860 t=0.54s. Also shown is the emission from the MWI, integrated along the DMS lines of sight. Values are plotted normalised to the peak in the profiles. If both diagnostics are correctly calibrated and are completely accurate, they should show the same profile.

profile from the MWI data, which can be used to determine the validity of both diagnostics, since if both are flawless the profiles should be identical.

Comparing this synthetic profile against the true DMS data in Figure 5.4, it is clear there is significant disagreement both at high and low lines of sight. The disagreement at high LOS numbers (at the divertor entrance) is most likely due to the MWI, as covered in the previous section. At low lines of sight, however, and in particular the sharp change in emission around LOS 10, suggests an error in the DMS. In particular, the drop in emission at LOS 10 seems to indicate there is more overlap between the two fibre sets than expected, and hence the lower 10 fibres are likely misaligned. Because of this, only fibres 10 to 20 will be used for the analysis.

5.1.4 Midplane Thomson Scattering

To properly study detachment evolution in experiment, one must measure detachment control parameters in addition to tracking detachment fronts. In the shots used for this study, plasma fuelling is the main varying controller, since input power is roughly fixed and intrinsic carbon radiation did not dominate power balance. Consequently, accurately determining midplane density is crucial for studying detachment evolution.

One useful diagnostic for measuring upstream density is the midplane Thomson system [153], [154]. Thomson scattering is a common plasma diagnostic which measures plasma density and temperature by recording the scattering and Doppler shift of laser light incident on a plasma. The midplane Thomson scattering system in MAST-U consists of eight Nd:YAG lasers with a sampling rate of $\approx$ 180Hz. The

light is collected and split across 130 fibre bundles [154]. The light from these fibres can then be analysed to produce a radial profile of electron density at the midplane.

Given a radial profile of electron density, one may assume the best way to define upstream density is simply the electron density at the major radius corresponding to the separatrix. However, it is important to remember that the separatrix location used for this analysis is from an EFIT code, which reconstructs the magnetic profiles using magnetic diagnostics [155]. This process, however, has significant uncertainties associated with it, and the location of the separatrix should not be taken as completely accurate. Because of this, the midplane density is not taken at exactly the separatrix, but is instead averaged from 4cm to 7cm inside the separatrix.

5.1.5 The Midplane Interferometry System

Interferometry is another diagnostic technique that can be used to estimate the detachment controller of upstream density. Interferometry allows properties of a plasma medium to be studied by measuring the interference of two or more beams of coherent light. The path difference between light travelling through a vacuum and through a plasma is proportional to the refractive index and length of the medium. Since the refractive index is proportional to density, the path length difference scales with the line integrated density of the plasma. This is the principle by which interferometry can measure the line-integrated density of a tokamak plasma.

The interferometry system in MAST-U consists of a CO_2 and a HeNe laser interferometer [156]. These two-colour systems are used to distinguish interference due to the plasma density, and due to vibration of the optical instruments themselves. The beam line is at the plasma midplane and is tangent to the central column at a distance of 0.3m. The uncertainty in density measurements for this diagnostic are 1E18 m^{-3}, and the temporal resolution is 4MHz [156].

Knowing the approximate width of the plasma through equilibrium reconstruction, the line-integrated density measurements from interferometry can be converted into a line-averaged density of the plasma, $\langle n \rangle$. Though this value is not a control variable in detachment models, the variation in line-averaged density likely scales with separatrix midplane density, which is a parameter in the DLS model.

5.2 Comparison of Front Movement

5.2.1 DLS Predictions

Using the diagnostics and analysis tools covered in the previous section, experimental front movement from MAST-U can be compared to the DLS model. Before comparing, however, it is paramount to ask how valid this comparison is, and what specific predictions should be tested. In terms of validity, the DLS model is not expected to model the shots used for this study well. This is because initial simulation and experimental analysis has shown that MU02 experiments are low power, and

dominated primarily by hydrogenic radiation along the entire divertor. In other words, the assumptions of impurity-dominated power balance, and a thin thermal front in the DLS model are broken in this regime.

Despite the non-ideal regime presented by the MAST-U experiments, there is still a wealth of interesting physics that may come from a comparison to the DLS model. In particular, the aim of this study is to determine whether there is any underlying physics of the DLS model that holds true despite the significant difference in regimes. In fact, one would expect many of the underlying physical processes of the DLS model to appear in experiment. For example, no matter what the regime in question is, moving a front further away from a target should lower the upstream temperature (and hence pressure for the same density). Similarly, in regions of high magnetic field gradient, detachment fronts may see stronger gradients in instantaneous heat flux density along a field line.

Consequently, though the following comparison is not ideal, it is still useful for extracting broad, underlying physics principles, if there are any. Though this investigation is by no means all-encompassing or precise, it is an effective step in the nascent topic of physical processes governing detachment front movement. The simplest comparison to start with is simply examining the measured front movement as density is ramped.

5.2.2 Experimental Comparison

Using the DMS and MWI diagnostics, the detachment front locations for shots 47079 and 46860 have been determined using the 50% fall-off in Fulcher emission towards the target. These shots are density ramps with the same input powers and plasma currents, but with 47079 operating with an elongated conventional divertor (ECD) 46860 operating with a Super-X divertor (SXD). Both shots lasted roughly 900ms. For each front location in the scan, a corresponding upstream density is calculated, separately using the midplane Thomson and interferometry diagnostics.

Once the front locations are calculated for both shots, the DLS model is applied to every timestamp. The simple DLS model is used here, applied to the EFIT equilibrium data for the given timestamp, with the upstream defined as the midplane (i.e., Equation 2.52 is used). The experimental front location is inputted into the model, which then returns a control parameter required for that front position. Thus, for each shot the predicted variation in density can be calculated.

In Figure 5.5 the MWI-determined front movement is plotted against density variation, with the DLS predicted density variation (normalised to the density of the first timestamp) also plotted. The left figures show the profiles for shot 47079, and the right hand figures show the results of shot 46860. The upper plots use the density calculated from the interferometry, and the lower plots use the density from the Thomson.

As expected, these figures do not show very good agreement between the DLS model and experimental results. However, similar to the SOLPS-ITER results in

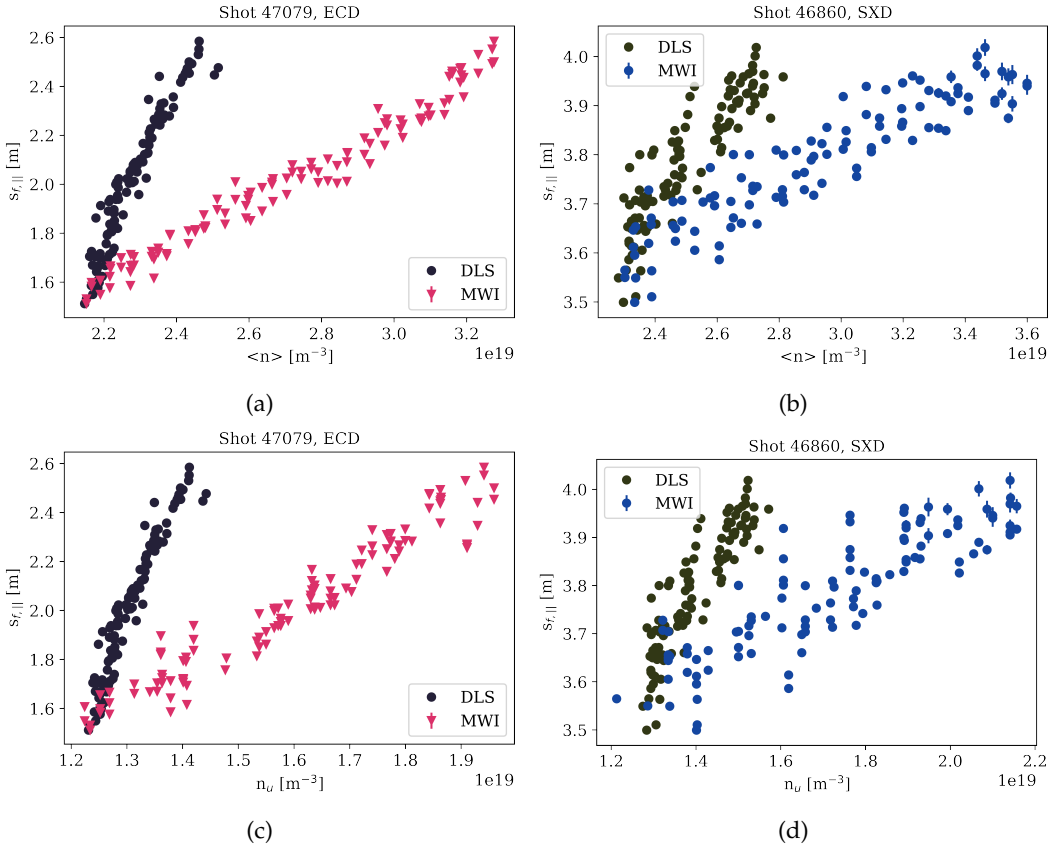

FIGURE 5.5: The detachment front position variation measured by the MWI plotted with respect to the interferometry line-averaged density (top) and Thomson upstream density (bottom). The density variation predicted by the DLS model for the given front positions are overlaid, normalised to the first chronological point in the shot. The left figures show this comparison for shot 47079 (ECD), and the right figures show this comparison for shot 46860 (SXD).

Chapter 3, the front movement is significantly (3 to 5 times) less sensitive in experiment compared to DLS predictions. The consistency between simulation and experiment is encouraging, and reinforces the overarching conclusion that adding more complex physics leads to wider windows of detachment than predicted by the DLS model. Or, in other words, the density variation required in experiment to move the same distance is always higher than predictions.

In terms of qualitative profiles, the shapes of the curves predicted by the DLS model are similar to the experimental front movement with respect to changes in density. In particular, the experimental ECD front movement shows a very tightly packed linear trend with respect to density; the DLS model predictions show a similar trend.

In addition to Figure 5.5, the detachment front location against density variation is plotted in Figure 5.6 (for both the ECD and SXD, interferometry and Thomson), but for front locations determined by the DMS. Inspecting the ECD data first, we again see a tightly packed linear trend of front evolution against density variation, both for the DLS and experimental data. The SXD data, on the other hand, shows a

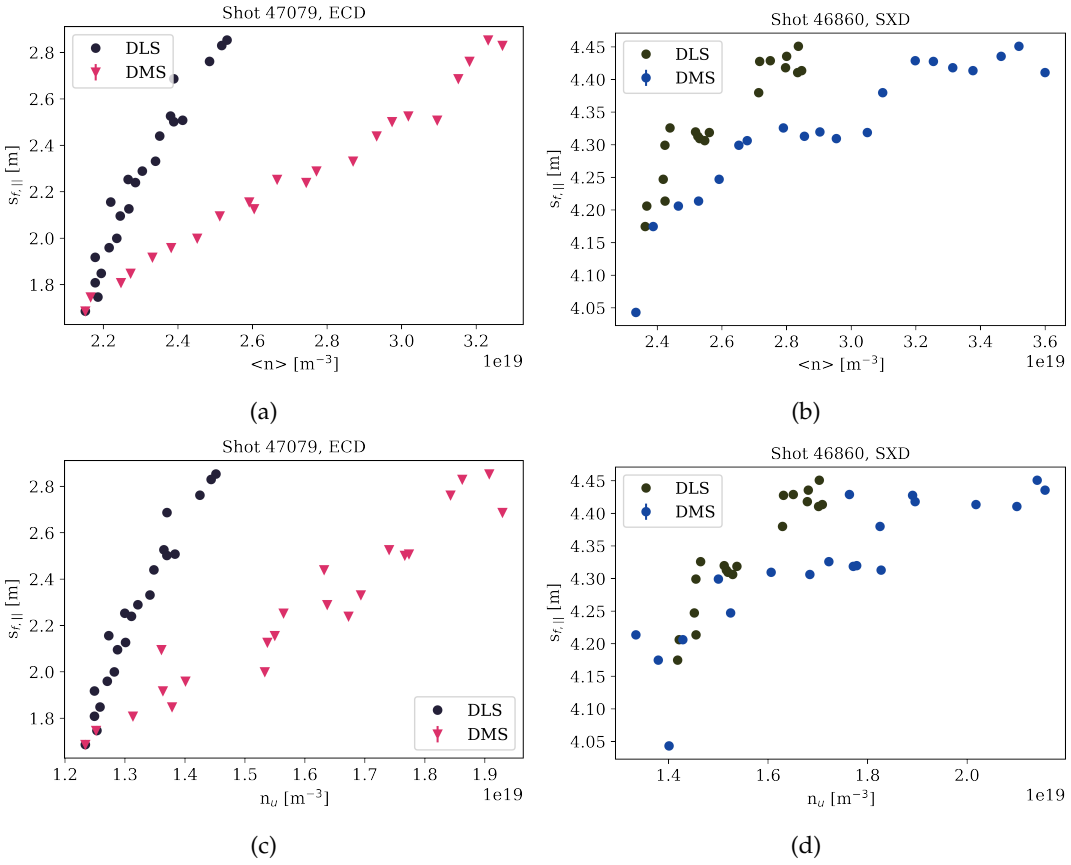

FIGURE 5.6: The detachment front position variation measured by the DMS plotted with respect to the interferometry line-averaged density (top) and Thomson upstream density (bottom). The density variation predicted by the DLS model for the given front positions are overlaid, normalised to the first chronological point in the shot. The left figures show this comparison for shot 47079 (elongated conventional), and the right figures show this comparison for shot 46860 (SXD).

scattered profile with no clear consistent trend. Interestingly though, the DLS model is able to well replicate the shape of this data, including the steep slope (sensitivity) at the start of the scan, and a flattening of the slope for the last 6 points in the scan. Consistently, the comparison again shows the experimental data is generally 3-5 times less sensitive than DLS model predictions.

5.3 The Influence of Divertor Configuration on Detachment Location Sensitivity

5.3.1 Modelling Predictions

In addition to investigating the absolute front movement in a particular configuration, it is perhaps more valuable to investigate predictions made by the DLS model as to how detachment evolution varies across different configurations. Unlike the

absolute front movement, one may expect the DLS model to better predict variations between equilibria, since some effects may hold true even if some DLS model assumptions are broken. In particular, the ability for magnetic flux expansion to reduce instantaneous parallel heat fluxes is true regardless of plasma regime or power dissipation mechanisms.

When it comes to the influence of total magnetic flux expansion on detachment, the DLS model predicts variations in both detachment access and location sensitivity. The effect of total flux expansion on detachment access has been studied experimentally [111], and has been investigated in the initial campaigns in MAST-U [110], [157]. What has not been studied in any device, however, is the variation of detachment location sensitivity, across configurations with different magnetic field profiles, and across the profile of a single configuration. One key prediction made by the DLS model is that in regions of high magnetic field gradient $\frac{1}{B}\frac{dB}{ds}$, the location of detachment fronts should be less sensitive to variations in control parameter(s).

5.3.2 Testing Predictions

To test this prediction, the detachment front movement in the elongated divertor configuration in shot 47079 is compared to the front movement in the Super-X configuration of shot 46860. The idea here being that at the same major radius, the more horizontal leg of the Super-X should have a higher local gradient in the total magnetic field strength. The same data presented in the previous section is also analysed here; front position and density variation data for the density ramps. Rather than comparing to the DLS model, here the front movements in the two configurations are compared against each other. Figure 5.7 shows the front movement with respect to density variation, for a front defined as the 50% and 20% fall-off in peak Fulcher emission. The four sub-figures show different combinations of diagnostics, with the following combinations: a) MWI/Interferometry, b) MWI/Thomson, c) DMS/Interferometry, and d) DMS/Thomson. It is important to note that the front movement for this plot is in the parallel direction.

From Figure 5.7 several conclusions can be drawn. An initial point to note is that for the same density, the SXD configuration is significantly more detached than the ECD, with the parallel front position from the target differing by more than 2m at maximum. This is expected since the Super-X is predicted to detach easier due to total flux expansion, and indeed does so in experiment. A significantly more novel conclusion is that the four sub-figures show consistently that the front movement is less sensitive (lower slope) in the Super-X configuration. In fact, on average the location sensitivity is 2.5 times lower in the Super-X than in the ECD. In other words, the same variation in density causes the front to move 2.5 times less in the parallel direction in the Super-X than in the ECD. This agrees reasonably well with the DLS model, which predicts a 3.3 times lower sensitivity in the Super-X scan than in the ECD.

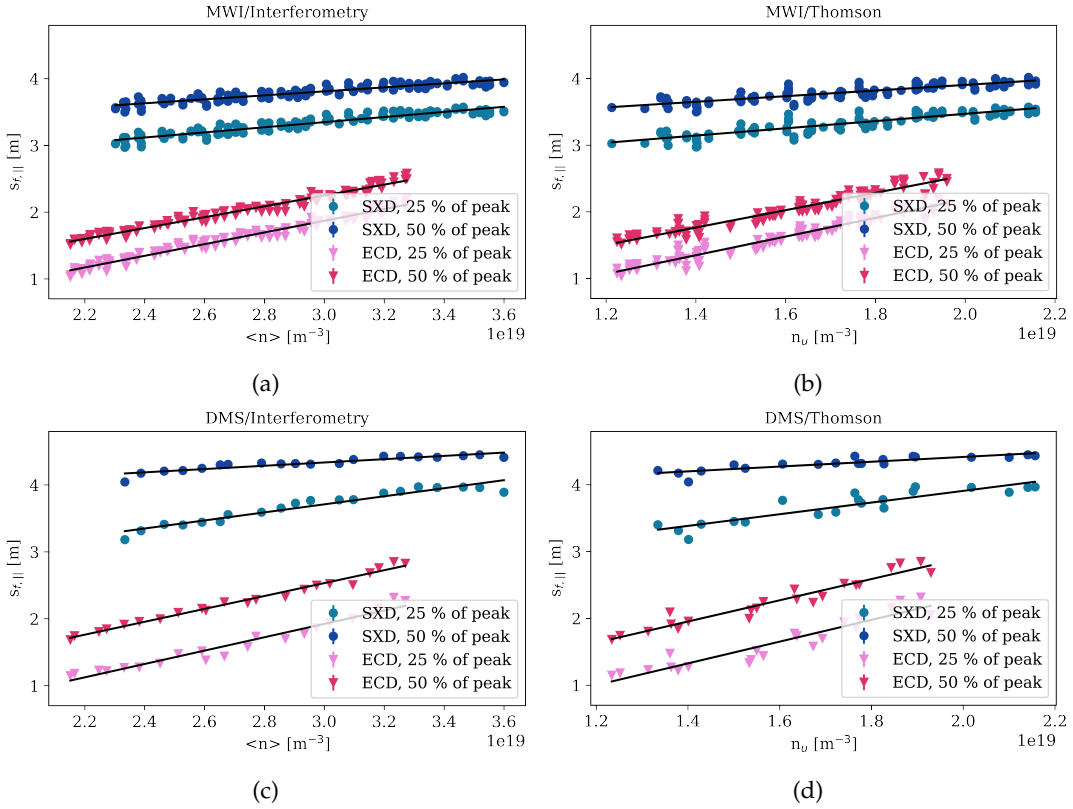

FIGURE 5.7: The front position variation measured by the MWI (a and b) and the DMS (c and d), plotted with respect to the line-averaged density from midplane interferometry (a and c) and the upstream density from the midplane Thomson (b and d) for shots 46860 (SXD) and 47079 (ECD). Data in these Figures is the same as that of Figures 5.5 and 5.6

At first the interpretation of Figure 5.7 may seem straightforward: the Super-X configuration, which should have higher magnetic field gradients, is predicted to have a lower location sensitivity in the detachment scan than the ECD, and experimental results show this is indeed so. However, though it is true that the experimental and predicted sensitivity in parallel space is lower in the Super-X, the figure does not necessarily indicate *why*. To investigate why, the total magnetic field profiles are plotted for all timestamps used, and are shown in Figure 5.8, with darker shades corresponding to equilibria later in time. The range in front movement measured by the MWI is indicated in this figure by grey lines.

From figure 5.8, one may pick out the equilibria at the start of each scan and ask whether the magnetic field gradient in the Super-X is significantly higher than the conventional in the regions of front movement. The difference in magnetic field at the start and end of the front movement, for the starting stationary equilibrium is indicated by $\Delta B_{stationary}$. Surprisingly, for the static equilibria at the start of each scan, the total magnetic field gradients are quite similar between the two configurations. As a result, the magnetic field difference considering the front movement if the equilibrium is higher (15%) in the ECD than in the SXD (6%).

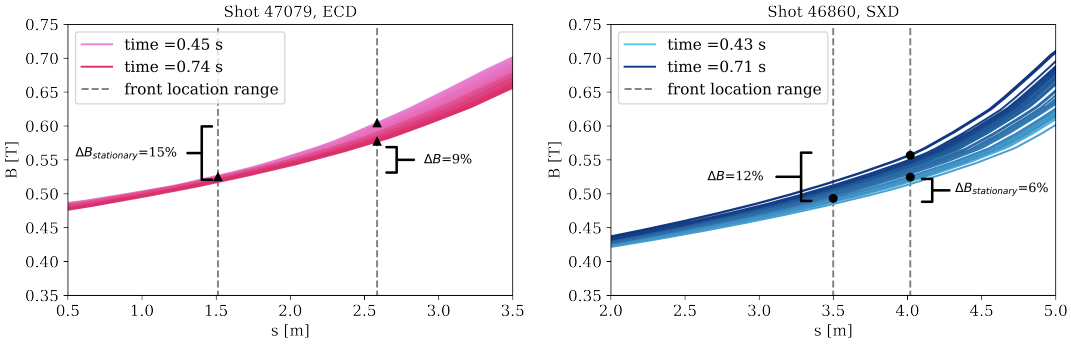

(a) (b)

FIGURE 5.8: The total magnetic field profiles for the shots A) 47079 (ECD) and b) 46860 (SXD), plotted for all timestamps where darker lines are later in time. The bounds of MWI-measured front movement are shown by dashed grey lines.

So why is the front movement predicted to be different, if the equilibria at the start of each scan have similar magnetic field gradients? Well, Figure 5.8 shows that both equilibria are evolving measurably in time. In fact, the magnetic field of the ECD decreases with time, and that of the SXD increases in time. As a result, the actual difference in front magnetic field at the start and end of the scan is greater is greater in the SXD (12 %) than the ECD (9%).

One may initially think that a change in magnetic field of a few percent may not be great enough to cause the large difference in sensitivity. However, one must remember that the detachment fronts are moving in a small area in the machine, and what really matters is the *relative difference* in the magnetic field change between the SXD and ECD. In the static equilibria, the change in magnetic field in the ECD case is 2.5 times larger than the SXD case. However, when the time variation is considered this factor is 0.75, meaning the relative magnetic field gradients between the two grids changes by more than a factor of 3 depending on whether the time varying equilibrium is considered. Thus, the time variation in magnetic field is likely what causes front movement to slow down with regards to changes in density. Not, as was previously thought, the magnetic field profile in a single static configuration.

Noting this in-depth analysis of the magnetic field profiles, what can now be concluded about the predicted impacts of magnetic configuration on detachment location sensitivity? At the start of this section, the aim was to answer whether the predicted impact of magnetic field gradients on detachment location sensitivity hold true by comparing two static configurations. In this investigation, the DLS model predicted that a scan in density for a given dynamic shot would lead to less parallel front movement in the Super-X case compared to the conventional. In other words, the *scan* (rather than configuration) in the Super-X should have led to a lower sensitivity in parallel space. This was confirmed, with a good degree of confidence. Consequently, this study supports the idea that principles of the DLS model can be used to predict how front movement changes in different divertor geometries.

5.3.3 The Impact of Poloidal Field

Another interesting exercise for this investigation is to plot the detachment front movement data in Figure 5.7, but with front location expressed in poloidal space. This distance is a very important one for detachment control, as it is often used in control algorithms, and this distance is likely more important than parallel front location in determining the strength of atomic and molecular processes downstream of the front. The poloidal front movement data is shown in Figure 5.9, and conveys a very different story to the parallel front data in Figure 5.7. In particular, the figure shows the poloidal front movement in the Super-X configuration has similar sensitivities to the movement in the conventional configuration. In fact, the average location sensitivity in the Super-X scan is only 10% lower than the conventional. Why is this?

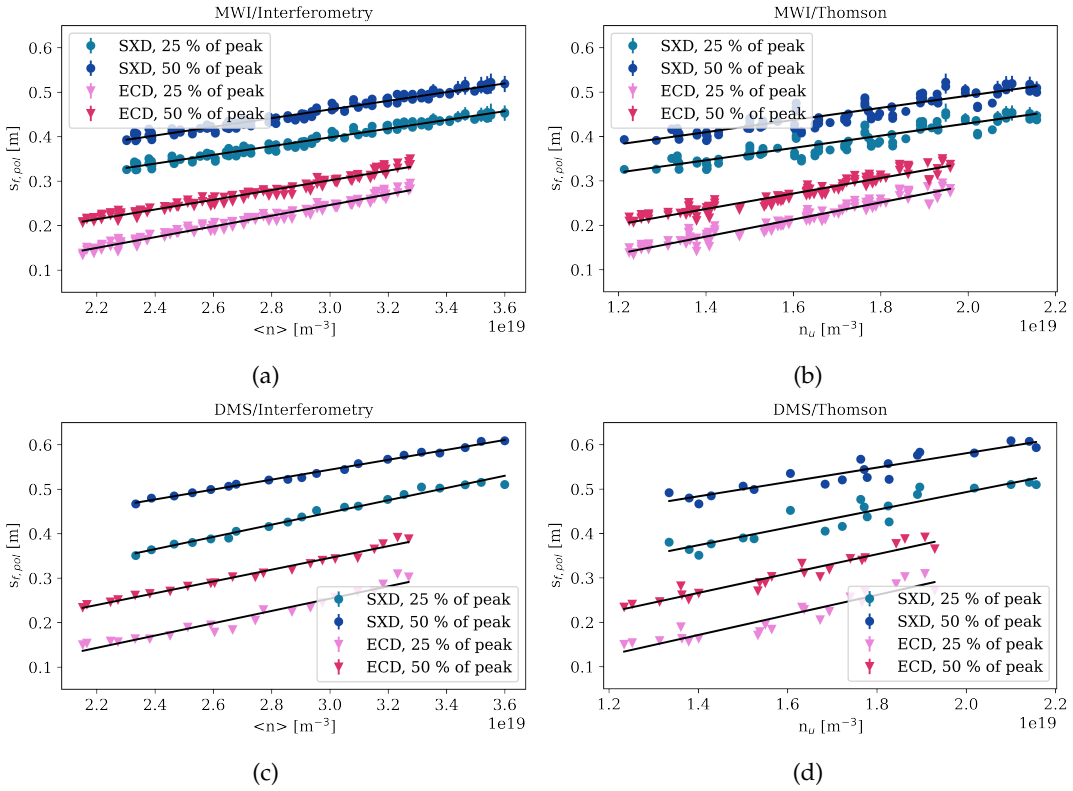

FIGURE 5.9: The front position variation measured by the DMS plotted with respect to the a) line-averaged density from midplane interferometry and b) the upstream density from the midplane Thomson for shots 46860 (SXD) and 47079 (ECD).

Ultimately, the only reason front movement would look different in the poloidal direction compared to the parallel direction is a variation poloidal pitch, $\frac{B_{pol}}{B}$. Specifically, the fact that a very small variation in parallel position in the Super-X corresponds to a large variation in poloidal position implies that the poloidal pitch increases at the end of the scan. To investigate this, the relationship between parallel and poloidal distance along a field line is shown for all equilibria for both shots in Figure 5.10, with darker shades corresponding to equilibria later in time.

Figure 5.10 indeed shows the poloidal pitch varies with time, particularly in the SXD shot. In this shot, the average pitch in the divertor increases, meaning a parallel distance from the target corresponds to more poloidal distance. Thus, even though the front only moves a small amount in parallel space, in the SXD this given amount corresponds to a further and further poloidal distance as the equilibria evolves. increase in the poloidal pitch in the divertor later in the scan for the SXD. Hence the effective front movement throughout the scan seems less sensitive in the poloidal plane for the SXD.

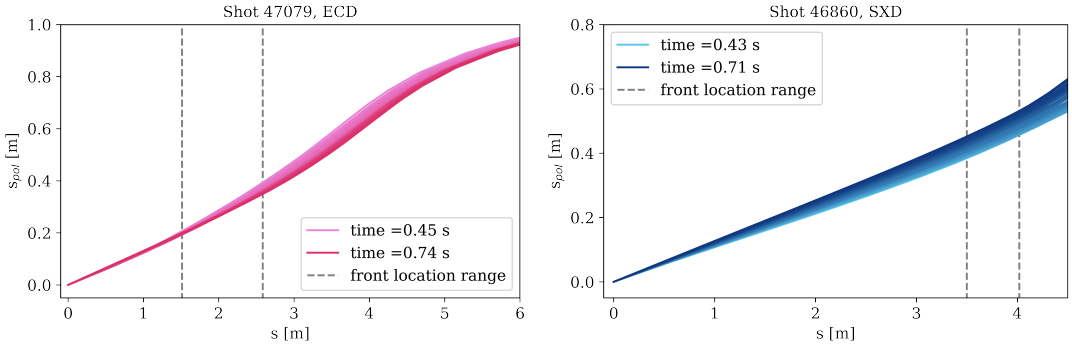

(a) (b)

FIGURE 5.10: The relationship between poloidal and parallel distance along the separatrix for the shots a) 47079 (ECD) and b) 46860 (SXD), plotted for all timestamps where darker lines are later in time. The bounds of MWI-measured front movement are shown by dashed grey lines.

5.4 The Importance of Physics Upstream of the Front

5.4.1 Modelling Predictions

One of the most important elements of the DLS model is that it models the region upstream of a detachment front, and neglects physics downstream of this front location. Hence, how the location of detachment moves is entirely determined by physics upstream of the front. A consequence of this is that, if a divertor geometry is changed, and the magnetic field profile upstream of the front is not significantly modified, then a detachment front will maintain a constant $L_{||,f}$, defined as the distance from the front to the midplane. This does not mean of course that the distance from the front to target will remain constant, and in fact the DLS model predicts this will change as the divertor equilibrium is varied with constant upstream conditions.

5.4.2 Testing Predictions

To test the prediction of upstream physics dominating front dynamics, the detachment front has been tracked for the shot 46895 in MU02. In this shot, the density and input power were held roughly constant, whilst the magnetic equilibrium was

varied. As a result, throughout the 800ms shot, the outer strike point varied from R=0.9m (corresponding to a conventional divertor) to R= 1.5m (corresponding to a Super-X). Inverted emissivity plots from the MWI for this shot are shown for several timestamps in Figure 5.11.

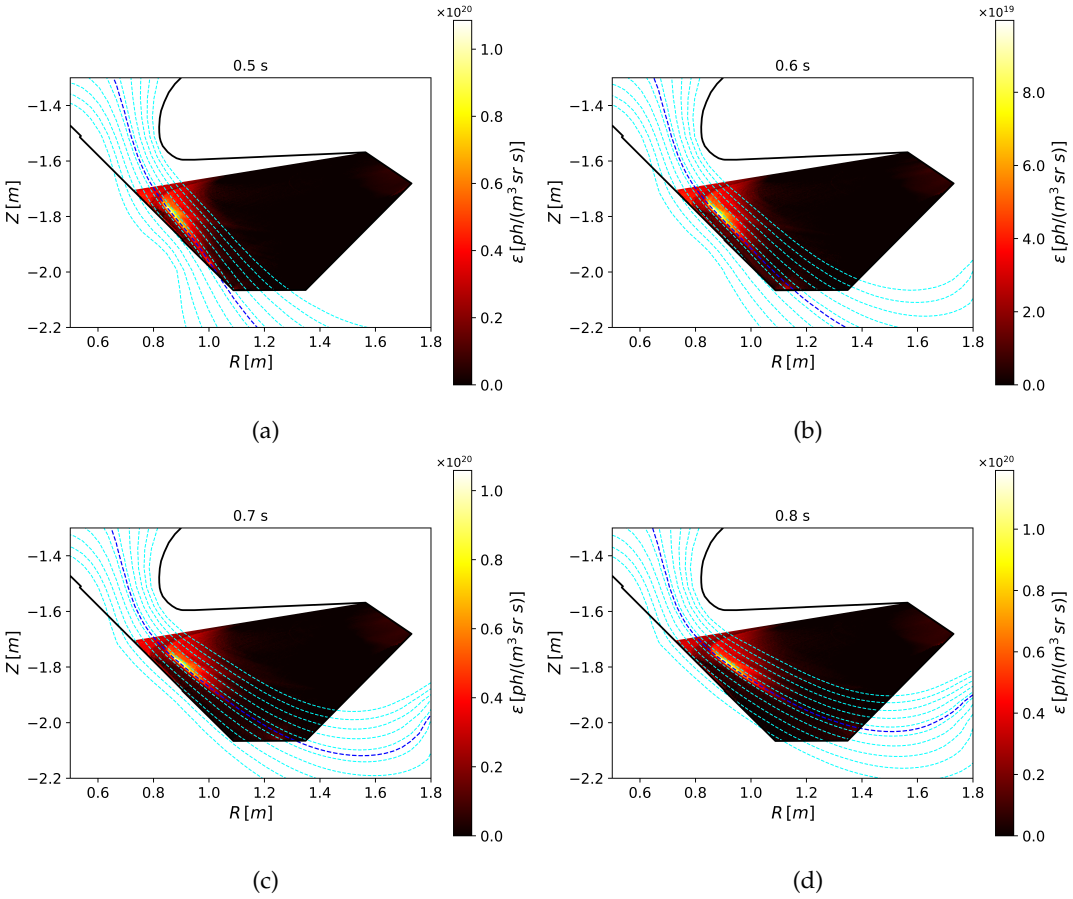

FIGURE 5.11: Inverted emissivity profile from the MWI diagnostic, for shot 46895 at t= a) 0.5s, b) 0.6s, c) 0.7s, and d) 0.8s. Overlaid is the magnetic equilibrium.

Because the density and input power were held roughly constant in this shot, the DLS model predicts that the front location (measured from upstream) should be held constant. Of course, this front location measured from the target should be varying significantly. The MWI-determined front location is plotted against the strike point major radius in Figure 5.12a, and from this figure a clear picture emerges. Indeed, at the start of the discharge, the target is attached, and as the strike point is swept out to a larger major radius, the divertor becomes more detached and the distance between the front and target increases.

What's more, Figure 5.12b shows the variation in divertor connection length as a function of strike point major radius. The variation in connection length is a very similar profile to the variation in front position from the target in Figure 5.12a, which tends to support the DLS model predictions. After all, this similarity shows that the increase in front distance from the target may simply be due to an increase in length

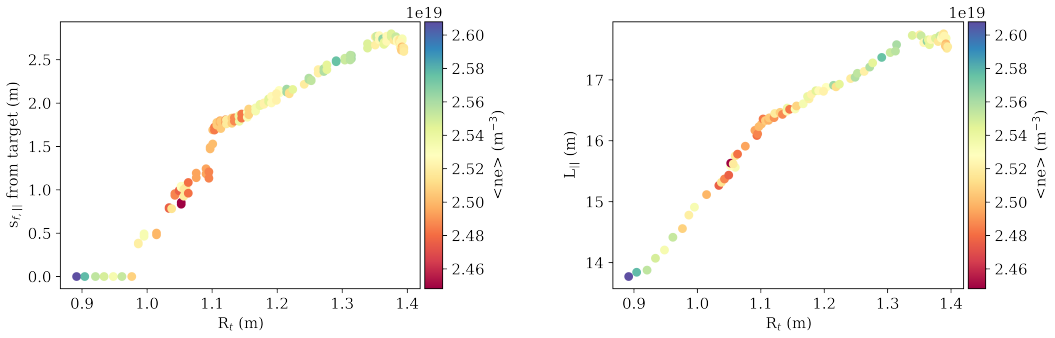

(a) (b)

FIGURE 5.12: a) The poloidal detachment front location, measured from the target, plotted against strike point major radius for a strike point sweep experiment in shot 46895 in MAST-U. b) The divertor connection length, plotted against strike point major radius for a strike point sweep experiment in shot 46895 in MAST-U. The colour of the points indicates the interferometry midplane density, which only varies by a maximum of 10% throughout the entire scan.

downstream of the front; the distance upstream of the front may remain the same.

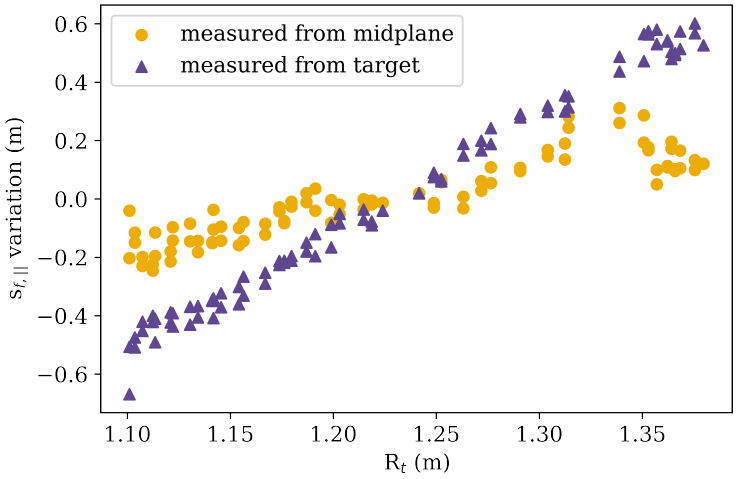

FIGURE 5.13: The variation of detachment front location in the parallel direction, plotted with respect to strike point major radius for shot 46895. The two sets of data correspond to the detachment position measured from the target, and from the midplane. Variation is plotted relative to the mean location in the scan.

To investigate this further, the variation in front position measured from the midplane is calculated and plotted in Figure 5.13. On the x-axis, the variation in distance from the front to the target is plotted. From this figure it is clear to see while the front location measured from the target varies significantly, the distance measured from the midplane varies less so. In fact, while the distance from the target varies by a standard deviation of 0.8m, the distance from front to midplane only varies by 0.25m in the scan. Curiously, the front still seems to be moving towards the upstream as the strike point leg is swept out, even when measured from the midplane. Perhaps

this is due to a change in atomic and molecular physics near the targets, or a change in effective baffling and recycling due to a different strike point angle.

Finally, the importance of the front position measured from the midplane can be further investigated by analysing shots 46860 and 47079 used in the previous sections. In particular, the front movement from these two shots - which have the same input power - can be plotted in terms of the parallel distance from the midplane, rather than the target. If the magnetic field strength is roughly constant, the front location movement relative to the density variation should be identical in the two configurations. The MWI front movement defined by the 50% fall-off in Fulcher emission is plotted with regards to interferometry density and Thomson density in Figures 5.14a and 5.14b respectively. Indeed, these figures show the front movement measured from the midplane is very similar between the two configurations. In fact, whereas the front location measured from the target consistently varied by 2m, the front location measured from the midplane differs by 0.5m at maximum for the same density.

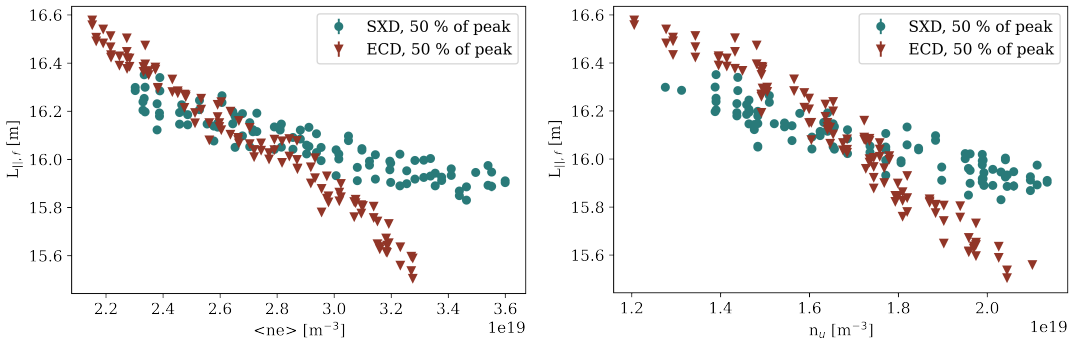

(a) (b)

FIGURE 5.14: The variation in detachment front location defined as the 50% fall-off in the peak emission from the MWI. The front location is measured from the midplane for shots 46860 (SXD) and 47079 (ECD), plotted with respect to a) interferometry density and b) Thomson density.

Overall, it seems that the location of a detachment front measured from the midplane is what is more likely what is determined by detachment control parameters; not the front position from the target. This supports the underlying physical principle of the DLS model that detachment front location is determined by the plasma profile upstream of the front. Moreover, this conclusion may be vital for understanding and controlling detachment front movement in machines which may operate with different configurations. After all, if one attempts to control the front location measured from the target, it may seem as though there is a different relationship governing front movement for each different configuration. This complexity may be simplified by instead focusing on the front location measured from the midplane, which seems to present a unifying relationship throughout multiple equilibria.

Of course, this is not to say the physics downstream of a detachment front is not

important. In fact, this distance is critical in removing further energy and momentum fluxes, and determining the all-important conditions at the target. Studying how this target measured front distance can affect target conditions is an incredibly important area of study, filled with a complex array of atomic and molecular physics. However, this complex study of the detached region lies outside the scope of this thesis.

5.5 Summary

For the first time, experimental detachment evolution has been compared to modelling predictions in the MAST-U tokamak. The front locations, determined by the MWI and DMS diagnostics, have been compared to the electron density variation recorded by the midplane interferometry and Thomson scattering systems. The profile of front movement against plasma density does not match perfectly well with DLS model predictions. Furthermore, the experimental front movement is significantly less sensitive then the DLS model predictions. This is in line with the conclusions found in Chapter 3 when comparing the DLS model and SOLPS-ITER simulations.

When comparing front movement in an elongated conventional and Super-X divertor, modelling predicts the movement should be less sensitive in parallel space in the elongated conventional than in the Super-X. Indeed, a factor 2.5 reduction in sensitivity is seen experimentally in the Super-X. However, this reduction in sensitivity seems less to do with the properties of the stationary Super-X configuration, and more pertaining to the evolution of the equilibrium throughout the shot.

Finally, the definitions of front location defined from the target and from the midplane were compared. The DLS model predicts that the front location measured from the midplane is the important quantity in determining the required detachment control parameter(s), and consequently this should not change as an equilibrium is varied with constant control parameters. Investigating experimental front movement in the Super-X and elongated conventional density scans, in addition to a strike point sweep experiment, it indeed seems as though the location of detachment from the midplane is held roughly constant for a constant set of control parameters.

This work is presented with the caveat that it has been applied to early campaigns of MAST-U, on L-mode discharges at modest powers. The DLS model, however, is best geared towards impurity-seeded, high-power H-mode experiments. Because of the experimental uncertainties and the non-ideal plasma parameters, this comparative study must be developed further. In MAST-U, this can be done by applying the DLS model to high power H-mode discharges in alternative divertors, which are planned for future campaigns. Moreover, more diagnostics are set to be applied in the MAST-U device, including an X-point imaging camera which views outside the MWI view, and could act to decrease some of the experimental uncertainties of the MWI.

Chapter 6

Conclusions and Outlook

In this thesis, the physics of divertor features has been explored through modelling techniques, for the end purposes of alternative divertors, divertor design, and the plasma exhaust challenge. From the various strands of work contained in this thesis, several novel conclusions have been reached concerning how alternative divertor features can affect exhaust and the process of detachment. These conclusions fall into three basic categories; pertaining to reduced modelling, simulation work, and experimental comparison.

Concerning reduced modelling, the DLS model has been introduced as a tool to study detachment, and unique extensions have been made to the model as part of this body of work. The DLS model predicts how detachment access and control can be facilitated through the magnetic configuration of a divertor. Specifically, the model predicts that detachment fronts should be less sensitive to control parameters in regions of strong magnetic field gradients, low poloidal field, or regions close to the x-point.

As part of this thesis, the DLS model has been extended, to allow for numerical computation of self-consistent heat flux and temperature profiles in a detached divertor. This extended model differs from the standard DLS model when there is a significant proportion of radiation occurring upstream, and the assumptions of the simple DLS model fail. The extended model should give better results for reactor-relevant devices, where the injection of high-Z impurities will likely cause radiation along the entire SOL.

If verified, the DLS modelling framework has the capacity to aid divertor design for future tokamaks, and contribute to developing experimental systems for detachment control.

Concerning simulations, analytical predictions of detachment front evolution have been compared against simulations for the first time. Specifically, hundreds of isolated divertor leg SOLPS-ITER simulations have been run in different geometries to test predictions made by the DLS model.

From this comparison, the DLS predicted impact of divertor features on detachment location sensitivity are largely confirmed by SOLPS-ITER simulations. Regions with strong magnetic field gradients, regions close to the x-point, and regions with poloidal flaring all have reduced detachment location sensitivity - both predicted

by the DLS model and simulated by SOLPS-ITER. The DLS prediction of negative location sensitivity regions is also confirmed by SOLPS-ITER simulations. In such regions, for the same control parameters, the simulations may converge to attached or deeply detached solutions. This agreement verifies the DLS model as a tool to predict the impact of magnetic geometry on detachment front movement. This marks the first verified analytical framework for modelling detachment location sensitivity.

Simulations have also been performed on a real MAST-U symmetric double-null Super-X geometry. This geometry is used to perform a baffling code-experiment in SOLPS-ITER. Density scans were performed for the Super-X geometry with extremely tight baffling and extremely open baffling, with an artificial nitrogen impurity. These experiments show easier detachment access in the tightly baffled case, and at the same level of detachment the tightly baffled case can maintain higher upstream temperatures. This ability for tightly baffled divertors to access good target conditions whilst maintaining a low upstream collisionality indicates tightly baffled divertors have significant benefits for core-edge integration. However, these benefits of the tightly baffled divertor seems to reduce at higher power; calling into question whether knowledge gained by baffling studies on low-power devices can extrapolate to reactor tokamaks.

Concerning experiments, for the first time an effort has been made to understand the physical processes governing the experimentally observed movement of detachment fronts. This effort is made by comparing detachment front tracking data and midplane density data in MAST-U to the DLS model. Notably, comparing the detachment front movement in a Super-X divertor to an elongated conventional divertor, the difference in detachment location sensitivity is found to be consistent with DLS model predictions.

Experimental analysis of detachment fronts in MAST-U show that front movement in different geometries is remarkably similar when the location of detachment fronts is measured from the midplane. This tends to support a fundamental idea of the DLS model that the location of detachment fronts is determined by physics upstream of the leading edge of detachment. Though in general this experimental work is not a concrete validation of the DLS model, it is preliminary data to support certain overarching principles of the model.

Ultimately, for every conclusion made in this body of work, there are a myriad of unanswered questions and areas to explore. For example, this work has shown that though reduced modelling can be powerful, it is by no means perfect, and many of these models neglect important physics such as pressure variation and cross-field transport. Finding ways to meaningfully implement physics such as pressure loss, hydrogenic power losses, and radial transport losses in 1d flux tube models, for example, is a ripe area of study. The DLS model also says nothing concerning how target parameters evolve as detachment fronts move; since the formulation only models upstream of the front location. Relating this front location back to target parameters is a significant open question. Another crucial aspect of divertor design

not considered by this simple modelling is engineering and cost constraints. Thus, these simple modelling considerations should be coupled with engineering information for a more integrated design of divertors.

The simulation work presented here lacks drifts and neglect the full transport of impurities and their different charge states. Studying how this impurity transport varies with divertor configuration is another fertile area of study. Moreover, the simulations presented are fluid/kinetic simulations of the mean-field profile of a tokamak plasma boundary, and the radial transport coefficients are set by the user, and are not set empirically. Other types of simulations, such as gyrokinetic simulations of plasma turbulence can shed light on how alternative divertor features may affect cross-field transport in the SOL and across the separatrix.

Finally, it must be stressed that the experimental work presented in this thesis marks the start - not the completion - of understanding physical processes behind detachment evolution in real devices. The experimental campaigns studied here are only a handful of 1.5 MW L-mode discharges. For more apt comparison to the DLS model, a higher power H-mode scenario should be used, with a seeded impurity such as nitrogen. Moreover, developing better statistics, by leveraging more experiments across different scenarios or even devices, would help alleviate much of the experimental uncertainty, and allow more certain conclusions about the potential uses of the DLS model.

With the work presented here, and the further work that may evolve from it, this thesis contributes to the field of alternative divertors and the physics of detachment. And by advancing exhaust physics one step further, this work progresses solutions to the challenges facing reactor tokamaks. Contributing to the global, generation-spanning effort to achieve controlled fusion on Earth.

Appendix A

Boundary Conditions for the Extended DLS Model

In the extended DLS model, the differential equations governing heat and temperature evolution are integrated from the target, and boundary conditions $T_t = 0$ and $q_{||,t} = 0$ cannot be used. As such a sufficiently low temperature and heat flux can be used. Figures A.1a and A.1b show the outputted heat flux profiles for the start and end of a detachment scan using the extended DLS model. In Figure A.1a, the scan is repeated with two target temperature boundary conditions; 1 eV and 5 eV. In this Figure, the two profiles produce almost identical results, indicating the choice of target temperature does not matter as long as it is low but not beyond the boundary of the cooling function used.

Similarly, Figure A.1b shows the outputted heat flux profiles when two very different target heat flux boundary conditions are used; 10 KWm^{-2} and 1000 KWm^{-2}. These profiles are also very similar, highlighting the choice of target heat flux also does not matter significantly as long as it is low compared to the upstream heat flux, but not too low as to not lead to significant temperature gradients.

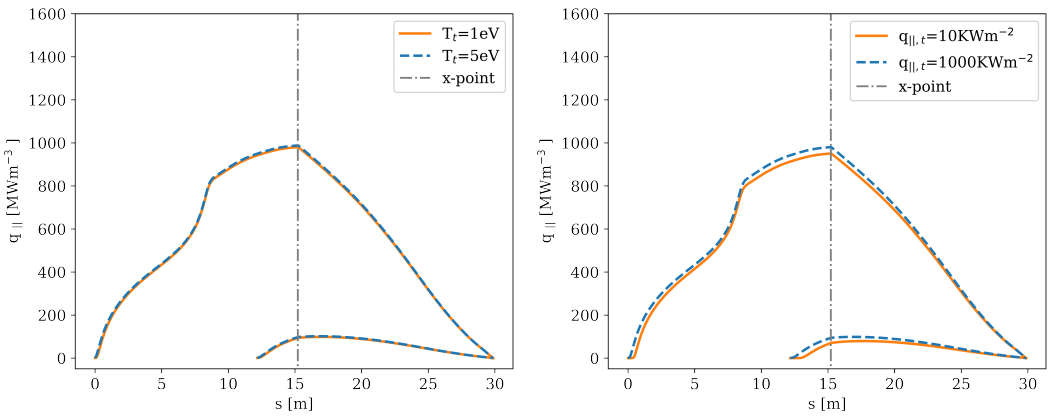

(a) (b)

FIGURE A.1: The outputted heat flux profiles from the DLS model for a) two different target temperature boundary conditions, and b) two different target heat flux boundary conditions.

Bibliography

[1] X. Bonnin, W. Dekeyser, R. Pitts, D. Coster, S. Voskoboynikov, and S. Wiesen, "Presentation of the new solps-iter code package for tokamak plasma edge modelling," *Plasma and Fusion Research*, vol. 11, pp. 1 403 102–1 403 102, 2016.

[2] S. Wiesen, D. Reiter, V. Kotov, *et al.*, "The new solps-iter code package," *Journal of nuclear materials*, vol. 463, pp. 480–484, 2015.

[3] D. Reiter, M. Baelmans, and P. Boerner, "The eirene and b2-eirene codes," *Fusion science and technology*, vol. 47, no. 2, pp. 172–186, 2005.

[4] B. Lipschultz, F. I. Parra, and I. H. Hutchinson, "Sensitivity of detachment extent to magnetic configuration and external parameters," *Nuclear Fusion*, vol. 56, no. 5, p. 056 007, 2016.

[5] E Havlíčková, J Harrison, B Lipschultz, *et al.*, "Solps analysis of the mast-u divertor with the effect of heating power and pumping on the access to detachment in the super-x configuration," *Plasma Physics and Controlled Fusion*, vol. 57, no. 11, p. 115 001, 2015.

[6] C. Cowley, B. Lipschultz, D. Moulton, and B. Dudson, "Optimizing detachment control using the magnetic configuration of divertors," *Nuclear Fusion*, vol. 62, no. 8, p. 086 046, Jul. 2022. DOI: 10.1088/1741-4326/ac7a4c. [Online]. Available: https://dx.doi.org/10.1088/1741-4326/ac7a4c.

[7] O. Myatra, B. Lipschultz, D. Moulton, *et al.*, "Predictive solps-iter simulations to study the role of divertor magnetic geometry in detachment control in the mast-u super-x configuration," *Nuclear Fusion*, vol. 63, no. 9, p. 096 018, Aug. 2023. DOI: 10.1088/1741-4326/acea33. [Online]. Available: https://dx.doi.org/10.1088/1741-4326/acea33.

[8] C Cowley, A. Q. Kuang, D Moulton, *et al.*, "Novel solps-iter simulations of x-point target and snowflake divertors," *Plasma Physics and Controlled Fusion*, vol. 65, no. 3, p. 035 011, Feb. 2023. DOI: 10.1088/1361-6587/acb4ba. [Online]. Available: https://dx.doi.org/10.1088/1361-6587/acb4ba.

[9] K. Bithas, P. Kalimeris, K. Bithas, and P. Kalimeris, "A brief history of energy use in human societies," *Revisiting the Energy-Development Link: Evidence from the 20th Century for Knowledge-based and Developing Economies*, pp. 5–10, 2016.

[10] N. Crafts and T. C. Mills, "Six centuries of British economic growth: a time-series perspective," *European Review of Economic History*, vol. 21, no. 2, pp. 141–158, Feb. 2017, ISSN: 1361-4916. DOI: 10.1093/ereh/hew020. eprint: https://academic.oup.com/ereh/article-pdf/21/2/141/23531938/hew020.pdf. [Online]. Available: https://doi.org/10.1093/ereh/hew020.

[11] D. B. GRIGG, "The world's agricultural labour force 1800-1970," *Geography*, vol. 60, no. 3, pp. 194–202, 1975, ISSN: 00167487. [Online]. Available: http://www.jstor.org/stable/40568423 (visited on 08/31/2023).

[12] International Labour Organisation, "Spotlight on work statistics n°11," in Oct. 2020. [Online]. Available: https://ilo.org/wcmsp5/groups/public/---dgreports/---stat/documents/publication/wcms_757960.pdf.

[13] T. Sadraoui, H. Hamlaoui, Z. Youness, and B. Sadok, "A dynamic panel data analysis for relationship between energy consumption, financial development and economic growth," *International Journal of Econometrics and Financial Management*, vol. 7, no. 1, pp. 20–26, 2019.

[14] J. C. Steckel, R. J. Brecha, M. Jakob, J. Strefler, and G. Luderer, "Development without energy? assessing future scenarios of energy consumption in developing countries," *Ecological Economics*, vol. 90, pp. 53–67, 2013, ISSN: 0921-8009. DOI: https://doi.org/10.1016/j.ecolecon.2013.02.006.

[15] C. Pasten and J. C. Santamarina, "Energy and quality of life," *Energy Policy*, vol. 49, pp. 468–476, 2012, Special Section: Fuel Poverty Comes of Age: Commemorating 21 Years of Research and Policy, ISSN: 0301-4215. DOI: https://doi.org/10.1016/j.enpol.2012.06.051.

[16] G. Szustak, P. Dąbrowski, W. Gradoń, and Ł. Szewczyk, "The relationship between energy production and gdp: Evidence from selected european economies," *Energies*, vol. 15, no. 1, p. 50, 2021.

[17] National Oceanic and Atmospheric Administration, *Trends in atmospheric carbon dioxide*. [Online]. Available: https://gml.noaa.gov/ccgg/trends/global.html.

[18] H. Le Treut et al, "Historical overview of climate change," in *Climate Change 2007: The Physical Science Basis. Contribution of Working Group I to the Fourth Assessment Report of the Intergovernmental Panel on Climate Change*, Cambridge: Cambridge University Press.

[19] NASA, *GISS Surface Temperature Analysis (GISTEMP v4)*, 2023.

[20] IPCC, "Summary for policymakers," in *Climate Change 2021: The Physical Science Basis. Contribution of Working Group I to the Sixth Assessment Report of the Intergovernmental Panel on Climate Change*, IPCC.

[21] NASA, *Arctic sea ice minimum extent*. [Online]. Available: https://climate.nasa.gov/vital-signs/arctic-sea-ice/.

[22] D. Notz and S. Community, "Arctic sea ice in cmip6," *Geophysical Research Letters*, vol. 47, no. 10, e2019GL086749, 2020. DOI: https://doi.org/10.1029/2019GL086749.

[23] H.-O. Pörtner et al., "Technical summary," in *Climate Change 2022: Impacts, Adaptation and Vulnerability. Contribution of Working Group II to the Sixth Assessment Report of the Intergovernmental Panel on Climate Change*, Cambridge: Cambridge University Press. DOI: 10.1017/9781009325844.002.

[24] IPCC, "Sea level rise and implications for low-lying islands, coasts and communities," in *Special Report on the Ocean and Cryosphere in a Changing Climate*, IPCC.

[25] W. Yuan, Y. Zheng, S. Piao, *et al.*, "Increased atmospheric vapor pressure deficit reduces global vegetation growth," *Science advances*, vol. 5, no. 8, eaax1396, 2019.

[26] R. D. Bressler, "The mortality cost of carbon," *Nature communications*, vol. 12, no. 4467, 2021.

[27] G. Bouthoul, R. Carrere, and G. Köhler, "A list of the 366 major armed conflicts of the period 1740-1974," *Peace Research*, vol. 10, no. 3, pp. 83–108, 1978.

[28] *Statistical review of world energy*, 2022. [Online]. Available: https://www.bp.com/en/global/corporate/energy-economics/statistical-review-of-world-energy.html.

[29] A. Rabinovich, *The Yom Kippur War: the epic encounter that transformed the Middle East*. Schocken, 2007.

[30] K. R. Merrill, "The oil crisis of 1973–1974: A brief history with documents," *Bedford/St. Martin's, USA*, 2007.

[31] U.S Bureau of Labor Statistics, *Labor force statistics from the current population survey*.

[32] E. P. Davis, "Comparing bear markets-1973 and 2000," *National Institute Economic Review*, vol. 183, pp. 78–89, 2003.

[33] T. Lister and J. Kesa, "Ukraine says it was attacked through russian, belarus and crimea borders," *CNN*, Feb. 2022.

[34] M. Funakoshi, H. Lawson, and K. Deka, "Tracking sanctions against russia," *Reuters*, Mar. 2022.

[35] UK Office for National Statistics, *Cost of living insights: Energy*, 2023.

[36] UK Office for National Statistics, *Consumer price inflation, uk: December 2022*, 2023.

[37] "Expensive energy may have killed more europeans than covid-19 last winter," *The Economist*, May 2023. [Online]. Available: https://www.economist.com/graphic-detail/2023/05/10/expensive-energy-may-have-killed-more-europeans-than-covid-19-last-winter.

[38] E. Baldacci, L. De Mello, and G. Inchauste, "Financial crises, poverty, and income distribution," in *Macroeconomic Policies and Poverty Reduction*, Routledge, 2004, pp. 269–307.

[39] IEA, *Renewable Electricity*. Sep. 2022. [Online]. Available: https://www.iea.org/reports/renewable-electricity.

[40] F. Mulder, "Implications of diurnal and seasonal variations in renewable energy generation for large scale energy storage," *Journal of Renewable and Sustainable Energy*, vol. 6, no. 3, p. 033 105, 2014.

[41] S. Pryor, R. J. Barthelmie, and J. Schoof, "Inter-annual variability of wind indices across europe," *Wind Energy: An International Journal for Progress and Applications in Wind Power Conversion Technology*, vol. 9, no. 1-2, pp. 27–38, 2006.

[42] W. J. Cole, D. Greer, P. Denholm, *et al.*, "Quantifying the challenge of reaching a 100% renewable energy power system for the united states," *Joule*, vol. 5, no. 7, pp. 1732–1748, 2021, ISSN: 2542-4351. DOI: https://doi.org/10.1016/j.joule.2021.05.011. [Online]. Available: https://www.sciencedirect.com/science/article/pii/S2542435121002464.

[43] Federal Statistical Office of Germany, *Electricity production in 2022: Coal accounted for a third, wind power for a quarter*, 2023.

[44] M. Alwaeli and V. Mannheim, "Investigation into the current state of nuclear energy and nuclear waste management—a state-of-the-art review," *Energies*, vol. 15, no. 12, p. 4275, 2022.

[45] *World Energy Resources*. New York: World Energy Council, 2016, p. 4, ISBN: 9780946121588.

[46] N. E. Agency and I. A. E. Agency, *Uranium 2020*. 2021, p. 484. DOI: https://doi.org/https://doi.org/10.1787/d82388ab-en.

[47] N. Takigawa and K. Washiyama, *Fundamentals of nuclear physics*. Springer, 2017.

[48] National Institute for Standards and Technology, *Atomic weights and isotopic compositions for all elements*. [Online]. Available: https://physics.nist.gov/cgi-bin/Compositions/stand_alone.pl?ele=&ascii=ascii2&isotype=some.

[49] F. F. Chen, *Introduction to Plasma Physics and Controlled Fusion*, Third. Springer, 2015.

[50] R. Fitzpatrick, *Plasma physics: an introduction*. Crc Press, 2022.

[51] P. M. Bellan, *Fundamentals of plasma physics*. Cambridge university press, 2008.

[52] T. M. Boyd, T. Boyd, and J. Sanderson, *The physics of plasmas*. Cambridge university press, 2003.

[53] J. D. Lawson, "Some criteria for a power producing thermonuclear reactor," *Proceedings of the physical society. Section B*, vol. 70, no. 1, p. 6, 1957.

[54] International Atomic Energy Authority, *Evaluated nuclear data file database*. [Online]. Available: https://www-nds.iaea.org/exfor/endf.htm.

[55] E. I. Moses, "Ignition on the national ignition facility: A path towards inertial fusion energy," *Nuclear Fusion*, vol. 49, no. 10, p. 104 022, 2009.

[56] J. Wesson and D. J. Campbell, *Tokamaks*. Oxford university press, 2011, vol. 149.

[57] M. Kikuchi, "Steady state tokamak reactor based on the bootstrap current," *Nuclear Fusion*, vol. 30, no. 2, p. 265, Feb. 1990. DOI: 10.1088/0029-5515/30/2/006. [Online]. Available: https://dx.doi.org/10.1088/0029-5515/30/2/006.

[58] W Hooke, "Review of experiments on current drive in tokamaks by means of rf waves," *Plasma Physics and Controlled Fusion*, vol. 26, no. 1A, p. 133, Jan. 1984. DOI: 10.1088/0741-3335/26/1A/312. [Online]. Available: https://dx.doi.org/10.1088/0741-3335/26/1A/312.

[59] T. Hender, J. Wesley, J Bialek, *et al.*, "Mhd stability, operational limits and disruptions," *Nuclear fusion*, vol. 47, no. 6, S128–S202, 2007.

[60] L. R. Baylor, P. Parks, T. C. Jernigan, *et al.*, "Pellet fuelling and control of burning plasmas in iter," *Nuclear fusion*, vol. 47, no. 5, pp. 443–448, 2007.

[61] A. Loarte, "Effects of divertor geometry on tokamak plasmas," *Plasma Physics and Controlled Fusion*, vol. 43, no. 6, R183, Jun. 2001. DOI: 10.1088/0741-3335/43/6/201.

[62] R. Hemsworth, D Boilson, P Blatchford, *et al.*, "Overview of the design of the iter heating neutral beam injectors," *New Journal of Physics*, vol. 19, no. 2, p. 025 005, 2017. DOI: 10.1088/1367-2630/19/2/025005.

[63] V. E. Golant and V. I. Fedorov, *RF plasma heating in toroidal fusion devices*. New York: Springer, 1989.

[64] G. Federici, L Boccaccini, F Cismondi, M Gasparotto, Y Poitevin, and I. Ricapito, "An overview of the eu breeding blanket design strategy as an integral part of the demo design effort," *Fusion Engineering and Design*, vol. 141, pp. 30–42, 2019.

[65] R Aymar, P Barabaschi, and Y Shimomura, "The iter design," *Plasma Physics and Controlled Fusion*, vol. 44, no. 5, p. 519, Apr. 2002. DOI: 10.1088/0741-3335/44/5/304.

[66] P. Rebut, R. Bickerton, and B. E. Keen, "The joint european torus: Installation, first results and prospects," *Nuclear fusion*, vol. 25, no. 9, p. 1011, 1985.

[67] t. A. T. H. Meyer and the EUROfusion MST1 Team, "Overview of physics studies on asdex upgrade," *Nuclear Fusion*, vol. 59, no. 11, p. 112 014, Jul. 2019. DOI: 10.1088/1741-4326/ab18b8.

[68] H. Ninomiya, T. Ando, T. Horie, *et al.*, "Jt-60 upgrade device for confinement and steady state studies," *Plasma Devices and Operations*, vol. 1, no. 1, pp. 43–65, 1990. DOI: 10.1080/10519999008225528.

[69] J. Luxon, "A design retrospective of the diii-d tokamak," *Nuclear Fusion*, vol. 42, no. 5, p. 614, May 2002. DOI: 10.1088/0029-5515/42/5/313.

[70] S. Coda, J Ahn, R. Albanese, *et al.*, "Overview of the tcv tokamak program: Scientific progress and facility upgrades," *Nuclear Fusion*, vol. 57, no. 10, p. 102 011, 2017.

[71] W. Morris, J. Harrison, A Kirk, *et al.*, "Mast upgrade divertor facility: A test bed for novel divertor solutions," *IEEE transactions on plasma science*, vol. 46, no. 5, pp. 1217–1226, 2018.

[72] J. Menard, S Gerhardt, M Bell, *et al.*, "Overview of the physics and engineering design of nstx upgrade," *Nuclear Fusion*, vol. 52, no. 8, p. 083 015, 2012.

[73] M. Shimada, D. Campbell, V. Mukhovatov, *et al.*, "Chapter 1: Overview and summary," *Nuclear Fusion*, vol. 47, no. 6, S1, Jun. 2007. DOI: 10.1088/0029-5515/47/6/S01.

[74] A. J. Creely, M. J. Greenwald, S. B. Ballinger, *et al.*, "Overview of the sparc tokamak," *Journal of Plasma Physics*, vol. 86, no. 5, p. 865 860 502, 2020. DOI: 10.1017/S0022377820001257.

[75] H. Wilson, I. Chapman, T. Denton, *et al.*, "Step—on the pathway to fusion commercialization," in *Commercialising Fusion Energy*, ser. 2053-2563, IOP Publishing, 2020, 8–1 to 8–18, ISBN: 978-0-7503-2719-0. DOI: 10.1088/978-0-7503-2719-0ch8. [Online]. Available: https://dx.doi.org/10.1088/978-0-7503-2719-0ch8.

[76] C. Bachmann, G. Aiello, R. Albanese, *et al.*, "Initial demo tokamak design configuration studies," *Fusion Engineering and Design*, vol. 98-99, pp. 1423–1426, 2015, Proceedings of the 28th Symposium On Fusion Technology (SOFT-28), ISSN: 0920-3796. DOI: https://doi.org/10.1016/j.fusengdes.2015.05.027.

[77] Y. Song, X. Zou, X. Gong, *et al.*, "Realization of thousand-second improved confinement plasma with super i-mode in tokamak east," *Science Advances*, vol. 9, no. 1, eabq5273, 2023.

[78] J Li, H. Guo, B. Wan, *et al.*, "A long-pulse high-confinement plasma regime in the experimental advanced superconducting tokamak," *Nature physics*, vol. 9, no. 12, pp. 817–821, 2013.

[79] F Wagner, "The history of research into improved confinement regimes," *The European Physical Journal H*, vol. 43, pp. 523–549, 2018.

[80] M. Abdou, M. Riva, A. Ying, *et al.*, "Physics and technology considerations for the deuterium–tritium fuel cycle and conditions for tritium fuel self sufficiency," *Nuclear fusion*, vol. 61, no. 1, p. 013 001, 2020.

[81] L. R. Baylor, C. Barbier, J. Carmichael, *et al.*, "Disruption mitigation system developments and design for iter," *Fusion Science and Technology*, vol. 68, no. 2, pp. 211–215, 2015.

[82] R. Pitts, X Bonnin, F Escourbiac, *et al.*, "Physics basis for the first iter tungsten divertor," *Nuclear Materials and Energy*, vol. 20, p. 100 696, 2019.

[83] P. C. Stangeby *et al.*, *The plasma boundary of magnetic fusion devices*. Philadelphia: IOP Publishing, 2000.

[84] R. A. Langley, J Bohdansky, W Eckstein, *et al.*, "Data compendium for plasma-surface interactions," *Nuclear Fusion*, vol. 24, no. S1, p. 001, 1984.

[85] A. Team *et al.*, "The h-mode of asdex," *Nuclear Fusion*, vol. 29, no. 11, p. 1959, 1989.

[86] T Hatae, M Sugihara, A. Hubbard, *et al.*, "Understanding of h mode pedestal characteristics using the multimachine pedestal database," *Nuclear fusion*, vol. 41, no. 3, p. 285, 2001.

[87] M Keilhacker, A Gibson, C Gormezano, and P. Rebut, "The scientific success of jet," *Nuclear fusion*, vol. 41, no. 12, p. 1925, 2001.

[88] A. Kuang, S Ballinger, D Brunner, *et al.*, "Divertor heat flux challenge and mitigation in sparc," *Journal of Plasma Physics*, vol. 86, no. 5, p. 865 860 505, 2020.

[89] C. S. Chang, S Ku, A. Loarte, *et al.*, "Gyrokinetic projection of the divertor heat-flux width from present tokamaks to iter," *Nuclear Fusion*, vol. 57, no. 11, p. 116 023, 2017.

[90] T. Eich, A. Leonard, R. Pitts, *et al.*, "Scaling of the tokamak near the scrape-off layer h-mode power width and implications for iter," *Nuclear fusion*, vol. 53, no. 9, p. 093 031, 2013.

[91] R. Pitts, J. Coad, D. Coster, *et al.*, "Material erosion and migration in tokamaks," *Plasma physics and controlled fusion*, vol. 47, no. 12B, B303, 2005.

[92] A. Kallenbach, R Neu, R Dux, *et al.*, "Tokamak operation with high-z plasma facing components," *Plasma physics and controlled fusion*, vol. 47, no. 12B, B207, 2005.

[93] S Suckewer and R. Hawryluk, "Plasma edge cooling during rf heating," *Physical Review Letters*, vol. 40, no. 25, p. 1649, 1978.

[94] J. Connor, "Edge-localized modes-physics and theory," *Plasma physics and controlled fusion*, vol. 40, no. 5, p. 531, 1998.

[95] A Loarte, G Saibene, R Sartori, *et al.*, "Transient heat loads in current fusion experiments, extrapolation to iter and consequences for its operation," *Physica Scripta*, vol. 2007, no. T128, p. 222, 2007.

[96] O Schmitz, M Becoulet, P Cahyna, *et al.*, "Three-dimensional modeling of plasma edge transport and divertor fluxes during application of resonant magnetic perturbations on iter," *Nuclear fusion*, vol. 56, no. 6, p. 066 008, 2016.

[97] P. T. Lang, K. Büchl, M. Kaufmann, *et al.*, "High-efficiency plasma refuelling by pellet injection from the magnetic high-field side into asdex upgrade," *Phys. Rev. Lett.*, vol. 79, pp. 1487–1490, 8 Aug. 1997. DOI: 10.1103/PhysRevLett.79.1487.

[98] A Kallenbach, M Bernert, R Dux, *et al.*, "Impurity seeding for tokamak power exhaust: From present devices via iter to demo," *Plasma Physics and Controlled Fusion*, vol. 55, no. 12, p. 124 041, 2013.

[99] P. Stangeby, "Basic physical processes and reduced models for plasma detachment," *Plasma Physics and Controlled Fusion*, vol. 60, no. 4, p. 044 022, 2018.

[100] O Février, C Theiler, S Coda, *et al.*, "Detachment in conventional and advanced double-null plasmas in tcv," *Nuclear Fusion*, vol. 61, no. 11, p. 116 064, 2021.

[101] B. D. Dudson, J Allen, T Body, *et al.*, "The role of particle, energy and momentum losses in 1d simulations of divertor detachment," *Plasma Physics and Controlled Fusion*, vol. 61, no. 6, p. 065 008, 2019.

[102] S. Krasheninnikov, A. Kukushkin, and A. Pshenov, "Divertor plasma detachment: Roles of plasma momentum, energy, and particle balances," *Plasma Physics and Controlled Fusion*, vol. 64, no. 12, p. 125 011, 2022.

[103] D. Ryutov, "Geometrical properties of a "snowflake" divertor," *Physics of Plasmas*, vol. 14, no. 6, p. 064 502, 2007.

[104] M. Kotschenreuther, P. Valanju, S. Mahajan, and J. Wiley, "On heat loading, novel divertors, and fusion reactors," *Physics of plasmas*, vol. 14, no. 7, p. 072 502, 2007. DOI: 10.1063/1.2739422.

[105] P. M. Valanju, M Kotschenreuther, S. Mahajan, and J. Canik, "Super-x divertors and high power density fusion devices," *Physics of Plasmas*, vol. 16, no. 5, p. 056 110, 2009.

[106] B LaBombard, E Marmar, J Irby, *et al.*, "Adx: A high field, high power density, advanced divertor and rf tokamak," *Nuclear Fusion*, vol. 55, no. 5, p. 053 020, 2015.

[107] M. Wigram, B. LaBombard, M. Umansky, *et al.*, "Performance assessment of long-legged tightly-baffled divertor geometries in the arc reactor concept," *Nuclear Fusion*, vol. 59, no. 10, p. 106 052, Sep. 2019. DOI: 10.1088/1741-4326/ab394f.

[108] G. Sun, H. Reimerdes, C. Theiler, *et al.*, "Performance assessment of a tightly baffled, long-legged divertor configuration in tcv with solps-iter," *Nuclear Fusion*, vol. 63, no. 9, p. 096 011, Aug. 2023. DOI: 10.1088/1741-4326/ace45f.

[109] H Reimerdes, R Ambrosino, P Innocente, *et al.*, "Assessment of alternative divertor configurations as an exhaust solution for demo," *Nuclear Fusion*, vol. 60, no. 6, p. 066 030, 2020.

[110] K. Verhaegh, B. Lipschultz, J. Harrison, *et al.*, "Spectroscopic investigations of detachment on the mast upgrade super-x divertor," *Nuclear Fusion*, vol. 63, no. 1, p. 016 014, 2022.

[111] C Theiler, B Lipschultz, J Harrison, *et al.*, "Results from recent detachment experiments in alternative divertor configurations on tcv," *Nuclear Fusion*, vol. 57, no. 7, p. 072 008, 2017.

[112] UK Atomic Energy Authority, *Mast upgrade research plan*, Nov. 2019. [Online]. Available: https://ccfe.ukaea.uk/wp-content/uploads/2019/12/MAST-U_RP_2019_v1.pdf.

[113] *Development of Steady State Compact Fusion Neutron Sources* (TECDOC Series 1998). Vienna: INTERNATIONAL ATOMIC ENERGY AGENCY, 2022, ISBN: 978-92-0-122722-5. [Online]. Available: https://www.iaea.org/publications/15069/development-of-steady-state-compact-fusion-neutron-sources.

[114] T. von Woedtke, S. Reuter, K. Masur, and K.-D. Weltmann, "Plasmas for medicine," *Physics Reports*, vol. 530, no. 4, pp. 291–320, 2013, Plasmas for Medicine, ISSN: 0370-1573. DOI: https://doi.org/10.1016/j.physrep.2013.05.005. [Online]. Available: https://www.sciencedirect.com/science/article/pii/S0370157313001634.

[115] C. Cardinaud, M.-C. Peignon, and P.-Y. Tessier, "Plasma etching: Principles, mechanisms, application to micro-and nano-technologies," *Applied Surface Science*, vol. 164, no. 1-4, pp. 72–83, 2000.

[116] M. Hapgood, *Space weather*. IOP Publishing, 2017.

[117] G. Federici, C. H. Skinner, J. N. Brooks, *et al.*, "Plasma-material interactions in current tokamaks and their implications for next step fusion reactors," *Nuclear Fusion*, vol. 41, no. 12, p. 1967, 2001.

[118] K.-U. Riemann, "The bohm criterion and sheath formation," *Journal of Physics D: Applied Physics*, vol. 24, no. 4, p. 493, 1991.

[119] D Bohm, "The characteristics of electrical discharges in magnetic fields," 1949.

[120] F. Militello, *Boundary Plasma Physics: An Accessible Guide to Transport, Detachment, and Divertor Design*. Springer Nature, 2022, vol. 123.

[121] D. G. Swanson, *Plasma kinetic theory*. Crc Press, 2008.

[122] D. Michels, A. Stegmeir, P. Ulbl, D. Jarema, and F. Jenko, "Gene-x: A full-f gyrokinetic turbulence code based on the flux-coordinate independent approach," *Computer Physics Communications*, vol. 264, p. 107 986, 2021.

[123] A. Peeters, Y. Camenen, F. J. Casson, *et al.*, "The nonlinear gyro-kinetic flux tube code gkw," *Computer physics communications*, vol. 180, no. 12, pp. 2650–2672, 2009.

[124] M. Kotschenreuther, G Rewoldt, and W. Tang, "Comparison of initial value and eigenvalue codes for kinetic toroidal plasma instabilities," *Computer Physics Communications*, vol. 88, no. 2-3, pp. 128–140, 1995.

[125] T. Arber, K. Bennett, C. Brady, *et al.*, "Contemporary particle-in-cell approach to laser-plasma modelling," *Plasma Physics and Controlled Fusion*, vol. 57, no. 11, p. 113 001, 2015.

[126] R Schneider, X Bonnin, K Borrass, *et al.*, "Plasma edge physics with b2-eirene," *Contributions to Plasma Physics*, vol. 46, no. 1-2, pp. 3–191, 2006. DOI: 10.1002/ctpp.200610001.

[127] S. Braginskii, "Transport phenomena in a completely ionized two-temperature plasma," *Sov. Phys. JETP*, vol. 6, no. 33, pp. 358–369, 1958.

[128] S. Braginskii, "Transport processes in a plasma," *Reviews of plasma physics*, vol. 1, p. 205, 1965.

[129] S. Chapman and T. G. Cowling, *The mathematical theory of non-uniform gases: an account of the kinetic theory of viscosity, thermal conduction and diffusion in gases*. Cambridge university press, 1990.

[130] D. Reiter *et al.*, "Eirene—a monte carlo linear transport solver," *URL http://www. eirene. de*, 2002.

[131] D Reiter *et al.*, "The eirene code user manual," *Julich KFA Report*, 2005.

[132] T. Rognlien, J. Milovich, M. Rensink, and G. Porter, "A fully implicit, time dependent 2-d fluid code for modeling tokamak edge plasmas," *Journal of Nuclear Materials*, vol. 196-198, pp. 347–351, 1992, Plasma-Surface Interactions in Controlled Fusion Devices, ISSN: 0022-3115. DOI: https://doi.org/10.1016/S0022-3115(06)80058-9.

[133] Y Feng, F Sardei, P Grigull, *et al.*, "Transport in island divertors: Physics, 3d modelling and comparison to first experiments on w7-as," *Plasma physics and controlled fusion*, vol. 44, no. 5, p. 611, 2002.

[134] H. Bufferand, C Baudoin, J Bucalossi, *et al.*, "Implementation of drift velocities and currents in soledge2d–eirene," *Nuclear Materials and Energy*, vol. 12, pp. 852–857, 2017.

[135] T. Petrie, J. M. Canik, C. Lasnier, *et al.*, "Effect of changes in separatrix magnetic geometry on divertor behaviour in diii-d," *Nuclear Fusion*, vol. 53, no. 11, p. 113 024, 2013.

[136] I. H. Hutchinson, "Thermal front analysis of detached divertors and marfes," *Nuclear Fusion*, vol. 34, no. 10, p. 1337, 1994.

[137] P. G. Carolan and V. A. Piotrowicz, "The behaviour of impurities out of coronal equilibrium," *Plasma Physics*, vol. 25, no. 10, p. 1065, Oct. 1983. DOI: 10.1088/0032-1028/25/10/001. [Online]. Available: https://dx.doi.org/10.1088/0032-1028/25/10/001.

[138] U. Stroth, M. Bernert, D. Brida, *et al.*, "Occurrence and control of x-point radiators and marfes in asdex upgrade: Experimental validation of an analytic model," *Bulletin of the American Physical Society*, 2022.

[139] G. Matthews, "Plasma detachment from divertor targets and limiters," *Journal of nuclear materials*, vol. 220, pp. 104–116, 1995.

[140] T Lunt, M Bernert, D Brida, *et al.*, "Compact radiative divertor experiments at asdex upgrade and their consequences for a reactor," *Physical Review Letters*, vol. 130, no. 14, p. 145 102, 2023.

[141] M Bernert, F Janky, B Sieglin, *et al.*, "X-point radiation, its control and an elm suppressed radiating regime at the asdex upgrade tokamak," *Nuclear Fusion*, vol. 61, no. 2, p. 024 001, 2020.

[142] M. Capitelli, G. Colonna, and A. D'Angola, *Fundamental aspects of plasma chemical physics*. Springer, 2012, vol. 66.

[143] D Moulton, J Harrison, B Lipschultz, and D Coster, "Using solps to confirm the importance of total flux expansion in super-x divertors," *Plasma Physics and Controlled Fusion*, vol. 59, no. 6, p. 065 011, 2017.

[144] N. Vianello, C. Tsui, C. Theiler, *et al.*, "Modification of sol profiles and fluctuations with line-average density and divertor flux expansion in tcv," *Nuclear Fusion*, vol. 57, no. 11, p. 116 014, Aug. 2017. DOI: 10.1088/1741-4326/aa7db3.

[145] S. Krasheninnikov, P. Catto, P Helander, D. Sigmar, and T. Soboleva, "Thermal bifurcation of scrape-off layer plasma and divertor detachment," *Physics of Plasmas*, vol. 2, no. 7, pp. 2717–2728, 1995.

[146] H. Du, G. Zheng, H. Guo, *et al.*, "Solps analysis of the necessary conditions for detachment cliff," *Nuclear Fusion*, vol. 60, no. 4, p. 046 028, 2020.

[147] S. Krasheninnikov, A. Kukushkin, A. Pshenov, A. Smolyakov, and Y. Zhang, "Stability of divertor detachment," *Nuclear Materials and Energy*, vol. 12, pp. 1061–1066, 2017.

[148] P. B. Snyder, H. R. Wilson, T. H. Osborne, and A. W. Leonard, "Characterization of peeling–ballooning stability limits on the pedestal," *Plasma Physics and Controlled Fusion*, vol. 46, no. 5A, A131, Apr. 2004. [Online]. Available: https://dx.doi.org/10.1088/0741-3335/46/5A/014.

[149] T. Wijkamp, J. Allcock, X Feng, *et al.*, "Characterisation of detachment in the mast-u super-x divertor using multi-wavelength imaging of 2d atomic and molecular emission processes," *Nuclear Fusion*, vol. 63, no. 5, p. 056 003, 2023.

[150] X Feng, A Calcines, R. Sharples, *et al.*, "Development of an 11-channel multi wavelength imaging diagnostic for divertor plasmas in mast upgrade," *Review of Scientific Instruments*, vol. 92, no. 6, p. 063 510, 2021.

[151] A Perek, W. Vijvers, Y Andrebe, *et al.*, "Mantis: A real-time quantitative multispectral imaging system for fusion plasmas," *Review of Scientific Instruments*, vol. 90, no. 12, 2019.

[152] J. Allcock, S. Silburn, R. Sharples, J. Harrison, N. Conway, and J. Vernimmen, "2d measurements of plasma electron density using coherence imaging with a pixelated phase mask," *Review of Scientific Instruments*, vol. 92, no. 7, 2021.

[153] J. G. Clark, M. D. Bowden, and R. Scannell, "Low temperature Thomson scattering on MAST-U," *Review of Scientific Instruments*, vol. 92, no. 4, p. 043 545, Apr. 2021, ISSN: 0034-6748. DOI: 10.1063/5.0043813.

[154] R. Scannell, M. J. Walsh, M. R. Dunstan, *et al.*, "A 130 point Nd:YAG Thomson scattering diagnostic on MASTa)," *Review of Scientific Instruments*, vol. 81, no. 10, p. 10D520, Oct. 2010, ISSN: 0034-6748. DOI: 10.1063/1.3460628.

[155] L. Lao, H. S. John, R. Stambaugh, A. Kellman, and W. Pfeiffer, "Reconstruction of current profile parameters and plasma shapes in tokamaks," *Nuclear Fusion*, vol. 25, no. 11, p. 1611, Nov. 1985. DOI: 10.1088/0029-5515/25/11/007.

[156] T O'Gorman, G Naylor, R Scannell, *et al.*, "Design of a real-time two-color interferometer for mast upgrade," *Review of Scientific Instruments*, vol. 85, no. 11, 2014.

[157] K. Verhaegh, B. Lipschultz, J. R. Harrison, *et al.*, "The role of plasma-atom and molecule interactions on power and particle balance during detachment on the mast upgrade super-x divertor," *Nuclear Fusion*, 2023. [Online]. Available: http://iopscience.iop.org/article/10.1088/1741-4326/acf946.